SAND2019-11688R

Update on the Thermal Hydraulic Investigations of a Horizontal Dry Cask Simulator

Spent Fuel and Waste Disposition

Prepared for
US Department of Energy
Spent Fuel and Waste Science and Technology

E.R. Lindgren
S.G. Durbin
R.J.M. Pulido
A. Salazar

Sandia National Laboratories
September 27, 2019
Milestone No. M2SF-19SN010203034
SAND2019-11688 R

Prepared by
Sandia National Laboratories
Albuquerque, New Mexico 87185 and Livermore, California 94550

Sandia National Laboratories is a multimission laboratory managed and operated by National Technology and Engineering Solutions of Sandia, LLC, a wholly owned subsidiary of Honeywell International, Inc., for the U.S. Department of Energy's National Nuclear Security Administration under contract DE-NA0003525.

Sandia National Laboratories

EXECUTIVE SUMMARY

The thermal performance of commercial spent nuclear fuel dry storage casks is evaluated through detailed numerical analysis. These modeling efforts are completed by the vendor to demonstrate performance and regulatory compliance. The calculations are then independently verified by the Nuclear Regulatory Commission (NRC). Canistered dry storage cask systems rely on ventilation between the inner canister and the overpack to convect heat away from the canister to the surrounding environment for both horizontal and vertical configurations. Recent advances in dry storage cask designs have significantly increased the maximum thermal load allowed in a canister in part by increasing the efficiency of internal conduction pathways and by increasing the internal convection through greater canister helium pressure. Carefully measured data sets generated from testing of full-sized casks or smaller cask analogs are widely recognized as vital for validating these models. While several testing programs have been previously conducted, these earlier validation studies did not integrate all the physics or components important in a modern, horizontal dry cask system.

The purpose of the present investigation is to produce data sets that can be used to benchmark the codes and best practices presently used to determine cladding temperatures and induced cooling air flows in modern horizontal dry storage systems. The horizontal dry cask simulator (HDCS) has been designed to generate this benchmark data and add to the existing knowledge base. The objective of the HDCS investigation is to capture the dominant physics of a commercial dry storage system in a well-characterized test apparatus for any given set of operational parameters. The close coupling between the thermal response of the canister system and the resulting induced cooling air flow rate is of particular importance.

The pressure vessel representing the canister has been designed, fabricated, and pressure tested for a maximum allowable working pressure (MAWP) rating of 2,400 kPa at 400 °C. An existing electrically heated but otherwise prototypic boiling water reactor (BWR), Incoloy-clad test assembly has been deployed inside of a representative storage basket and canister. An insulated sheet metal enclosure is used to mimic the thermal properties of the concrete vault enclosure used in a modern horizontal storage system. Transverse and axial temperature profiles along with induced cooling air flow are measured for a wide range of decay powers and representative (and higher) canister pressures using various backfills of helium or air.

The single assembly geometry with well-controlled boundary conditions simplifies computational requirements while preserving relevant physics. The test apparatus integrates all the underlying thermal-hydraulics important to defining the performance of a modern horizontal storage system. These include combined-mode heat transfer from the electrically-heated assembly to the canister walls and the primarily natural-convective heat transfer from the canister to the cooling air flow passing through the horizontal vault enclosure.

In a previous investigation, data sets from a vertically oriented dry cask simulator (DCS) were used in a model validation activity. However, this model validation activity was not fully blind in that all the modeling participants had access to complete data sets. Data from the present investigation using the HDCS will be used to host a blind model validation effort. Although a complete set of data has been collected with the HDCS spanning fill pressures of both helium and air from 100 kPa to 800 kPa and assembly powers from 0.5 kW to 5.0 kW, only the data from two test cases are presented in this report. These cases include an assembly power of 2.50 kW and a backfill gas of helium for one case and air for the other, both at a pressure of 100 kPa. This limited data set is provided for model comparison and refinement. The other test cases are reserved for a future blind model validation study.

The steady-state peak temperatures for the components located inside the pressure vessel (canister) were significantly lower for the helium fill case than the air fill case. The PCT for the helium case was 559 K and located at an axial location of 1.22 m. The PCT for the air fill case was 647 K and located at an axial

location of 0.61 m. The vertical and horizontal temperature profiles both indicate that the temperature gradients between the components inside the pressure vessel are lower in the helium case than in the air case.

ACKNOWLEDGEMENTS

The authors would like to acknowledge the hard work and commitment of all contributors to the project. In particular, we would like to acknowledge the strong support and leadership of Ned Larson at the Department of Energy. Sylvia Saltzstein (8845) and Geoff Freeze (8843) are to be commended for their programmatic and technical guidance.

The authors would also like to thank Greg Koenig, William Chavez, Adrian Perales, Kyle Tsosie, and Dominic Fascitelli of 8843 for their tireless efforts and dedication to service, which made the success of this project possible.

This page is intentionally left blank.

CONTENTS

LIST OF FIGURES

This page is intentionally left blank.

LIST OF TABLES

ACRONYMS / ABBREVIATIONS

BR	blockage ratio
BWR	boiling water reactor
CFD	computational fluid dynamics
CYBL	Cylindrical Boiling
DCS	Dry Cask Simulator
DOE	Department of Energy
DSC	dry storage canister
HDCS	Horizontal Dry Cask Simulator
HSM	Horizontal Storage Module
ISFSI	independent spent fuel storage installation
MAWP	maximum allowable working pressure
NE	Nuclear Energy
NRC	Nuclear Regulatory Commission
PCT	peak cladding temperature
PWR	pressurized water reactor
SFWD	Spent Fuel and Waste Disposition
SNF	spent nuclear fuel
SNL	Sandia National Laboratories
TC	thermocouple

This page is intentionally left blank.

UPDATE ON THE THERMAL HYDRAULIC INVESTIGATIONS OF A HORIZONTAL DRY CASK SIMULATOR

This report fulfills milestone M2SF-19SN010203034 (Update on the Thermal Hydraulic Investigations of a Horizontal Dry Cask Simulator) in the Spent Fuel and Waste Science and Technology work package (SF-19SN01020303). This work was sponsored under the Department of Energy's (DOE) Office of Nuclear Energy (NE) Spent Fuel and Waste Disposition (SFWD) campaign.

1 INTRODUCTION

The performance of commercial spent nuclear fuel dry storage casks is typically evaluated through detailed analytical modeling of the system's thermal performance. These modeling efforts are performed by the vendor to demonstrate both performance and regulatory compliance and are independently verified by the Nuclear Regulatory Commission (NRC). The majority of commercial dry storage casks currently in use are aboveground in both horizontal and vertical orientations. Figure 1.1 shows a diagram for a typical horizontal system. Cooling of the assemblies located inside the sealed canister is enhanced by the induced flow of air drawn in the bottom of the enclosure and exiting out the top of the enclosure.

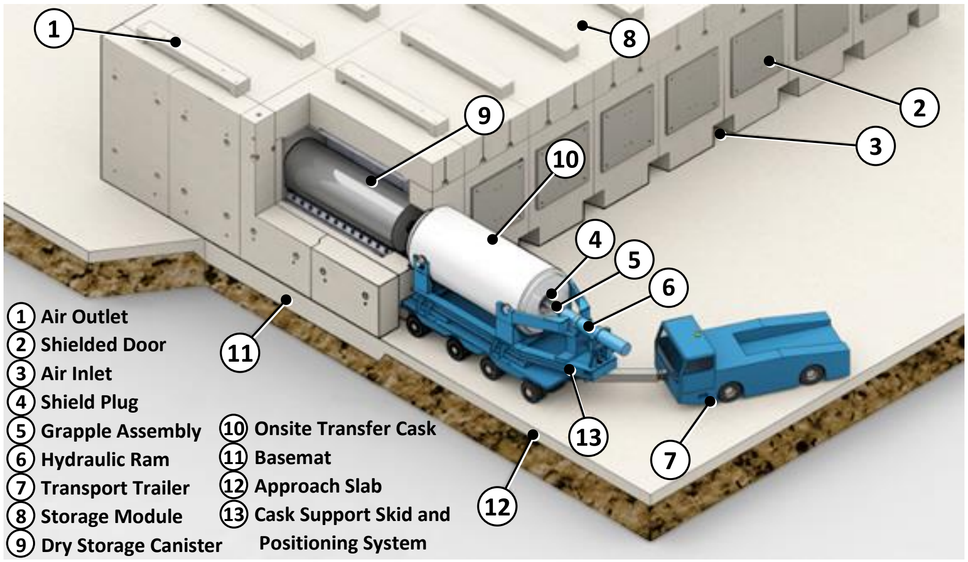

Source: http://us.areva.com/EN/home-3138/areva-nuclear-materials-tn-americas--nuhoms-used-fuel-storage-system.html#tab=tab6

Figure 1.1 Horizontal dry storage cask system.

Carefully measured data sets generated from testing of full-sized casks or smaller cask analogs are widely recognized as vital for validating design and performance models. Numerous studies have been previously conducted [Bates, 1986; Dziadosz and Moore, 1986; Irino *et al.*, 1987; McKinnon *et al.*,1986]. Recent advances in dry storage cask designs have significantly increased the maximum thermal load allowed in a canister in part by improving the efficiency of internal conduction pathways and by enhancing internal convection through greater canister helium pressure. Horizontal, canistered cask systems rely on ventilation between the canister and the vault walls to convect heat away from the canister to the surrounding environment. While several testing programs have been previously conducted, these earlier validation attempts did not integrate all of the physics or components important in modern horizontal dry cask systems. Thus, the enhanced performance of modern horizontal dry storage systems cannot be fully validated using previous studies.

1.1 Objective

The purpose of the investigation described in this update report is to document initial data sets that can be used to benchmark the codes and best practices presently used to calculate cladding temperatures and induced cooling air flows in modern horizontal dry storage systems. The horizontal dry cask simulator (HDCS) has been designed to generate this benchmark data and add to the existing knowledge base.

1.2 Previous Studies

1.2.1 Small Scale, Single Assembly

Two single assembly investigations were documented in the mid-1980s [Bates, 1986; Irino *et al.*, 1987]. Both included electrically heated 15×15 pressurized water reactor (PWR) assemblies with thermocouples (TCs) installed to directly measure the surface temperature of the cladding. In Bates (1986) the electrically heated assembly was instrumented with fifty-seven TCs distributed over seven axial levels. In Irino *et al.* (1987) the electrically heated assembly was instrumented with ninety-two TCs distributed over four axial levels. In Bates (1986) a single irradiated 15×15 PWR assembly was also studied using 105 TCs distributed equally into each of the fifteen guide tubes at seven axial levels. All testing included horizontal orientation using helium or air at one atmosphere but imposed a constant temperature boundary condition on the outer cask wall in order to obtain prototypic storage temperatures in the fuel assembly bundle. None of these tests incorporated the naturally convective cooling by induced air flow inside of vault-like enclosures.

In a recent investigation [Durbin and Lindgren, 2018], an existing electrically heated but otherwise prototypic BWR Incoloy-clad test assembly was deployed inside of a representative storage basket and cylindrical pressure vessel that represents a vertical canister system. The symmetric single assembly geometry with well-controlled boundary conditions simplified interpretation of results. Two different arrangements of ducting were used to mimic conditions for aboveground and belowground storage configurations for vertical, dry cask systems with canisters. Transverse and axial temperature profiles were measured throughout the test assembly. The induced air mass flow rate was measured for both the aboveground and belowground configurations. In addition, the impact of cross-wind conditions on the belowground configuration was quantified.

Over 40 unique data sets were collected and analyzed for these efforts. Fourteen data sets for the aboveground configuration were recorded for powers and internal pressures ranging from 0.5 to 5.0 kW and 0.3 to 800 kPa absolute, respectively. Similarly, fourteen data sets were logged for the belowground configuration starting at ambient conditions and concluding with thermal-hydraulic steady state. Over thirteen tests were conducted using a custom-built wind machine. The results documented in the BWR dry cask simulator (DCS) test report [Durbin and Lindgren, 2018] highlight a small, but representative, subset of the available data from this test series.

Data sets from the vertically oriented dry cask simulator were used in a model validation activity [Pulido *et al.*, 2019]. In this study, a model validation exercise was carried out using the data obtained from dry cask simulator testing in the vertical, aboveground configuration. Five modeling institutions – Nuclear Regulatory Commission (NRC), Pacific Northwest National Laboratory (PNNL), Centro de Investigaciones Energéticas, MedioAmbientales y Tecnológicas (CIEMAT), and Empresa Nacional del Uranio, S.A., S.M.E. (ENUSA) in collaboration with Universidad Politécnica de Madrid (UPM) – were granted access to the input parameters from SAND2017-13058R, “Materials and Dimensional Reference Handbook for the Boiling Water Reactor Dry Cask Simulator”, and results from the vertical aboveground BWR dry cask simulator tests reported in NUREG/CR-7250, “Thermal-Hydraulic Experiments Using A Dry Cask Simulator”. With this information, each institution was tasked to calculate minimum, average, and maximum fuel axial temperature profiles for the fuel region as well as the axial temperature profiles of the DCS structures. Transverse temperature profiles and air mass flow rates within the dry cask simulator were also calculated. These calculations were done using modeling codes (ANSYS FLUENT, STAR-CCM+, or COBRA-SFS), each with their own unique combination of modeling assumptions and boundary conditions. For this validation study, four test cases of the vertical, aboveground dry cask simulator were considered, defined by two independent variables – either 0.5 kW or 5 kW fuel assembly decay heat, and either 100 kPa or 800 kPa internal helium pressure. However, this model validation activity was not fully blind in that all the modeling participants had access to complete data sets. Data from the present investigation using the HDCS will be used to host a blind model validation effort.

1.2.2 Full Scale, Multi Assembly

Several full-scale, multi-assembly cask studies were also documented in the mid-1980s to early 1990s, one for a BWR cask with unconsolidated fuel assemblies [McKinnon *et al*., 1986] and the others for PWR casks with both consolidated and unconsolidated fuel [Dziadosz *et al*., 1986; McKinnon *et al*., 1987; Creer *et al*., 1987; McKinnon *et al*.,1989; Strope *et al*., 1990]. Only in the most recent study was a ventilated horizontal cask design tested. In all studies the cask or canister was studied with internal atmospheres ranging from vacuum up to 150 kPa using air, nitrogen, or helium. Recently, detailed thermal modeling results of a NUHOMS Horizontal Storage Module (HSM) with a 24P canister deployed at Calvert Cliffs were compared to limited canister surface temperature measurements [Suffield *et al*., 2012].

1.2.2.1 Unventilated

In the first study [McKinnon *et al*., 1986], twenty-eight or fifty-two BWR assemblies with a total heat load of 9 or 15 kW, respectively, were contained in a REA 2023 prototype steel-lead-steel cask with a water-glycol neutron shield. Thirty-eight TCs were installed on the cask interior. Twenty-four of those were installed in direct contact with the center rod in seven assemblies at up to seven different elevations. Twelve were installed on the basket at three different elevations. Two TCs were installed in direct contact with a fuel rod located on the center outer face of an assembly. The cask was tested in an open environment in both a vertical and horizontal orientation with internal atmospheres of vacuum or nitrogen at 145 kPa (21.0 psia) average or helium at 152 kPa (22 psia) average.

In the earliest full-scale PWR cask study [Dziadosz *et al*., 1986], twenty-one PWR assemblies with a total heat load of 28 kW were contained in a Castor-V/21 cast iron/graphite cask with polyethylene rod neutron shielding. The interior of the cask was instrumented with sixty TCs deployed on ten lances located in eight guide tubes and two basket void spaces. Two of the assembly lances were installed into the center assembly. Note that with the use of TC lances inside of the assembly guide tubes, no direct fuel cladding temperatures were measured. The cask was tested in an open environment in both a vertical and horizontal orientation with internal atmospheres of vacuum or nitrogen at 57 kPa or helium at 52 kPa.

A relatively low total heat load of 12.6 kW was tested in a Westinghouse MC-10 cask with twenty-four PWR assemblies [McKinnon *et al*., 1987]. The MC-10 has a forged steel body and distinctive vertical carbon steel heat transfer fins around the outer circumference. The outer surface of the cask was instrumented with thirty-four TCs. The interior of the cask was instrumented with fifty-four TCs deployed on nine TC lances in seven fuel assembly guide tubes and two basket void spaces. The cask was tested in an open environment in both a vertical and horizontal orientation and the interior atmosphere was either a vacuum or 150 kPa helium or air.

A pair of studies using the same TN-24 cask was tested with twenty-four PWR assemblies with 20.5 kW total output [Creer *et al*., 1987] or twenty-four consolidated fuel canisters with 23 kW total output [McKinnon *et al*., 1989]. The TN-24P has a forged steel body surrounded by a resin layer for neutron shielding. The resin layer is covered by a smooth steel outer shell. The TN-24P is a prototype version of the standard TN-24 cask with differences in the cask body thickness, basket material and neutron shield structure. The TN-24P also incorporates fourteen TCs into the basket structure. In either study the fuel was instrumented with nine TC lances with six TCs per lance, seven in fuel guide tubes and two in simulated guide tubes in basket void spaces. The outside surface was instrumented with thirty-five TCs in the unconsolidated fuel study [Creer *et al*., 1987] and twenty-seven TCs in the consolidated fuel study [McKinnon *et al*.,1989]. In both studies the cask was tested in an open environment in both vertical and horizontal orientations with the interior atmosphere as either a vacuum or 150 kPa helium or air. A seventh test was conducted in the consolidated fuel study [McKinnon *et al*., 1989] for a horizontal orientation under vacuum with insulated ends to simulate impact limiters.

None of the previous studies discussed so far included or accounted for ventilation inside of a horizontal cask or vault. Both single assembly investigations that included a horizontal orientation imposed constant temperature boundary conditions [Bates, 1986; Irino *et al*., 1987], and the four full scale cask studies [Dziadosz *et al*., 1986; McKinnon *et al*., 1987; Creer *et al*., 1987; McKinnon *et al*.,1989] only considered cask designs externally cooled in an open environment.

1.2.2.2 Ventilated

Performance testing of a commercial NUHOMS-07P horizontal PWR spent fuel storage system was conducted in the mid to late 1980s [Strope *et al*., 1990]. The NUHOMS-07P horizontal PWR spent fuel storage system is an early, much smaller version of modern horizontal systems in common use today. The system consists of a stainless steel dry storage canister (DSC) with a welded closure that is housed in a concrete vault called a horizontal storage module (HSM). Ventilation inlets and outlets in the HSM induce air flow over and around the DSC to passively remove heat. Eight NUHOMS-07P systems were constructed and loaded under a site-specific license for use at Duke Energy's H.B. Robinson independent spent fuel storage installation (ISFSI). Each unit stores seven 15×15 PWR assemblies. When the first three systems were fabricated, two of the vaults were instrumented with fifty-four type J TCs, and two canisters were instrumented with twenty-five TCs each. Prior to loading with fuel, two test series were conducted using electric heaters to simulate the fuel. A single Chromalox Calrod was deployed in the center of each of the seven fuel basket tubes. Other than inputting the desired heat, the heater rod did not hydraulically or thermally simulate the prototypic nature of a spent fuel assembly.

The first test series was conducted with an instrumented DSC inside of an IF-300 spent fuel transportation cask. In this test series, temperatures were measured while the DSC, with heater rods, was flooded with water, vacuum dried, and backfilled with helium. No mock fuel assemblies were occupying any of the storage cells (referred to as fuel sleeves in the report), but five TC spears were located in the center of most storage cells. The seven heater rods were powered at 1 kW each for a total of 7 kW in the DSC. The maximum temperatures reported (during vacuum drying) was 255 °C for the top of the center fuel sleeve wall and 288 °C for the center of the empty center fuel sleeve.

The next test series was conducted with the electrically heated DSC located in the instrumented HSM. Under normal operation with a total DSC power of 7 kW, the maximum temperature reported was 201 °C for a fuel sleeve wall and 241 °C for the empty fuel sleeve centerline. Blocking the HSM air inlets and outlets increased these peak temperatures to 225 °C and 264 °C respectively. Increasing the total power from 7 kW to 13 kW increased the fuel sleeve temperature to 291 °C and the empty sleeve centerline to 340 °C. Decreasing the power to 2.2 kW decreased these temperatures to 116 °C and 142 °C respectively.

For the final test series, the heater rods were removed and the dry canisters were loaded with nominally 5 kW of actual spent nuclear fuel. Unfortunately, when the spent fuel assemblies were loaded many of the TCs in the DSC were damaged. Only one TC spear that measured the upper fuel assembly centerline temperature survived. With all three HSMs loaded with spent fuel, the maximum fuel sleeve wall temperature was 156 °C and the maximum fuel temperature in the upper horizontal assembly was 180 °C.

Throughout the second and third test series conducted using an HSM, attempts were made to measure the flow of air into the HSM air inlet. Unfortunately, the data was found to be erratic and judged to be unreliable. The data from the air velocity measurements were not used in the evaluation. The usefulness of the performance data for model validation purposes is seriously compromised by the limited temperature data and the absence of the air flow data.

1.2.3 Uniqueness of Present Test Series

The present investigation uses a simplified, well-characterized single-assembly test apparatus that integrates the dominant physics in prototypic systems. This approach differs from previous studies in several major respects. Principal among these is that the ventilated boundary conditions for a horizontal configuration are explicitly considered. Accurate, induced air flow rates were measured using the successful approach used in previous studies [Durbin and Lindgren, 2018]. Rather than striving to achieve prototypic peak clad temperatures by artificially imposing a temperature boundary condition on the canister wall, the present study incorporates relevant physics by including realistic boundary conditions.

Additionally, the apparatus contained a hydraulically and thermally prototypic mock assembly that can accommodate elevated pressures. The pressure vessel allowed testing at prototypic pressures of 100 to 150 kPa. Testing at higher pressures was conducted in order to experimentally quantify the contribution of convection and evaluate the assumption that convective heat transfer inside the canister is negligible.

As was the case in the previous vertical DCS studies [Durbin and Lindgren, 2018] a scaling distortion in simulated assembly power is necessary to more closely match the thermal-hydraulic response of a full-sized spent fuel storage cask. This need for additional decay heat is reasonable given the higher external surface-area-to-volume ratio of a single assembly arrangement as in the HDCS compared to a modern canister with up to eighty-nine assemblies.

This page is intentionally left blank.

2 APPARATUS AND PROCEDURES

2.1 General Construction

The core of the vertical Dry Cask Simulator (DCS) used in previous studies [Durbin and Lindgren, 2018] was modified for configuration to a horizontal orientation. The general design details with the required support modifications are shown in Figure 2.1, and additional dimensional details are shown in Appendix B. As before, an existing electrically heated but otherwise prototypic 9×9 BWR Incoloy-clad test assembly was deployed inside of a representative storage basket and cylindrical pressure vessel that represents the canister. Transverse and axial temperature profiles (using TCs detailed in Section 2.4.1) as well as induced cooling air flow rates (using hotwire anemometers detailed in Section 2.4.4) have been measured for a wide range of decay power and canister pressures as detailed in Section 2.6.

In prototypic horizontal systems, the assemblies are free to make direct contact with the bottom face of the basket. Due to existing mechanical fixturing and instrumentation at the fuel assembly base, the HDCS assembly is not free to make direct contact with the basket and must maintain concentricity to avoid damage during reorientation to a horizontal configuration. Therefore, a full-length aluminum (alloy 6061) bridge plate 127 mm (5 in.) wide and 9.6 mm (0.378 in.) thick was installed between the assembly channel box and the inside face of the basket to establish a conductive pathway and maintain concentric spacing of the assembly. Set screws were also installed through the basket on the other three sides to center and stabilize the channel box. Geometric details of the contact between the aluminum plate and the channel box are shown in Figure 2.2. There is limited contact between the corners of the channel box and the aluminum bridge plate. Of the 127 mm width of the bridge plate, only a total of 13.4 mm (0.528 in.) makes contact with the channel box shoulders and the center 97 mm (3.82 in.) is separated by a 0.9 mm (0.0354 in.) gas gap.

Full-length stabilizing tubes along the corners of the basket provided limited conductive paths between the basket and the pressure vessel while keeping the basket centered in the pressure vessel and limiting convective cells as shown in Figure 2.3. The stainless steel 304 tubes had an outer diameter of 12.7 mm (0.500 in.) and wall thickness of 1.59 mm (0.0625 in.). The tubes were stitch welded to the basket at 0.61 m (24 in.) intervals from the basket bottom to the top. These stitch welds had a nominal length of 25.4 mm (1.00 in.). Once the pressure vessel was installed, these stabilizer tubes formed line contacts on both the basket and the pressure vessel.

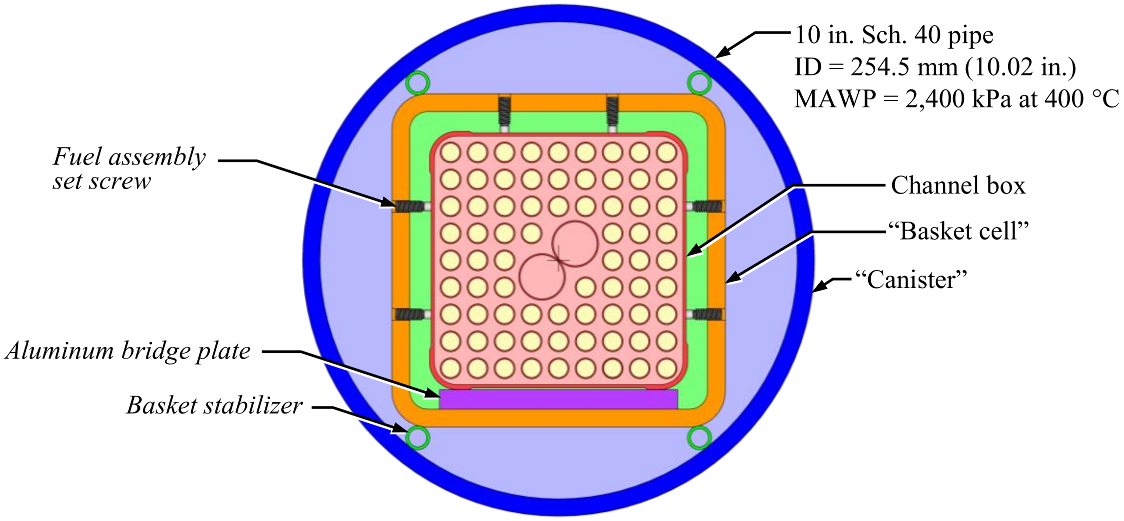

Figure 2.1 General design details of the dry cask simulator with initial *modifications*.

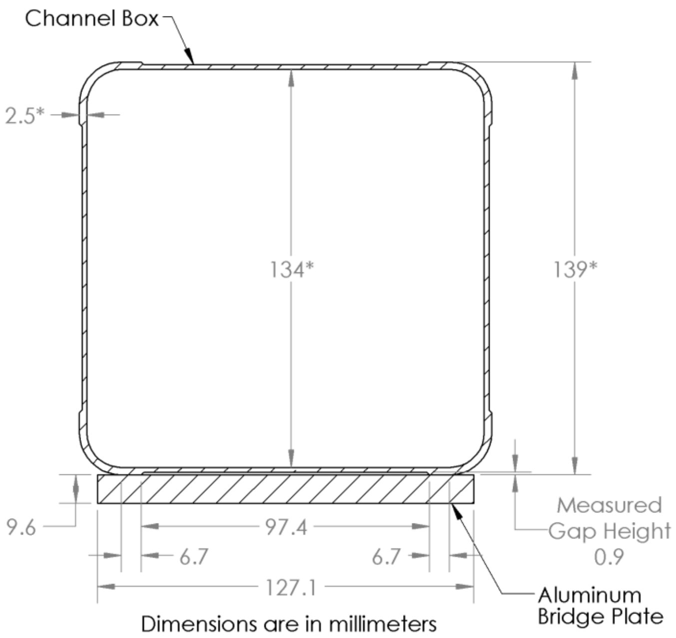

Figure 2.2 Channel box and aluminum bridge plate dimensions, including the contact dimensions and the dimensions of the gap between the channel box and bridge plate [*Yamamoto *et al.*, 2002].

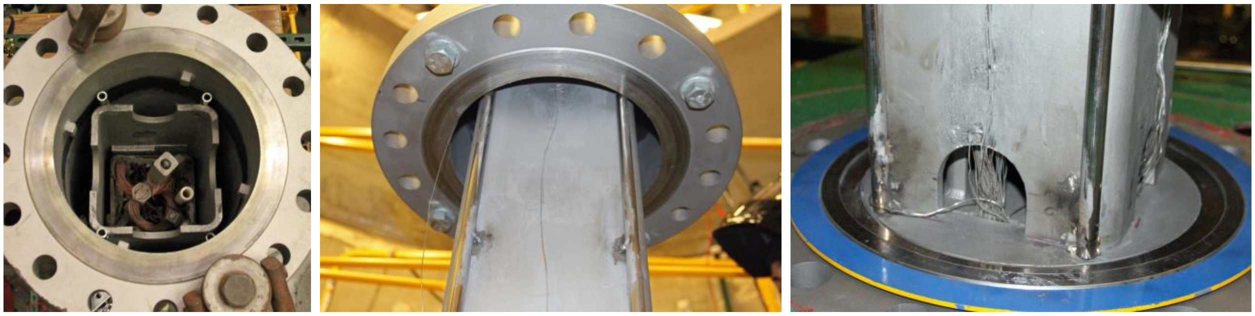
Top View **Middle View** **Bottom View**

Figure 2.3 Photographs of the test assembly showing the basket stabilizer rods.

The horizontal test apparatus is enclosed in an insulated stainless-steel sheet metal enclosure that simulates the concrete vault as shown as a partially exploded view in Figure 2.4 and described in detail in Section 2.2. The vault is comprised of 11-gauge stainless steel sheet metal components. Three side ribs on each side support two side panels and two top panels. Panels on each end enclose around the pressure vessel pipe. Inlet and outlet vents to the vault enclosure are located on the top and bottom of each of the four side panels. The vault inlets are supplied by rectangular ducts in which the induced flow is measured using hot wire anemometers. Because the induced flow for the HDCS is expected to be similar to that measured in the aboveground DCS study, the inlet ducts are designed to be the same size. The flow area of the vault inlet and outlet vents also match the flow area of the inlet ducts. The exterior of the sheet metal is covered with a thin layer of insulation (not shown) to mimic the thermal resistance of the walls in a commercial concrete vault (see Section 2.2 for details).

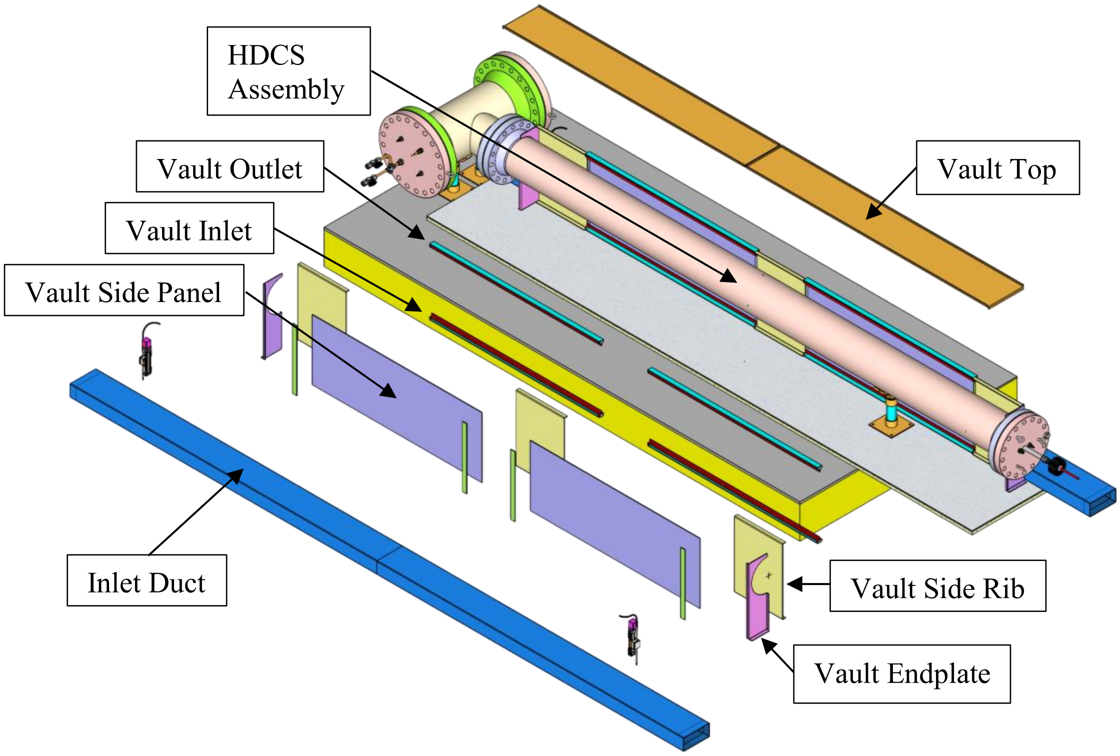

Figure 2.4 HDCS and partially exploded sheet metal vault components.

The new test configuration was assembled and operated inside of the Cylindrical Boiling (CYBL) test facility, which is the same facility used for earlier fuel assembly studies [Lindgren and Durbin, 2013; Durbin and Lindgren, 2018]. The apparatus was lifted out of the CYBL vessel and rotated to a horizontal orientation on a platform on the third (top) floor of the CYBL building. Figure 2.5 shows a scaled diagram of CYBL facility with the DCS inside. The stainless-steel vault enclosure has been assembled around the pressure vessel after it is laid in the horizontal position.

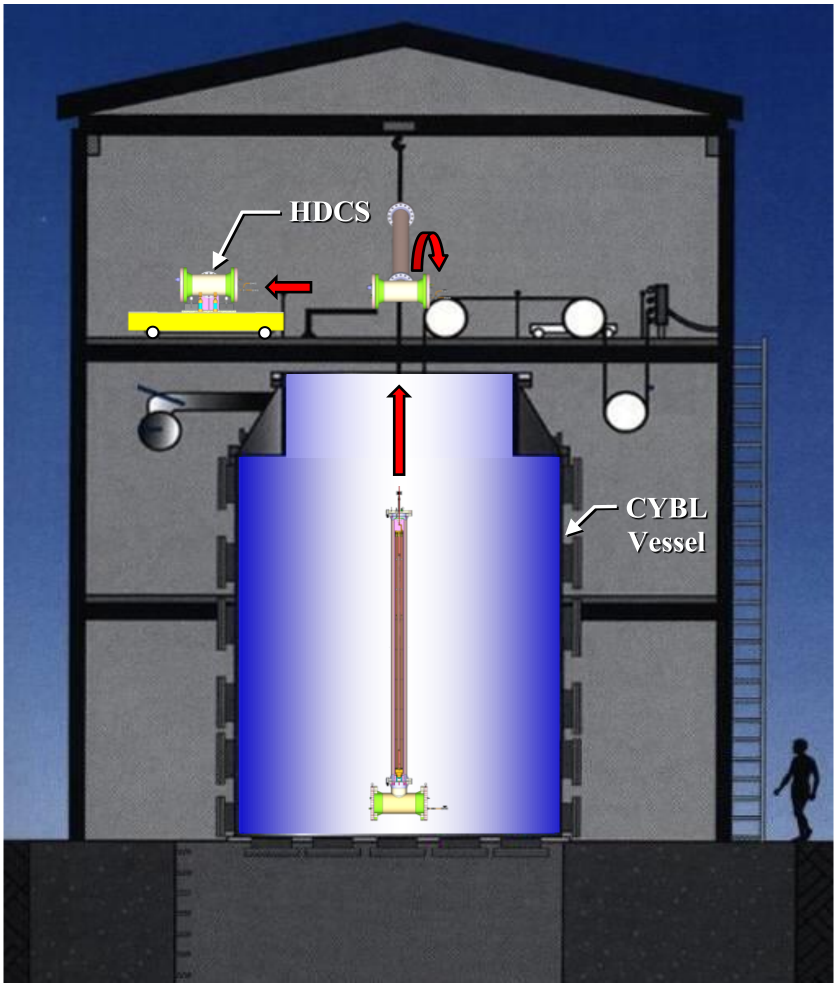

Figure 2.5 CYBL facility housing dry cask simulator testing.

2.2 Design of Vault

The HDCS enclosure was scaled to a NUHOMS HSM Model 80 and Model 102 vault containing a NUHOMS 61BT canister by the blockage ratio (BR) defined as the ratio of the diameter of the canister to the inside width of the vault as shown in Figure 2.6. For design purposes, the air mass flow rate for the HDCS was assumed from values measured during similar, vertical test conditions [Durbin and Lindgren, 2018]. This assumption was justified by observing the comparability in the air mass flow calculated by the modeling two prototypic systems NUHOMS HSM (0.25 kg/s) and the Holtec HI-STORM 100 (0.32 kg/s) with computational fluid dynamics (CFD) [Solis and Zigh, 2015]. Thus, the inlet and outlets to the vault enclosure were designed to have a flow area that matched the aboveground, vertical DCS apparatus. As with the aboveground vertical case, the HDCS has four inlet ducts each with inside dimensions of 0.102 m (4.02 in.) by 0.229 m (9.02 in.) and air velocity anemometers were used to measure the inlet flow rate. Computer-controlled stages were used to automatically traverse across the inlet opening to measure the flow field.

A simple analysis using one-dimensional thermal resistances for combined heat transfer was performed for the vault side walls and top of an HSM and the HDCS. This analysis showed that the combined thermal resistance of the HSM vault from the heat shield to the outside of the concrete wall was equivalent to the stainless steel HDCS vault wall backed with 6.4 mm (0.25 in.) of high-temperature, alumina-silica insulation. Thus, the analysis includes the effects of the heat shield from radiation and convection. The equivalency of a relatively thin layer of insulation to 0.51 m (20 in.) of reinforced concrete with a heat shield may be realized in large part because the thermal conductivity of the insulation is roughly 30 times less than that of the concrete. Therefore, the two systems will lose thermal energy through the vault walls at the same rate for the same temperature on the HSM heat shield as on the HDCS vault interior wall.

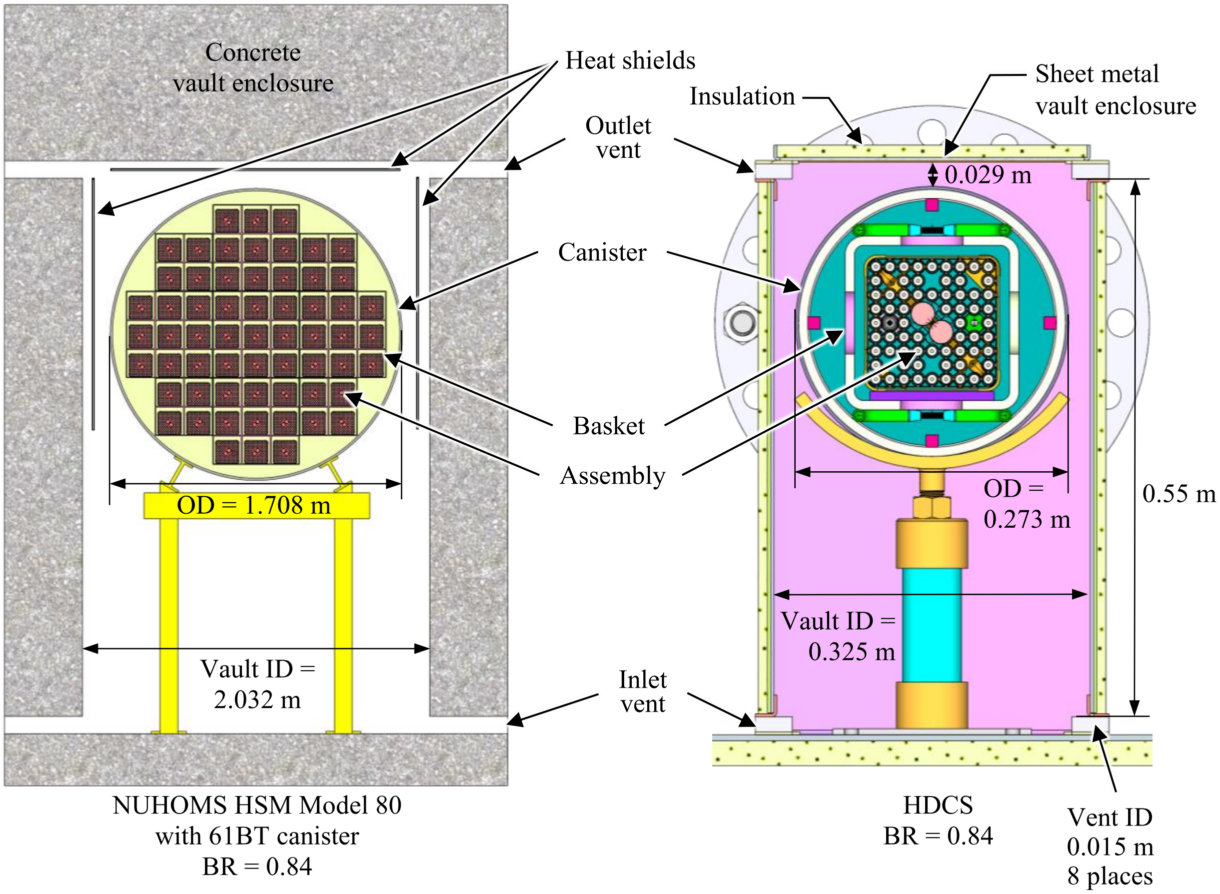

Figure 2.6 Cross sections of a NUHOMS HSM Model 80 and the Horizontal Dry Cask Simulator.

Table 2.1 gives the key parameters for the HDCS at two simulated decay heats and a commercial horizontal storage system. As in previous studies [Durbin and Lindgren, 2018], a known scaling distortion in simulated assembly power is necessary to more closely match the thermal-hydraulic response of a full-sized spent fuel storage cask. This need for additional decay heat is reasonable given the higher external surface-area-to-volume ratio of a single-assembly arrangement as in the HDCS compared to a modern canister with up to eighty-nine assemblies. The air mass flow rate shown for the HDCS is assumed from values measured during similar, vertical test conditions [Durbin and Lindgren, 2018]. The air mass flow rate and other parameters for the commercial horizontal system were taken from a CFD study of various dry storage systems [Solis and Zigh, 2015]. The average velocity, U_{avg}, is calculated by assuming uniform air flow in the vault below the canister. The characteristic length for convection was defined as the canister height for previous vertical testing with the DCS assembly and matched well with vertical, commercial systems. For the current testing in a horizontal configuration, the characteristic length is defined by the outer canister diameter, $D_{canister}$. The significant difference between the HDCS and the commercial canister diameters introduces additional scaling distortions as described next by dimensional analyses.

Table 2.1 Comparison of key dimensional quantities for the HDCS and commercial systems.

Parameter	HDCS		Cask
Power (W)	500	5,000	24,000
$\dot{m}_{Air}$ (kg/s)	0.026	0.069	0.251
$D_{canister}$ (m)	0.273	0.273	1.708
U_{avg} (m/s)	0.019	0.049	0.021

Table 2.2 gives the critical dimensionless groups of the HDCS and a commercial system, namely Reynolds, modified Rayleigh, and Nusselt numbers. As previously noted, the disparity in the canister diameters causes scaling distortions. However, closer examination of the Reynolds numbers indicates that the HDCS and commercial canisters do share the same flow regime. This irregular regime is generally defined for cylinders with $270 < Re_D < 5{,}000$ and is characterized by irregular shedding of von Kármán vortex streets in the cylinder wake. For $Re_D < 1{,}000$ in the irregular regime, the vortices in the near-wake exhibit laminar behavior whereas turbulent dissipation is observed in these vortices for $Re_D > 1{,}000$ [Noack, 1999]. The impact of this difference is expected to be mitigated by the proximity of the vault walls and ceiling.

The modified Rayleigh number is preferred for these analyses because the canister boundary condition is more closely approximated by a uniform heat flux than an isothermal wall temperature. Three-dimensional separation of the cylinder wake defines the onset of the transition to turbulence. Visualization experiments have shown that this important transition occurs when the modified Rayleigh number exceeds 3.5×10^9 [Misumi *et al.*, 2003]. Therefore, the highest power planned for HDCS tests will be transitional if not turbulent as in a commercial system. Power-law fits of Nusselt number to the Rayleigh number are a common treatment for cylinders. Sparrow and Pfeil (1984) offer a series of correlations for symmetrically confined cylinders between vertical walls. These Nusselt numbers for confined cylinders are within an order of magnitude of each other.

Table 2.2 Comparison of dimensionless groups for the HDCS and commercial systems.

Dimensionless Group	HDCS		Cask
Power (W)	500	5,000	24,000
Re_D	280	730	2,000
Ra_D^*	1.3×10^9	1.3×10^{10}	1.4×10^{13}
$Nu_{D,\ Confined}$	30	50	170

2.3 Details of the Heated Fuel Bundle

The highly prototypic fuel assembly was modeled after a 9×9 BWR. Commercial components were purchased to create the assembly including the top and bottom tie plates, spacers, water rods, channel box, and all related assembly hardware (see Figure 2.7). Incoloy heater rods were substituted for the fuel rod pins for heated testing. Due to fabrication constraints the diameter of the Incoloy heaters was slightly smaller than prototypic rods, 10.9 mm (0.430 in.) versus 11.2 mm (0.440 in.). The slightly simplified Incoloy mock fuel rods were fabricated based on drawings and physical examples from the nuclear component supplier. The dimensions of the assembly components are listed below in Table 2.3. The assembly was hydraulically characterized in a previous study [Lindgren and Durbin, 2013].

Table 2.3 Dimensions of assembly components in the mock 9×9 BWR.

Description	Lower (Full) Section	Upper (Partial) Section
Number of pins	74	66
Full heater rod length (m)	3.96	
Partial heater rod length (m)	2.61	
Heater OD (mm)	10.9	
Pin pitch (mm)*	14.4	
Pin separation (mm)	3.48	
Water rod OD (main section) (mm)*	24.9	
Water rod ID (mm)*	23.4	
Channel box length (m)	4.13	
Channel box ID (mm)*	134	
Channel box OD (mm)*	139	
Corner channel box wall (mm)*	2.5	

*[Yamamoto *et al.,* 2002]

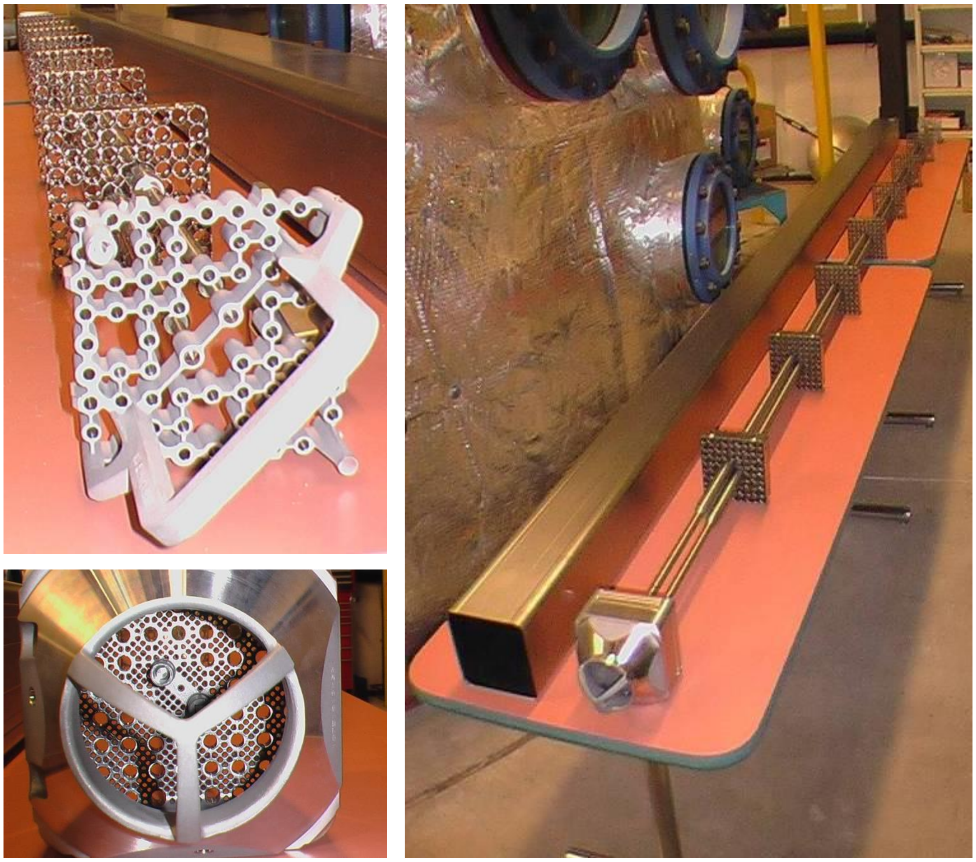

Figure 2.7 Typical 9×9 BWR components used to construct the test assembly including top tie plate (upper left), bottom tie plate (bottom left) and channel box and spacers assembled onto the water rods (right).

2.4 Instrumentation

The test apparatus was instrumented with thermocouples for temperature measurements, pressure transducers for internal gas pressure monitoring, and hot wire anemometers for flow velocity measurements in the exterior ducting. Voltage, amperage, and electrical power transducers were used to monitor electrical energy input to the test assembly.

Ninety-two TCs were previously installed on the BWR test assembly. The TCs used are ungrounded junction type-K with an Incoloy sheath diameter of 0.762 mm (0.030 in.) held in intimate contact with the cladding by a thin Nichrome shim. This shim is spot welded to the cladding as shown in Figure 2.8. The TC attachment method allows the direct measurement of the cladding temperature. Details of the BWR test assembly and TC locations are described below and elsewhere [Lindgren and Durbin, 2013]. Additional TCs were installed on the other major components of the test apparatus such as the channel box, storage basket, canister wall, and exterior air ducting. TC placement on these components was designed to correspond with the existing TC placement in the BWR assembly.

Figure 2.8 Typical TC attachment to heater rod.

Hot wire anemometers were chosen to measure the inlet flow rate because this type of instrument is sensitive and robust while introducing almost no unrecoverable flow losses. Due to the nature of the hot wire measurements, best results are achieved when the probe is placed in an isothermal, unheated gas flow. Hot wires were used to map the two-dimensional flow field across the inlet ducts. As was implemented in the previous study [Durbin and Lindgren, 2018], these hot wires were traversed with computer-controlled stages.

2.4.1 Thermocouples

2.4.1.1 BWR Assembly TC Locations

The existing electrically heated prototypic BWR Incoloy-clad test assembly was previously instrumented with thermocouples in a layout shown in Figure 2.9. The TC naming convention is based on the alpha-alpha grid shown along the top and right-hand sides of the plan views shown in Figure 2.9b. As examples, the locations are shown for the TC on heater rod CS and the TC on the water rod at EU (WEU). Also shown with the plan views are the relative location of the four Quadrants and the elevations applicable for each of the three plan views.

The assembly TCs are arranged in axial and transverse arrays. The axial cross-section is depicted in Figure 2.9a and transverse cross-sections are shown in Figure 2.9b. The axial array A1 has TCs nominally spaced every 0.152 m (6 in.) starting from the top of the bottom tie plate ($z_o = 0$ reference plane). Axial array A2 has TCs nominally spaced every 0.305 m (12 in.) and the transverse arrays are nominally spaced every 0.610 m (24 in.). The spacings are referred to as nominal due to a deviation at the 3.023 m (119 in.)

elevation because of interference by a spacer. Note that the TCs in the axial array intersect with the transverse arrays.

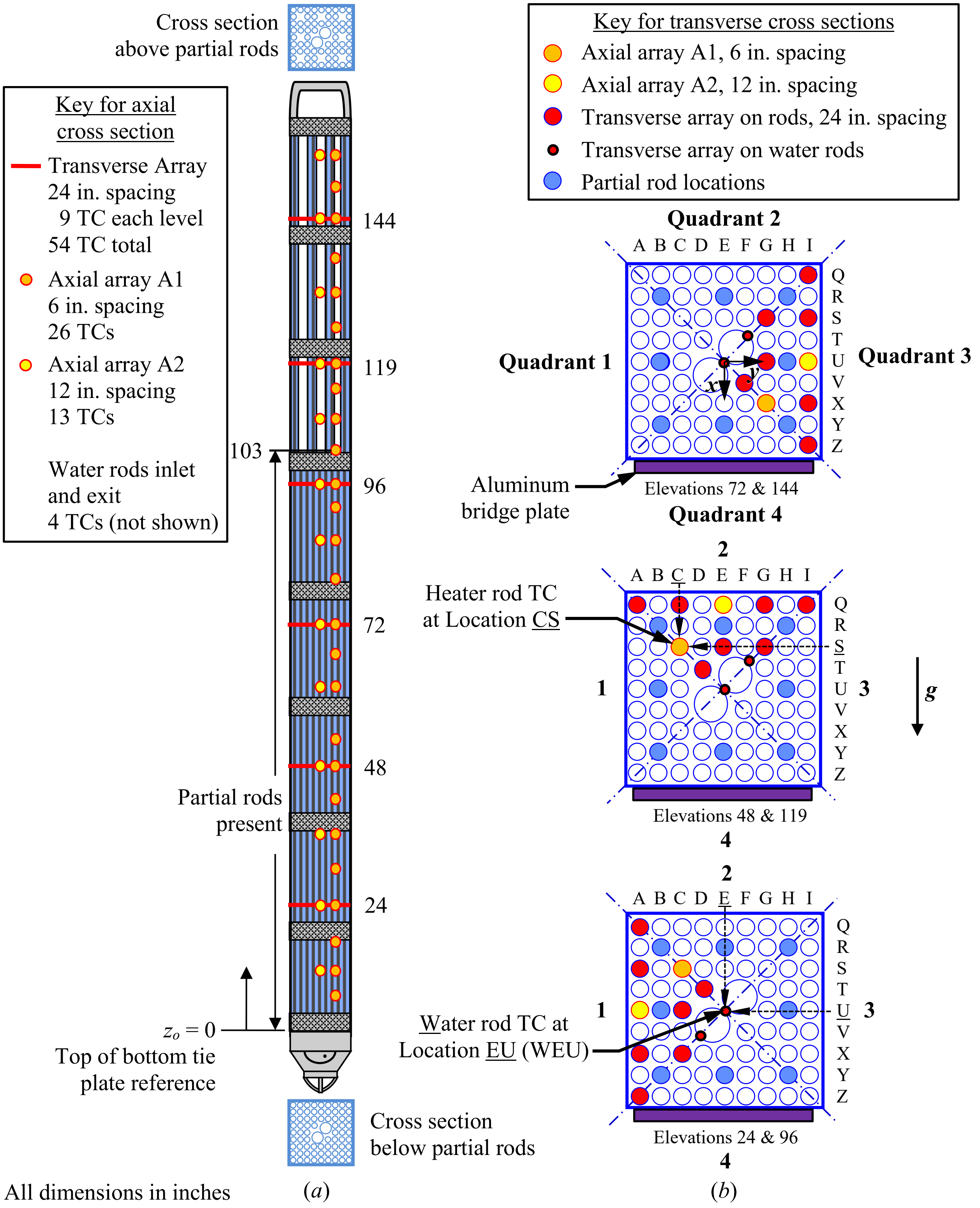

Figure 2.9 Experimental BWR assembly showing as-built *a*) axial and *b*) transverse thermocouple locations.

Based on the need to optimally balance the TC routing through the assembly, the axial and transverse arrays of TCs were distributed among three separate quadrants relying on the assumption of axial symmetry that was valid for the initial, vertical orientation studied previously. However, the assumption of axial symmetry is not valid in the horizontal orientation. Based on the previous vertical orientation of the test apparatus inside of the CYBL vessel, the assembly was laid on the aluminum bridge plate on Quadrant 4, which lacks any TCs in the tube bundle. In the horizontal orientation, there is symmetry between Quadrants 1 and 3, and the peak cladding temperature was expected to be in Quadrant 2.

Figure 2.10 shows the definition of the reference coordinate system. The reference origin is defined as the center of the top surface of the bottom tie plate. The x-axis is positive in the direction of Quadrant 4 and negative in the direction of Quadrant 2. The y-axis is positive in the direction of Quadrant 3 and negative in the direction of Quadrant 1.

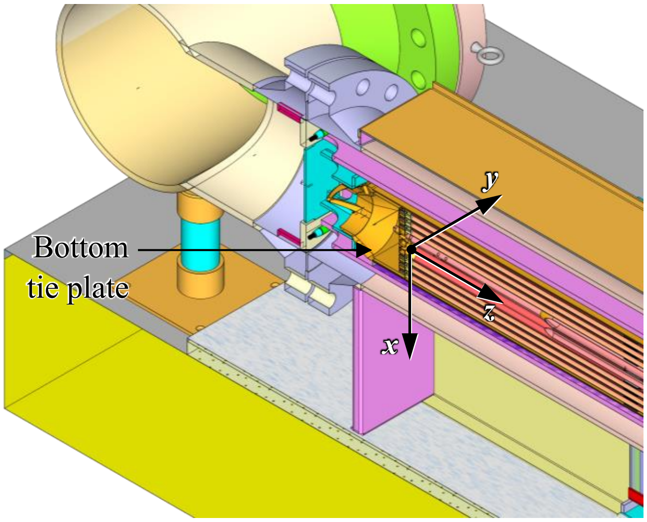

Figure 2.10 Definition of coordinate references in test apparatus.

2.4.1.2 BWR Channel Box TC Locations

The BWR channel box was instrumented with 25 TCs as depicted in Figure 2.11. Twenty-one of the TCs are on the channel faces, three are on the corners and one is on the pedestal. The TCs on the faces of the channel box are nominally located at $|x|$, $|y| = 0.069, 0$ m (2.704, 0 in.) or $|x|$, $|y| = 0, 0.069$ m (0, 2.704 in.) depending on the quadrant in which they are placed. TCs on the corners are nominally located at $|x|$, $|y| = 0.065, 0.065$ m (2.564, 2.564 in.). The reference plane, z_o, is measured from the top of the bottom tie plate, the same as the BWR assembly. In the horizontal orientation, Quadrant 4 is down.

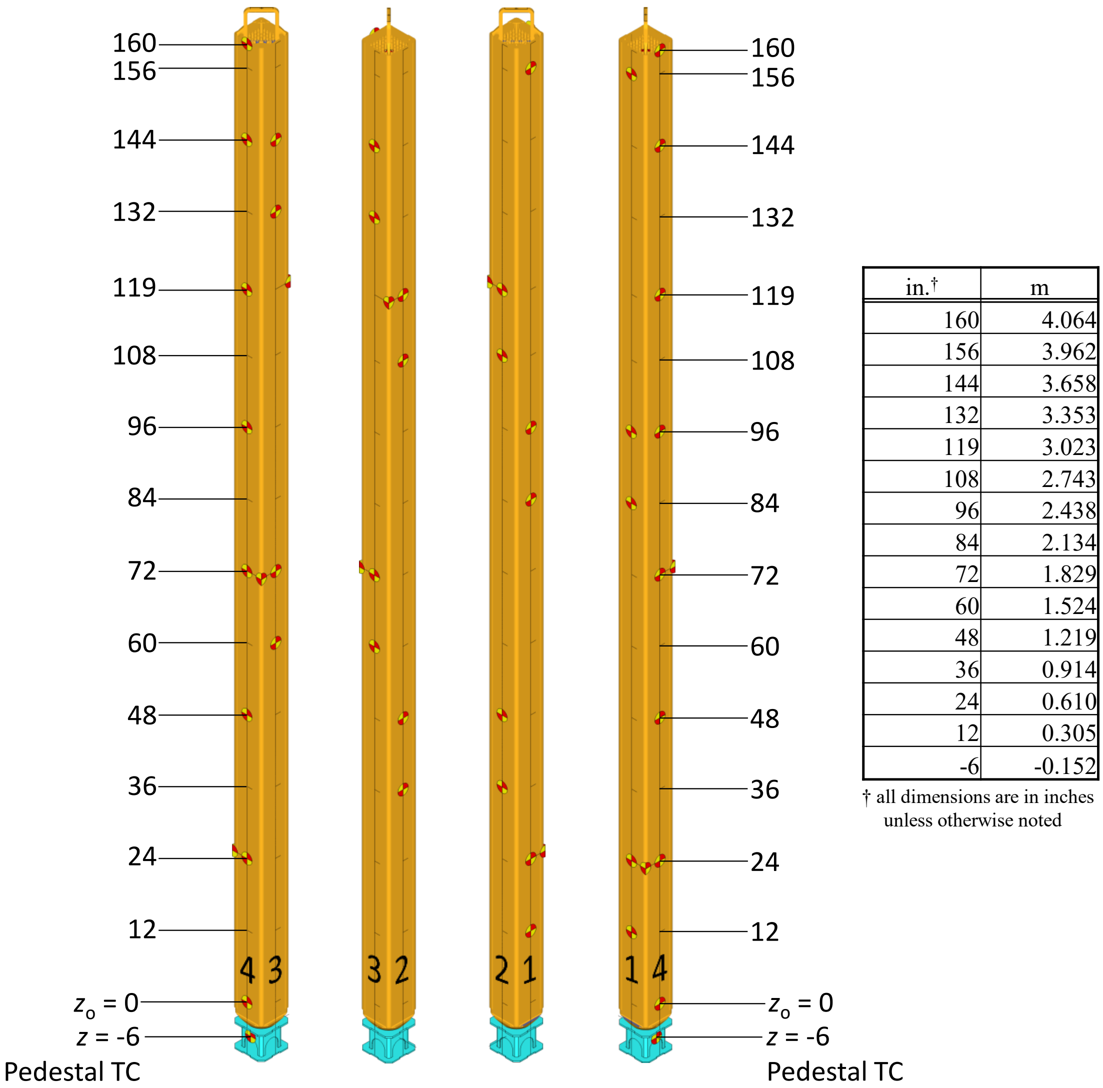

in.†	m
160	4.064
156	3.962
144	3.658
132	3.353
119	3.023
108	2.743
96	2.438
84	2.134
72	1.829
60	1.524
48	1.219
36	0.914
24	0.610
12	0.305
-6	-0.152

† all dimensions are in inches unless otherwise noted

Figure 2.11 BWR channel box showing thermocouple locations.

2.4.1.3 Storage Basket TC Locations

The storage basket is instrumented with 26 TCs as depicted in Figure 2.12. Twenty-one of the TCs are on the basket faces at the same positions as on the channel box, four are on the corners (the corner TC at the 4.191 m (165 in.) level does not correspond to a channel box TC) and one is on the basket face at the elevation of the pedestal. TCs located on the basket faces are nominally located at $|x|$, $|y| = 0$, 0.089 m (0, 3.5 in.) and $|x|$, $|y| = 0.089$, 0 m (3.5, 0 in.). TCs on the corners are nominally located at $|x|$, $|y| = 0.083$, 0.083 m (3.281, 3.281 in.) The reference plane, z_o, is measured from the top of the bottom tie plate. The coordinates given are with respect to the test apparatus reference origin, as shown in Figure 2.10.

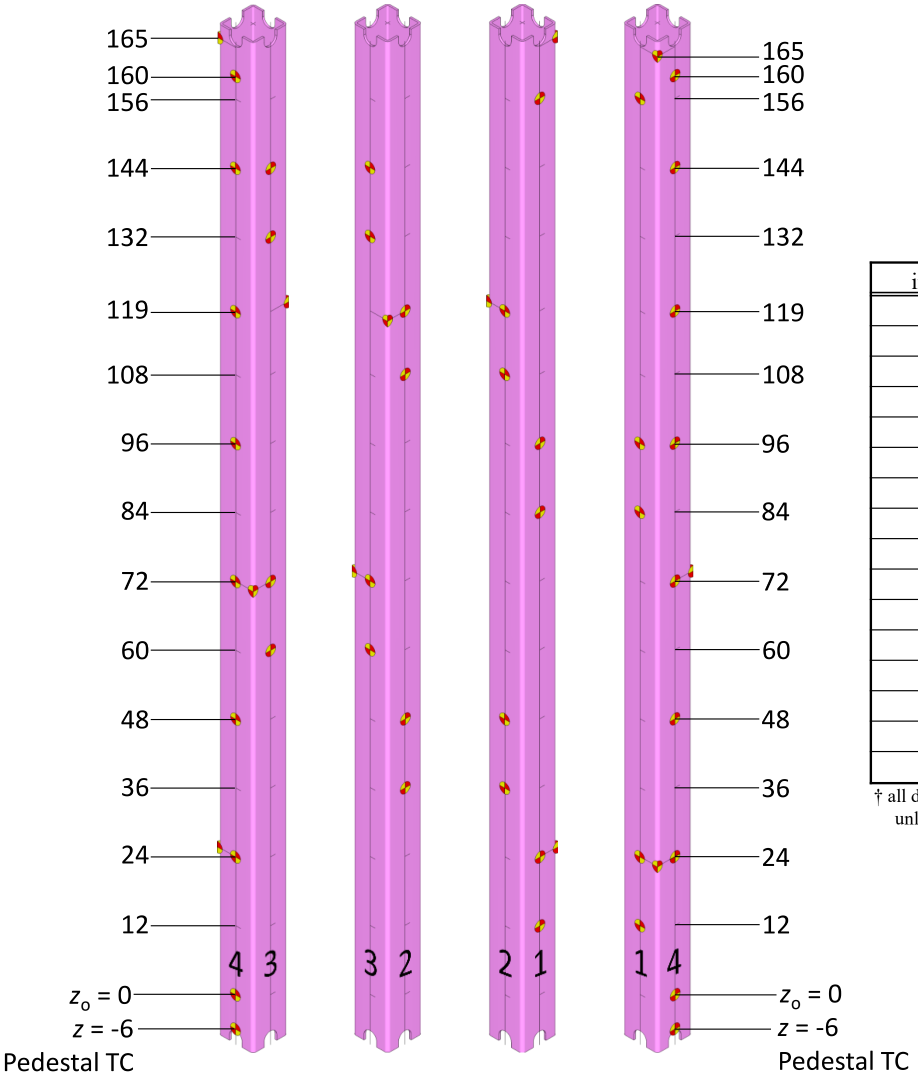

in.†	m
165	4.191
160	4.064
156	3.962
144	3.658
132	3.353
119	3.023
108	2.743
96	2.438
84	2.134
72	1.829
60	1.524
48	1.219
36	0.914
24	0.610
12	0.305
-6	-0.152

† all dimensions are in inches unless otherwise noted

Figure 2.12 Storage basket showing thermocouple locations.

2.4.1.4 Pressure Vessel TC Locations

The pressure vessel was instrumented with 27 TCs as depicted in Figure 2.13. Twenty-four of the TCs are aligned with the TCs on the storage basket faces and three are aligned with the TCs on the storage basket corners. TCs aligned with the storage basket faces are nominally located at $|x|$, $|y|$ = 0, 0.137 m (0, 5.375 in.) and $|x|$, $|y|$ = 0.137, 0 m (5.375, 0 in.). TCs aligned with the storage basket corners are nominally located at $|x|$, $|y|$ = 0.097, 0.097 m (3.801, 3.801 in.). The reference plane, z_o, is measured from the top of the bottom tie plate. The coordinates given are with respect to the test apparatus reference origin, as shown in Figure 2.10.

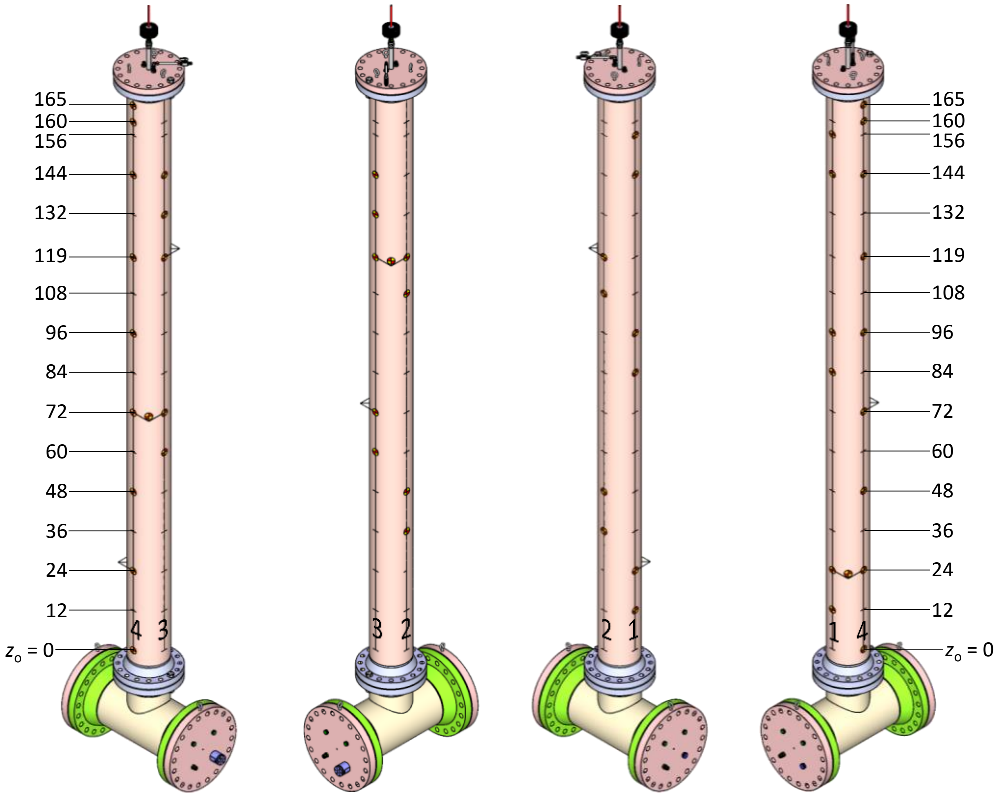

in.†	m
165	4.191
160	4.064
156	3.962
144	3.658
132	3.353
119	3.023
108	2.743
96	2.438
84	2.134
72	1.829
60	1.524
48	1.219
36	0.914
24	0.610
12	0.305

† all dimensions are in inches unless otherwise noted

Figure 2.13 Pressure vessel showing thermocouple locations.

2.4.1.5 Vault Enclosure and External TC Locations

The vault enclosure and the external ambient temperature regions are instrumented with 106 TCs, with some TCs shown in Figure 2.14 and Figure 2.15 and a comprehensive list included in Appendix F. Fourteen of the TCs are aligned along the centerline of the top lid at 0.305 m (12.0 in.) spacing. Twelve TCs are arranged in eight vertical arrays on the external side of the vault at nominally 0.610 m (24.0 in.) spacing. Twelve more TCs are placed on the opposite external side at nominally 0.610 m (24.0 in.) as well. Three TCs are placed internal to the vault at z = 2.13 m (84.0 in.) – two of these TCs are placed on the internal side of the side ribs at this axial location, and the remaining TC is placed on the internal side of the top lid. The alternating, one-two TC layout pattern on the vertical side in Figure 2.14 is reversed (two-one) on the vertical side not shown. The TC locations for both sides of the vault are shown in Appendix F. Nine TCs are placed along the baseplate that forms the bottom of the vault. One TC is placed on each of the four endplates of the vault (which adds up to 4 TCs total on all endplates). Ten gas TCs are placed around the pressure vessel, baseplate, and vault. Twenty gas TCs are placed internally within the vault inlets and outlets. Four TCs are placed around the HDCS instrumentation, and eighteen TCs are placed external to the vault to measure ambient temperatures. The reference plane, z_o, is measured from the top of the bottom tie plate.

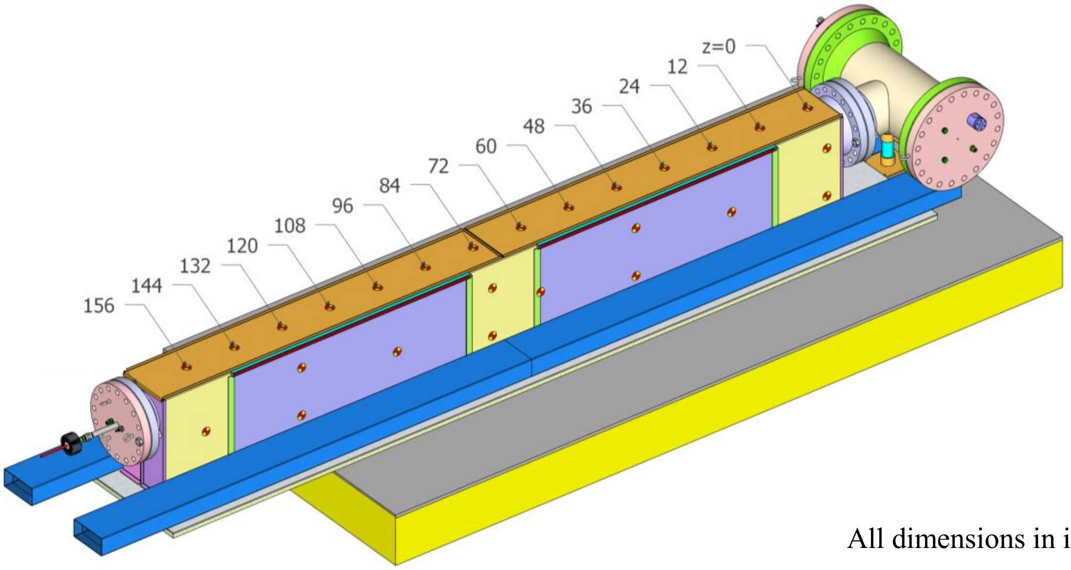

Figure 2.14 Vault without insulation showing thermocouple locations on the top and north sides.

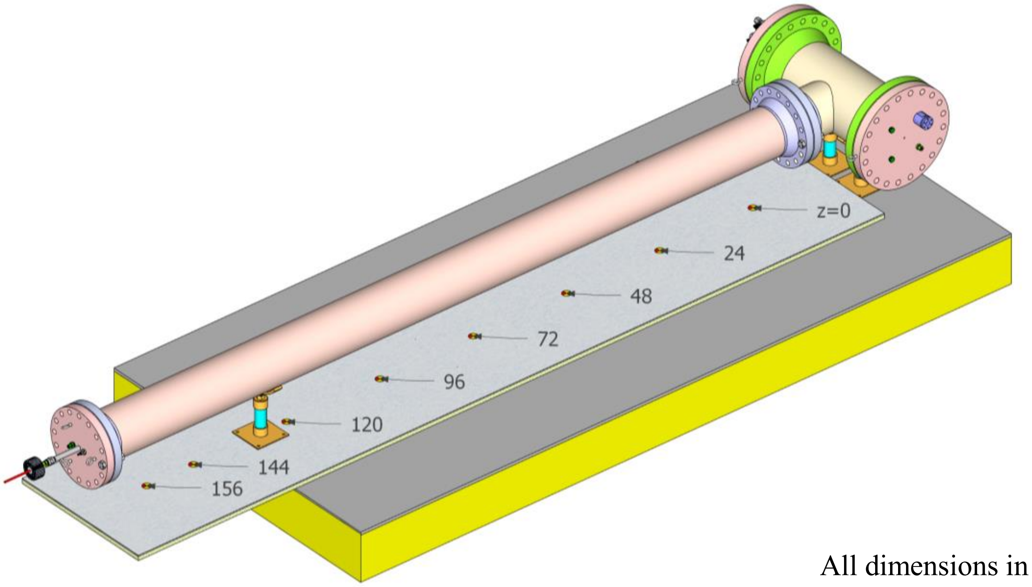

Figure 2.15 Base plate thermocouple locations.

2.4.2 Pressure and Pressure Vessel Leak Rates

Two high-accuracy 0 to 1,034 kPa (0 to 150 psia) absolute pressure transducers (Setra Systems ASM1-150P-A-1M-2C-03-A-01) are installed in the instrument well. The pressure measurements are made in duplicate due of the importance of the measurement. The experimental uncertainty associated with these gauges is ±0.05% of full scale, or ±0.52 kPa (±0.075 psi).

All penetrations and fittings were selected for the apparatus to have helium leak rates of 1×10^{-6} std. cm^3/s or better at 100 kPa. In addition, spiral-wound gaskets capable of leak rates of better than 1×10^{-7} std. cm^3/s were used to form the seals at each flange. The ANSI N14.5 leak rate of 1×10^{-4} std. cm^3/s [ANSI, 2014] would result in an observable pressure drop of 0.03 kPa (4×10^{-3} psi) after a one-week period, which is far below the experimental uncertainty of 0.52 kPa (0.075 psi). During previous testing, leaks in the as-built apparatus were identified and repaired as best as possible [Durbin and Lindgren, 2018]. Ultimately, a small leak path of undetermined origin remains, and a positive pressure control system was implemented to maintain pressure as described next.

2.4.2.1 Pressure Control

A pressure control system has been implemented using the high-accuracy, absolute-pressure transducers, three low-flow needle valves, and three positive-shutoff actuator valves under control of the LabView DAC system. Two actuator valves (vent) control flow out of the vessel, and the third valve (fill) controls the fill gas flow into the vessel. As the vessel heats up, the expanding backfill gas vents out of the first actuator and needle valve to maintain a constant pressure. A second vent valve (overflow) activates if the vessel continues to pressurize. As steady state is reached, the small leak will slowly reduce the backfill pressure, at which point the control system opens the third actuator valve (fill) to allow a small flow through the third needle valve. Overall, a similar pressure control system used in past testing was able to maintain the vessel pressure constant to within ±0.3 kPa (0.044 psi).

2.4.2.2 Pressure Vessel Internal Volume Measurement

The pressure vessel internal volume was measured during previous testing [Durbin and Lindgren, 2018]. The total internal volume was determined to be 252.0 liters, with an uncertainty of ±2.6 liters. This measurement includes the volume of the instrument well that is insulated from the heated test section.

2.4.3 Power Control

A diagram of the test assembly power control system is shown in Figure 2.16 and the details inside the instrument panel are shown in Figure 2.17. The electrical voltage and current delivered to the test assembly heaters is controlled to maintain a constant power by a digital silicon-controlled rectifier (SCR). The data acquisition (DAQ) system provides a power setpoint to the SCR that is constantly compared to the measured output power. The power, voltage, and current measurements are collected by the DAQ. The details of the instrumentation used to control and measure the electrical power are provided in Table 2.4. A special calibration schedule of thirty-two points was ordered for the power diagnostic (Ohio Semitronics PTB-112D1PCY48). The observed 95% uncertainty based of the Student’s t-value and the standard error of the regression for this instrument give an uncertainty of $U_{\text{Watt}} = \pm 13$ W. Additional details may be found in Appendix A.

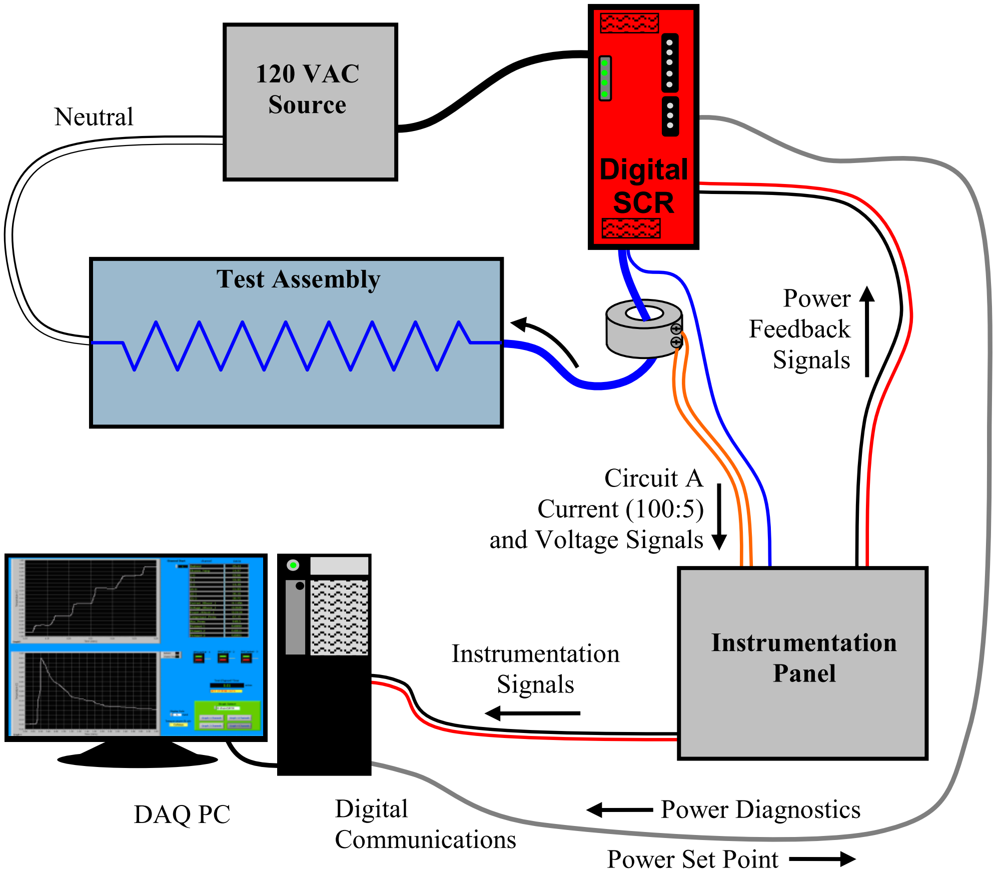

Figure 2.16 **Power control system and test circuits.**

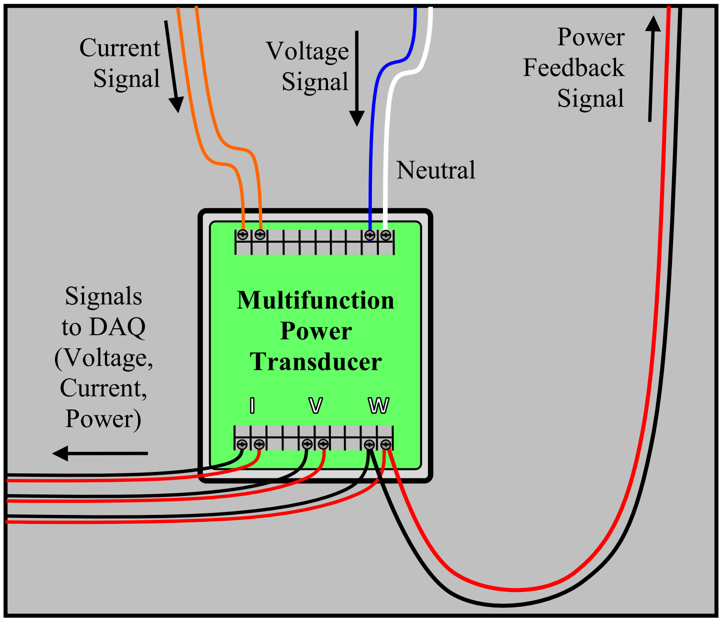

Figure 2.17 **Schematic of the instrumentation panel for voltage, current, and power measurements.**

Table 2.4 List of power control equipment.

Description	Manufacturer	Model
Power Test Board (PTB) – Measures Volts, Amps, Watts	Ohio Semitronics	PTB-112D1PCY48
Digital SCR Power Controller	Control Concepts	uF1HXLGI-130-P1RSZ

2.4.4 Hotwires

The hotwire anemometers used are TSI model 8455 where the tip detail is shown in Figure 2.18. For scale, the largest shaft diameter shown is 6 mm (0.25 in.). The sensing element of the model 8455 is protected inside of an open cage and is sensitive to flows down to 0.13 m/s (25 ft/min) with a response time of 0.2 seconds.

Figure 2.18 Photograph of the hot wire anemometer tip.

2.5 Air Mass Flow Rate

Figure 2.19 shows the air flow pattern through the HDCS vault. Cold air is drawn into the air inlet ducts and flows into the vault inlets on the sides of the enclosure. The air heats as it passes between the vault and the simulated canister. The hot air exhausts at the top of the enclosure sides via the vault outlets. The hotwires are mounted on motorized stages (Velmex Stage XN10-0040-M02-71, Motor PK245-01AA). The data acquisition computer communicated with the stage controller (Velmex Controller VXM-4) to identify and verify hot wire positioning.

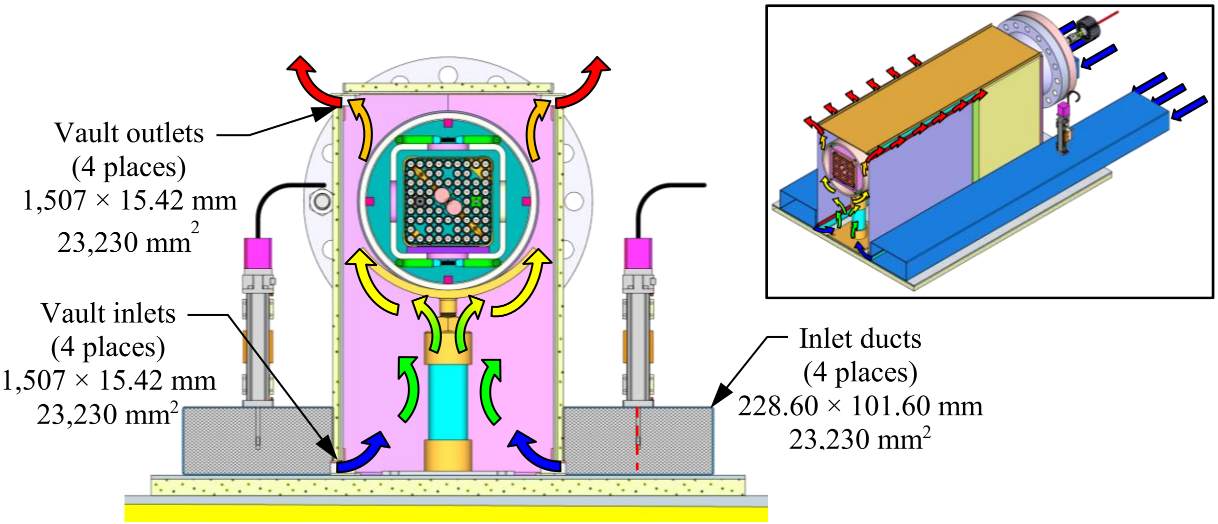

Figure 2.19 Air flow pattern in the HDCS from natural convection.

The methods for determining the induced air flow in the HDCS are based on the successful methods developed in the previous aboveground and belowground, vertical DCS studies [Durbin and Lindgren, 2018]. The methods used hot wire anemometers to measure inlet air velocity and subsequently calculate an overall air mass flow rate.

2.5.1 Flow Straightening

To obtain the most stable and repeatable measurements possible, a honeycomb element is inserted into all four assembly inlets to align the flow in the desired direction and reduce any flow disturbances on the hot wire anemometers. As shown in Figure 2.20, a plastic honeycomb element was chosen with a cell diameter, wall thickness, and flow length of 3.8, 0.1, and 25.8 mm (0.150, 0.004, and 1.015 in.), respectively. This type of flow straightening element has been found to provide the greatest reduction in hot wire fluctuations while introducing the smallest pressure drop to the system. The effective, frictional coefficient for this honeycomb material was found to be $D = 2.7 \times 10^6$ m^{-2} for porous media in CFD simulations.

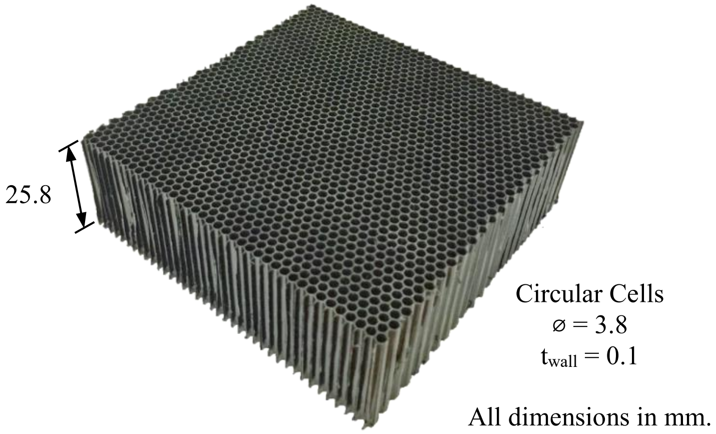

Figure 2.20 Photograph of the honeycomb element used for flow straightening.

As depicted in Figure 2.21, the flow straightener section featured a convergent nozzle made of corrugated fiberboard and scrim-backed, pressure-sensitive tape to minimize the flow losses associated with the honeycomb element by increasing the flow area by a factor of four. The honeycomb dimensions used in each of the four inlets was 0.425 m (16.7 in.) tall by 0.233 m (9.2 in.) wide and 0.0258 m (1.02 in.) thick for a flow area of 0.099 m^2. The nozzle design included two straight sections to accommodate the honeycomb and the assembly inlet. Long-sweep arcs with matching tangents at the inflection point were chosen to provide a smooth transition from the honeycomb section to the assembly inlet. A detailed mechanical drawing can be found in Appendix B.3.

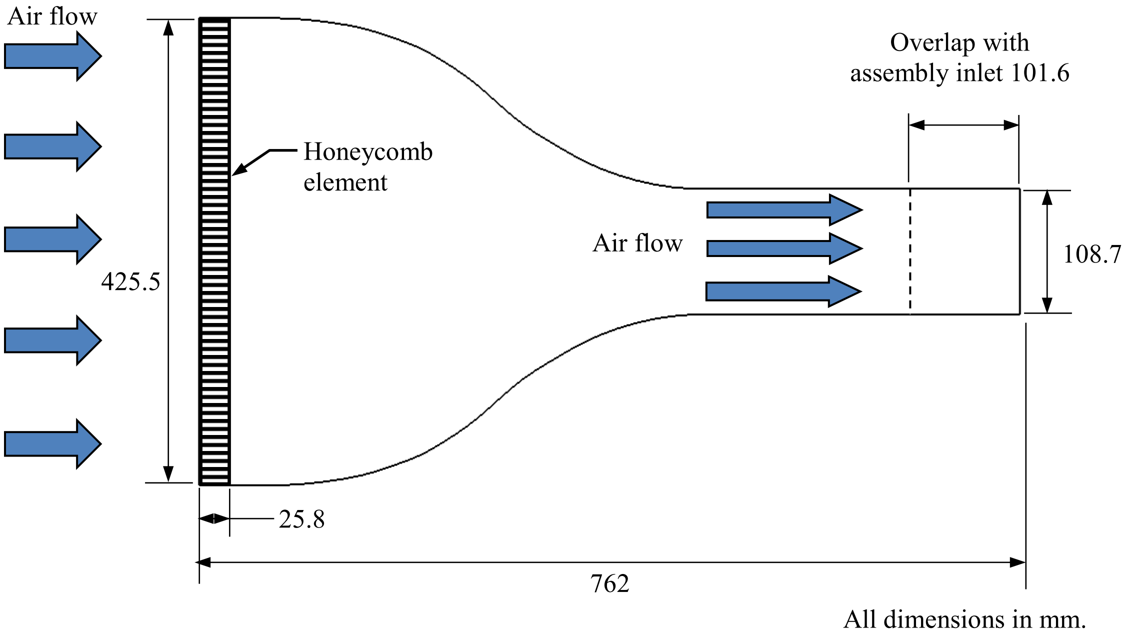

Figure 2.21 Cutaway schematic of the flow straightener.

2.5.2 Air Flow Measurement

The inlet flow straightening nozzles and hot wire anemometer locations for the HDCS are depicted in Figure 2.22. After the four convergent nozzles, rectangular ducts with nominal cross-sectional dimensions of 0.229 m (9.00 in.) by 0.102 m (4.00 in.) convey the inlet flow into the simulated vault. Multiple hot wire anemometers are located nominally 0.5400 m (21.25 in.) downstream from the inlet of each duct to map the inlet air flow. Shown is a single representative motorized stage and hot wire anemometers on each duct.

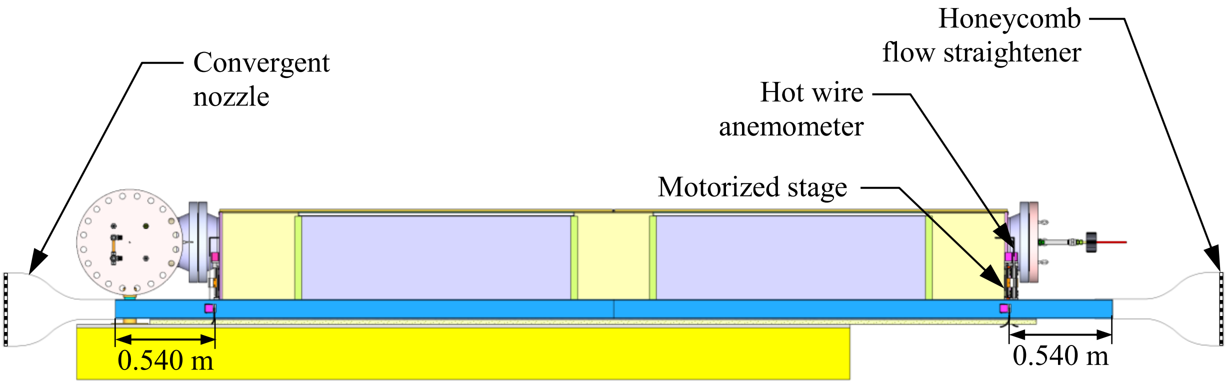

Figure 2.22 Flow straightening nozzles and hot wire anemometer locations in the inlet ducts.

There are at least three (and in one duct four) hot wire anemometers on motorized stages as illustrated in Figure 2.23. Each duct has a vertical hot wire anemometer that traverses across the center of the duct in the *x*-direction and a horizontal hot wire anemometer that traverses across the center of the duct in the *y*-direction 25.4 mm (1.00 in.) farther downstream. Additionally, the NE duct and the SW duct have a vertical hot wire anemometer that traverses in the *x*-direction 9.5 mm (0.38 in.) from the outer duct wall, the NW duct has a vertical hot wire anemometer that traverses in the *x*-direction 9.5 mm (0.38 in.) from the inner duct wall, and the SE duct has two additional vertical hot wire anemometers that traverses in the *x*-direction 9.5 mm (0.38 in.) from both the inner and outer duct walls.

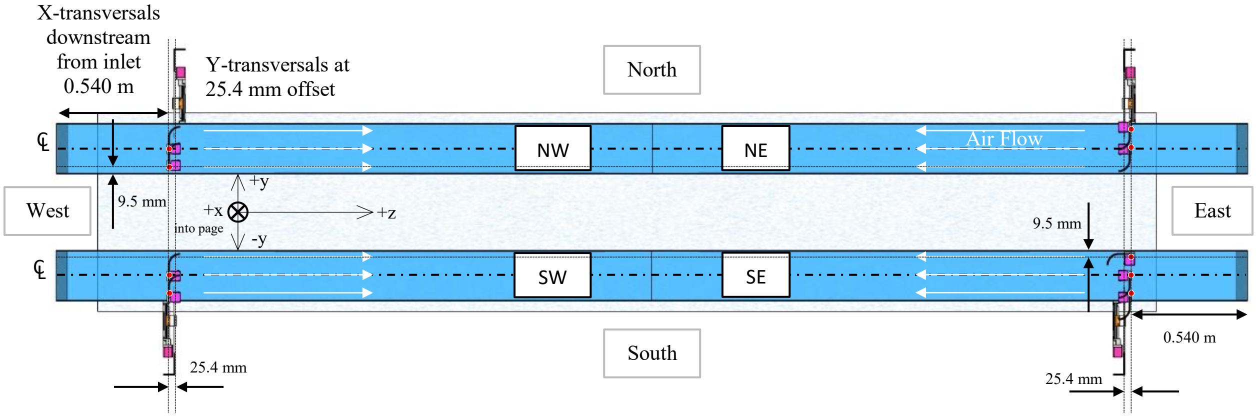

Figure 2.23 Plan view location details of hotwire anemometers in the inlet ducts.

The measured steady-state velocities in all four ducts were averaged and used to determine a 2-dimensional distribution of average duct velocity across the duct flow area. The duct flow area is discretized into rectangular elements with a flow velocity determination associated with the center of each element as illustrated in Figure 2.24. The values shown in green are derived from the vertical traverses. The values shown in blue are derived from the horizontal traverse. The values shown in yellow are derived by similarity with the horizontal and vertical velocity profile measurements. The region shown in red on the periphery is the no-slip region with no flow along the outer walls.

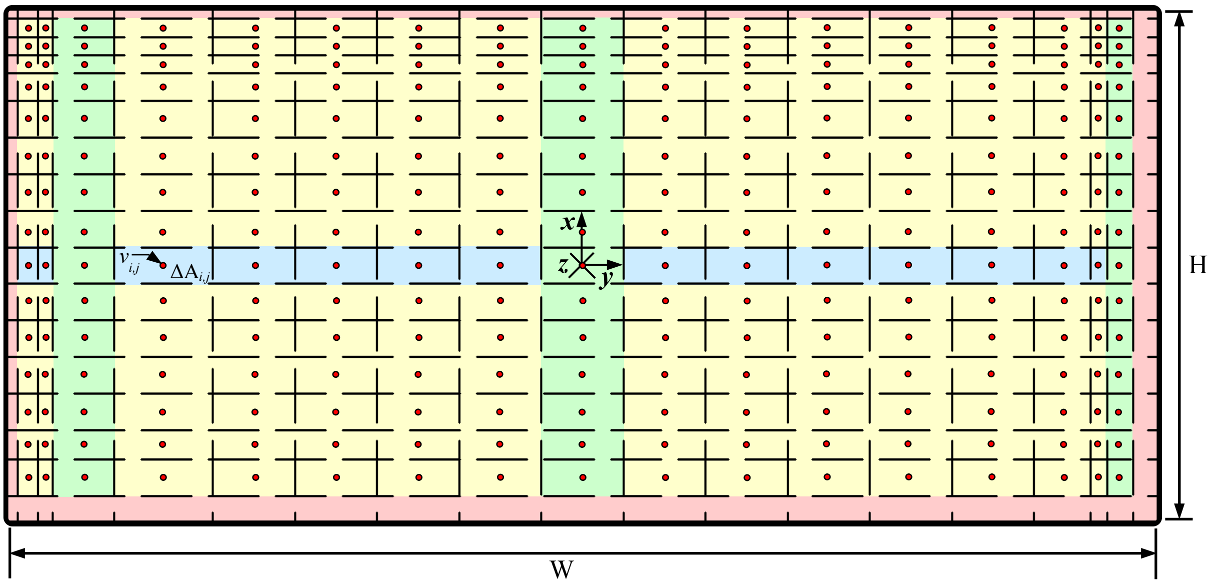

Figure 2.24 Diagram showing the integration scheme for the calculation of air mass flow rate at the inlet.

Value derived from horizontal measurement, vertical measurement, similarity, and no-slip.

Each velocity was assumed to be constant across the differential area, $\Delta A_{i,j}$, defined by the coordinates of $\left(\frac{x_i+x_{i-1}}{2},\frac{y_j+y_{j-1}}{2}\right)$ and $\left(\frac{x_i+x_{i+1}}{2},\frac{y_j+y_{j+1}}{2}\right)$ where *i* is the *x*-coordinate index and *j* is the *y*-coordinate index.

The integrated, natural air mass flow rate is given in Equation 2.1. The reference density is defined by the standard conditions for the TSI hot wires, or $\rho_{ref} = 1.2$ kg/m^3 at 21.1 °C and 101.4 kPa. Using this midpoint approximation scheme, the no-slip condition is assumed to apply to the area half-way between the wall and the nearest available velocity values. Applying the no-slip condition in this manner equates to assuming the velocity varies linearly between zero at the wall to the nearest measured value, which is expected to underestimate the flow rate based on comparisons with boundary layer theory.

$$\dot{m}_{\mathrm{Tot}} = \sum_{j=1}^{17} \sum_{i=1}^{19} \rho_{\mathrm{ref}} \cdot \Delta \mathrm{A}_{i,j} \cdot v_{i,j} \qquad 2.1$$

Table 2.5 gives differential area, $\Delta A_{i,j}$, by location in the inlet. These differential areas are used for all calculations of air mass flow rate as defined in Equation 2.1. The measured locations of the hot wire anemometers were used to determine each differential area.

Table 2.5 Differential areas for the calculation of air mass flow rate.

All values in mm^2.

y (mm) / *x* (mm)	-113.2	-110.2	-106.1	-104.6	-81.6	-65.3	-49.0	-32.6	-16.3	0.0	16.3	32.6	49.0	65.3	81.6	97.9	104.1	104.6	111.8
50.4	4	7	5	22	36	30	30	30	30	30	30	30	30	30	30	21	6	9	9
47.7	7	15	10	45	72	60	60	60	60	60	60	60	60	60	60	41	12	19	18
44.0	7	15	10	45	72	60	60	60	60	60	60	60	60	60	60	41	12	19	18
40.3	7	15	10	45	72	60	60	60	60	60	60	60	60	60	60	41	12	19	18
36.7	11	22	15	67	108	90	90	90	90	90	90	90	90	90	90	62	18	28	27
29.3	15	30	21	90	144	120	120	120	120	120	120	120	120	120	120	82	24	37	35
22.0	15	30	21	90	144	120	120	120	120	120	120	120	120	120	120	82	24	37	35
14.7	15	30	21	90	144	120	120	120	120	120	120	120	120	120	120	82	24	37	35
7.3	15	30	21	90	144	120	120	120	120	120	120	120	120	120	120	82	24	37	35
0.0	15	30	21	90	144	120	120	120	120	120	120	120	120	120	120	82	24	37	36
-7.3	15	30	21	90	144	120	120	120	120	120	120	120	120	120	120	82	24	37	36
-14.7	15	30	21	90	144	120	120	120	120	120	120	120	120	120	120	82	24	37	35
-22.0	15	30	21	90	144	120	120	120	120	120	120	120	120	120	120	82	24	37	35
-29.3	15	30	21	90	144	120	120	120	120	120	120	120	120	120	120	82	24	37	35
-36.7	12	24	17	72	116	96	96	96	96	96	96	96	96	96	96	66	20	30	29
-41.1	15	30	21	90	144	120	120	120	120	120	120	120	120	120	120	82	24	37	35
-48.8	10	21	14	62	100	83	83	83	83	83	83	83	83	83	83	57	17	26	25

2.6 Test Matrix

The HDCS test series is comprised of ten test runs as summarized in Table 2.6. Both helium and air were used as fill gases. The fill pressure was either 100 kPa or 800 kPa for helium. For air, the fill pressure was 100 kPa. For air and helium at 100 kPa the assembly was powered at four power levels: 0.50, 1.00, 2.50, and 5.00 kW. For helium at 800 kPa the assembly was powered at either 0.50 or 5.00 kW. The steady-state results of two tests highlighted in grey for 2.50 kW with backfill of 100 kPa of either helium or air are discussed in detail in this report. To facilitate a blind modeling validation exercise, the comparison metrics listed in Table 2.7 are provided for the two runs discussed in this report. Modeling validation participants will be asked to provide the same information calculated for all of the runs listed in Table 2.6.

Table 2.6 HDCS test matrix. Tests with results presented in this in this report are runs highlighted in grey.

Fill Gas	Pressure (kPa)	Power (W)
Helium	100	500
	100	1000
	100	2500
	100	5000
	800	500
	800	5000
Air	100	500
	100	1000
	100	2500
	100	5000

Table 2.7 Proposed steady-state comparison metrics and locations for example data in this report for simulated decay heat of 2.50 kW and two different canister fill gases.

Metric	Notes	Example Data (2.50 kW)	
		He 100 kPa	**Air 100 kPa**
Peak Cladding Temperature	PCT	Table 3.1	Table 3.2
		Figure 3.1	Figure 3.2
PCT - Location	x, y, z	Table 3.1	Table 3.2
		Figure 3.1	Figure 3.2
Air mass flow rate	$\dot{m}_{\mathrm{Air}}$	Table 3.1	Table 3.2
Axial temperature profile	T(z) at WEU (5 locations)	Table 3.3	
		Figure 3.1	Figure 3.2
Transverse x-axis temp. profile	T(x) at z = 48 in. (11 locations)	Table 3.4	
		Figure 3.3	Figure 3.4
Transverse y-axis temp. profile	T(y) at z = 72 in. (7 locations)	Table 3.5	
		Figure 3.5	Figure 3.6

3 STEADY-STATE RESULTS

The criterion for steady state was considered met when the first derivative with respect to time of most TCs in the test apparatus was ≤ 0.3 K/h. The steady state values reported here represent the average of data collected from the point this criterion was met in the majority of data channels and the end of the test.

3.1 Peak Temperatures, Power and Induced Flow

Table 3.1 shows the steady-state results for the 2.50 kW, 100 kPa case with helium as the fill gas. The table lists the average, maximum, minimum, and the standard deviation for the applied power, peak temperatures of the cladding, channel box, storage basket, pressure vessel, vault enclosure, and ambient, as well as the total induced cooling air flow rate. Table 3.2 shows the same steady-state results for the 2.50 kW, 100 kPa case with air as the fill gas. The power for the two tests was essentially the same and stable at 2.50 kW. The induced flow in the helium fill test was slightly higher than in the air-filled test but within experimental error, $U_{\dot{m},\text{ Total}} = \pm 3\times10^{-4}$ kg/s. The steady-state peak temperatures for the components inside the pressure vessel were significantly cooler with the helium fill than with the air fill. The greatest difference was in the fuel bundle where the PCT was 88 K cooler and decreased for components moving outward. The steady-state peak temperatures for the pressure vessel and vault enclosure were essentially the same for the two gas fills. The tables also list the axial location of the peak temperature and the rod or quadrant that the peak temperature occurred (see Figure 2.9 for rod and quadrant naming convention). For the air fill case, the PCT was at a lower axial location (0.61 m) than the other components and was located on Quadrant 2 which is the top face. For the helium fill case, the PCT was on the same rod but at an axial location twice as great and coincided with the axial location of the peak temperature of the other components. For most components the peak temperature was located on the upward face, or Quadrant 2. However, for the basket, the peak temperature was located on the bottom face, or Quadrant 4. As will be discussed in more detail in Section 3.2.2, the temperatures of the top and bottom faces of the storage basket were similar and within experimental error.

Table 3.1 Steady-state peak temperature results for various components in the 2.50 kW 100 kPa case with helium.

	Power (W)	PCT (K)	Channel (K)	Basket (K)	Vessel (K)	Vault (K)	Ambient (K)	Tot. Flow Rate (kg/s)
Average	**2503**	**558.7**	**505.9**	**463.7**	**420.8**	**367.9**	**296.7**	**0.0283**
Max	2515	559.4	506.7	464.7	422.3	370.1	302.3	0.0286
Min	2493	557.9	504.9	462.5	419.4	366.3	294.0	0.0273
Rod or Quadrant #		DT	2	4	2	2 (top)		
z-Location (m)		1.22	1.22	1.22	1.22	1.22		

Table 3.2 Steady-state peak temperature results for various components in the 2.50 kW 100 kPa case with air.

	Power (W)	PCT (K)	Channel (K)	Basket (K)	Vessel (K)	Vault (K)	Ambient (K)	Tot. Flow Rate (kg/s)
Average	**2500**	**647**	**563**	**486**	**420**	**367**	**297**	**0.0277**
Max	2519	647	563	486	421	368	301	0.0280
Min	2484	647	562	486	420	367	295	0.0268
Rod or Quadrant #		DT	2	2	2	2 (top)		
z-Location (m)		0.61	0.91	1.22	1.22	1.22		

3.2 Temperature Profiles

3.2.1 Axial Temperature Profile – T*(z)*

The steady-state internal fuel bundle axial temperature profiles for the 2.50 kW, 100 kPa fill of helium and air are shown in Figure 3.1 and Figure 3.2, respectively and the data presented in the figures is tabulated in Table 3.3. The location of the thermocouples used to produce the profile is indicated on the inset of the fuel bundle cross-section. Most of the TCs are attached to fuel rods CS (blue diamonds) and GX (green triangle). A few TCs are located on the water rods (red squares). The peak cladding temperature is located on rod DT and is indicated by a star symbol. See Figure 2.9 for the heater rod naming convention.

The temperatures in the fuel bundle were all lower with the helium backfill than with the air backfill. The shapes of the axial profiles are similar although the profile is flatter in the lower fully populated bundle in the helium fill case. For both cases the temperature profile drops more steeply with increased axial location after the partial rods end in the bundle at $z = 2.6$ m and again at the end of the heated zone at $z = 3.7$ m.

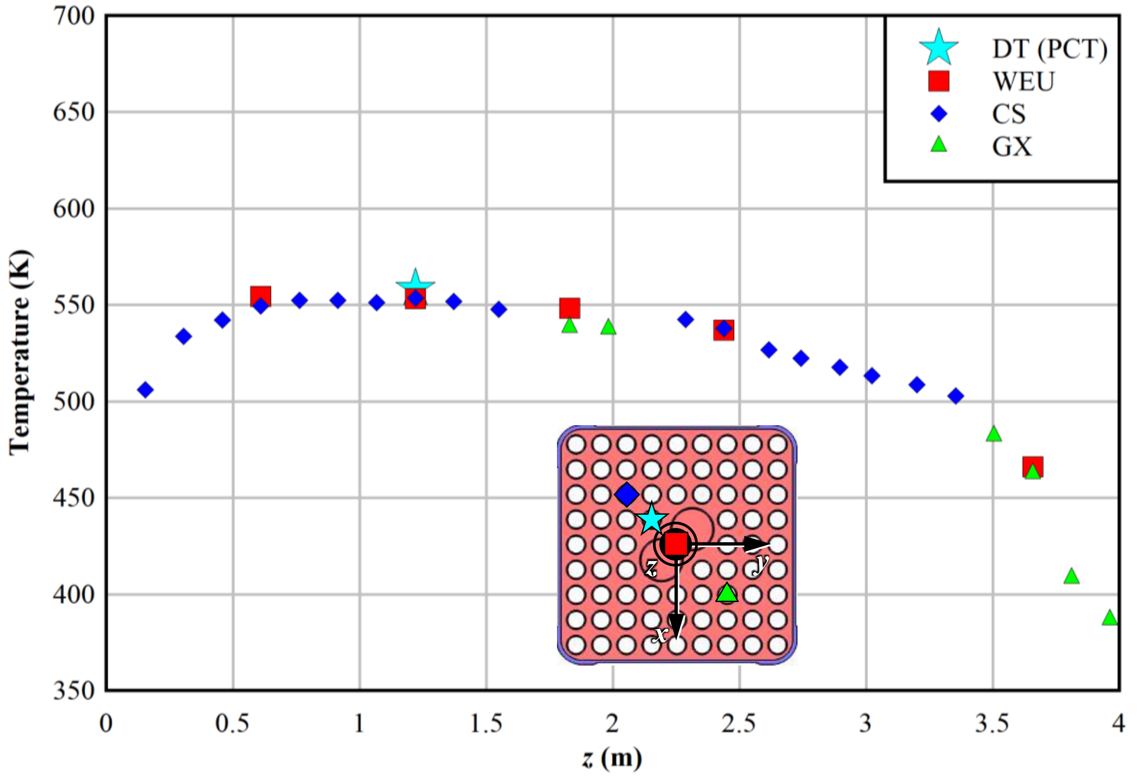

Figure 3.1 Internal temperature profile as a function of *z* for 2.50 kW and helium at 100 kPa.

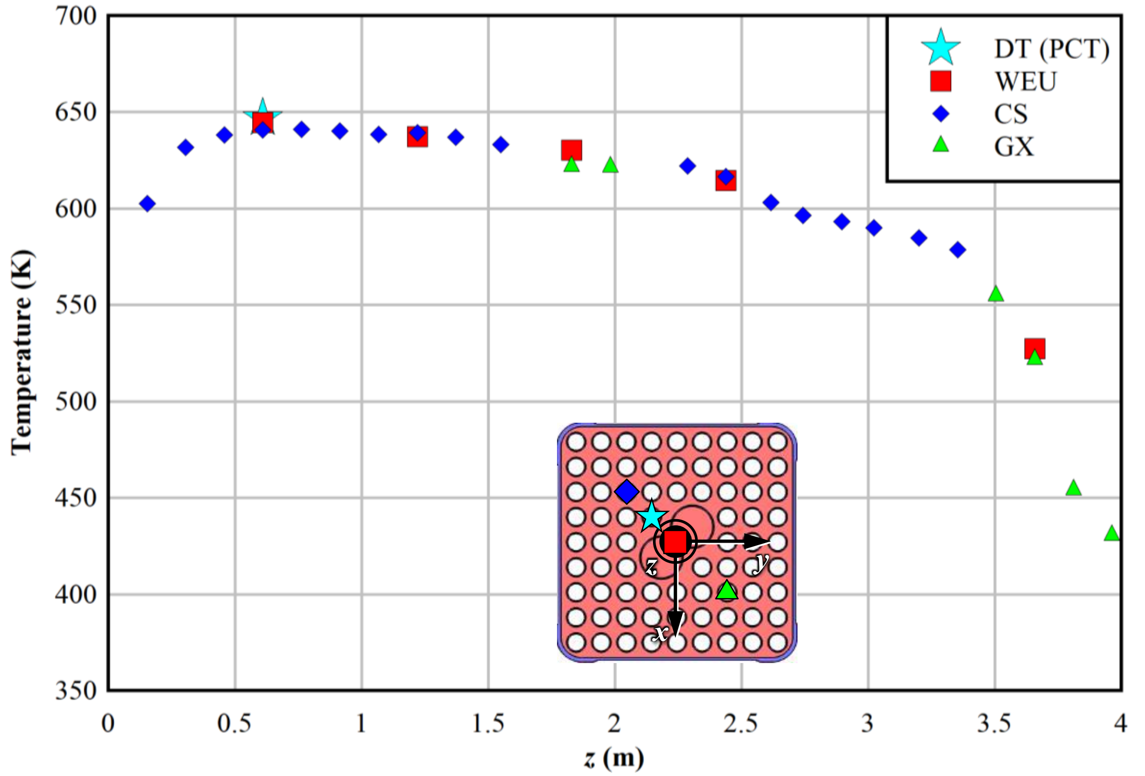

Figure 3.2 Internal temperature profile as a function of *z* for 2.50 kW and air at 100 kPa.

Table 3.3 Internal temperature profile coordinates as a function of the *z*-coordinate for 2.50 kW and 100 kPa for the helium and air test cases.

TC Location	*z* (in.)	*z* (m)	Temperature (K)	
			Helium	Air
DT (PCT)	24.0	0.610	--	647
	48.0	1.219	559	--
WEU	24.0	0.610	555	645
	48.0	1.219	553	637
	72.0	1.829	548	630
	96.0	2.438	537	615
	144.0	3.658	466	527
CS	6.0	0.152	506	603
	12.0	0.305	534	632
	18.0	0.457	542	638
	24.0	0.610	550	641
	30.0	0.762	552	641
	36.0	0.914	552	640
	42.0	1.067	551	638
	48.0	1.219	554	639
	54.0	1.372	552	637
	61.0	1.549	548	633
	90.0	2.286	542	622
	96.0	2.438	538	617
	103.0	2.616	527	603
	108.0	2.743	523	597
	114.0	2.896	518	593
	119.0	3.023	513	590
	126.0	3.200	509	585
	132.0	3.353	503	579
GX	72.0	1.829	538	622
	78.0	1.981	538	622
	138.0	3.505	482	555
	144.0	3.658	463	522
	150.0	3.810	408	454
	156.0	3.962	387	431

3.2.2 Vertical Temperature Profile – T*(x)*

The steady-state vertical temperature data is presented in Table 3.4. The temperature profiles for the 2.50 kW, 100 kPa fill of helium and air are also shown graphically in Figure 3.3 and Figure 3.4, respectively. The scaled inset figure on the right shows the location of the thermocouples. The profile passes through the center line of the apparatus along the *x*-axis at $z = 1.219$ m. TCs are located on the top and bottom of the vault enclosure, pressure vessel, storage basket and channel box. TCs are also located inside the assembly on the water rods and heater rods, ES and EQ (see Figure 2.9 for heater rod naming convention). The peak temperature for both cases was located on rod ES but the peak temperature for the helium fill case was 87 K cooler than the air fill case. For the air case the temperature of the bottom of the storage basket was 1.5 K lower than the top of the storage basket. For the helium case the situation is reversed and the temperature of the bottom of the storage basket was 1.5 K higher than the top of the storage basket. This temperature difference is within the experimental error of the temperature measurement. More significant is the temperature difference between the bottom of the storage basket and the bottom of the channel box. For the air case this temperature difference is 50 K. For the helium case the temperature difference between the channel and the basket is reduced to 13 K indicating much better thermal coupling by the aluminum bridge plate when the gap between the bridge plate and the channel box (see Figure 2.2) is filled with helium. The temperature difference between the basket and the pressure vessel is also less in the helium case.

Table 3.4 Vertical temperature profile coordinates for 2.50 kW, *z* = 1.219 m (48.0 in.), and at 100 kPa for the helium and air test cases.

Location	*x* (in.)	*x* (m)	Temperature (K)	
			Helium	Air
Vault Top	-6.66	-0.169	368	367
Pressure Vessel Top	-5.38	-0.137	421	420
Basket Top	-3.53	-0.090	462	486
Channel Top	-2.70	-0.068	506	562
EQ	-2.26	-0.057	536	617
ES	-1.13	-0.029	558	645
WEU	0.00	0.000	553	637
Channel Bottom	2.70	0.068	477	534
Basket Bottom	3.53	0.090	464	484
Pressure Vessel Bottom	5.38	0.137	414	408
Vault Bottom	16.6	0.421	323	321

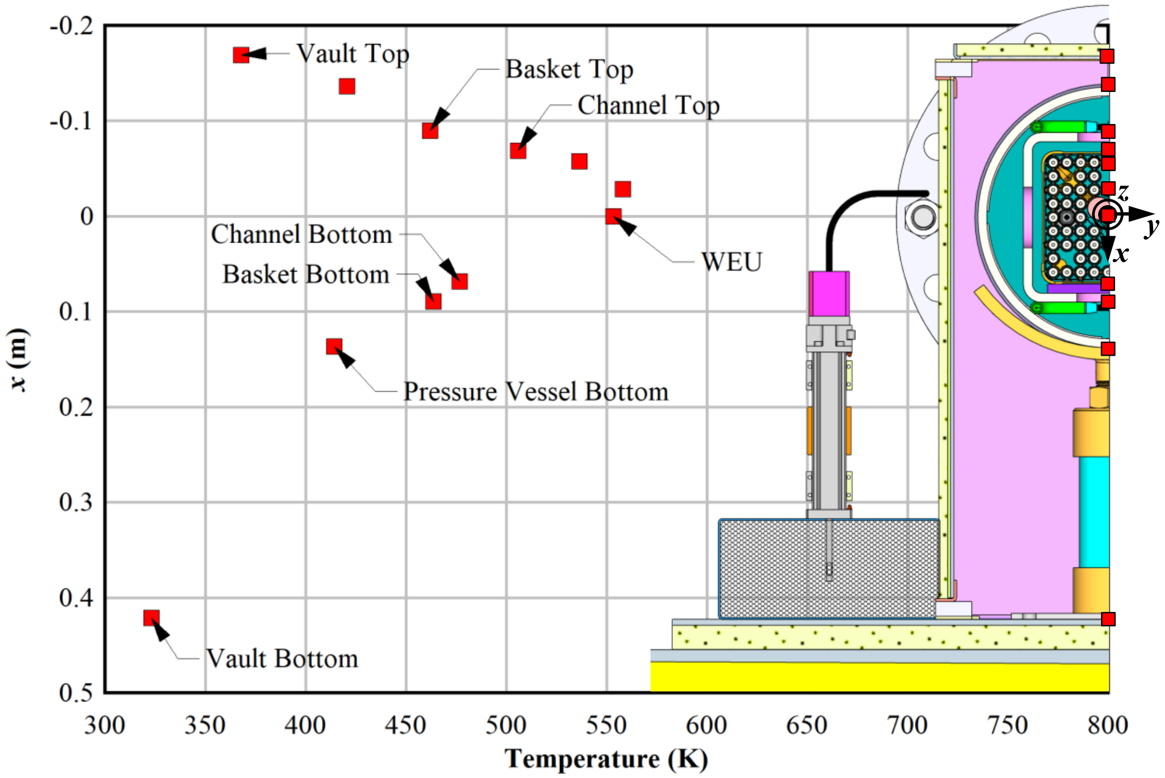

Figure 3.3 Vertical temperature profile for 2.50 kW, z = 1.219 m (48.0 in.), and helium at 100 kPa.

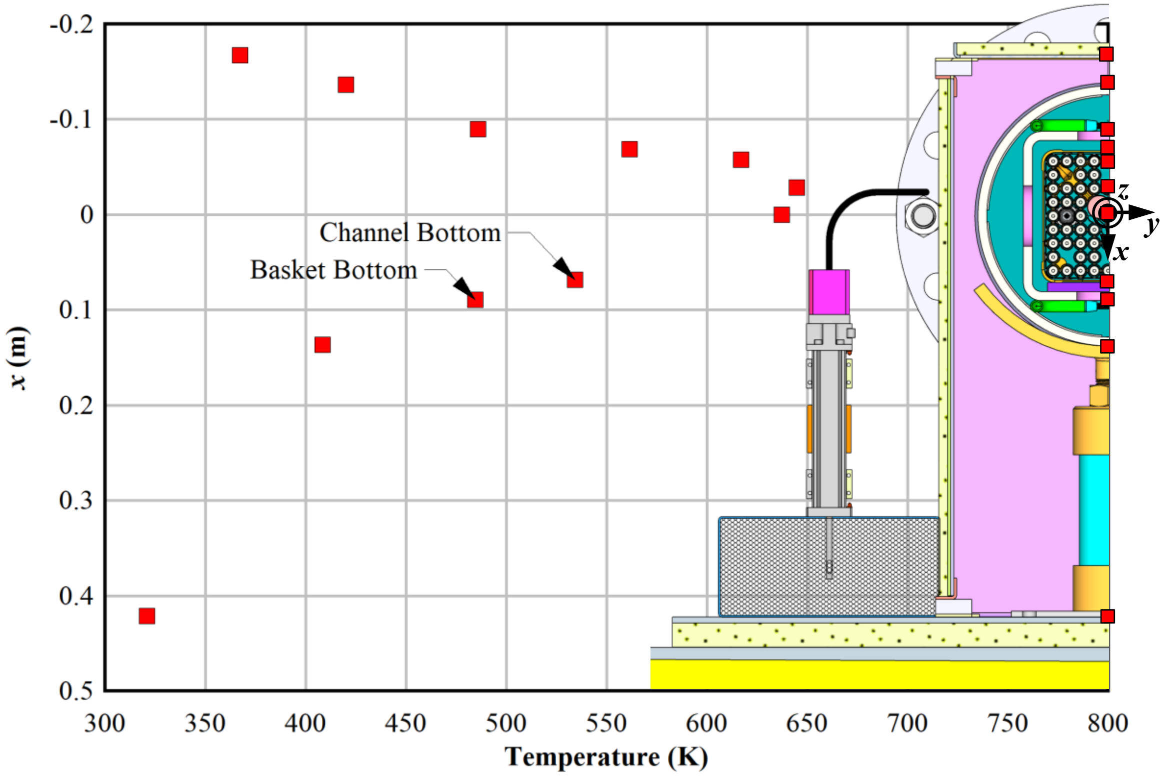

Figure 3.4 Vertical temperature profile for 2.50 kW, z = 1.219 m (48.0 in.), and air at 100 kPa.

3.2.3 Horizontal Temperature Profile – T*(y)*

The steady-state horizontal temperature data for the 2.50 kW, 100 kPa fill of helium and air are presented in Table 3.5 and shown in Figure 3.5 and Figure 3.6, respectively. The unscaled inset figure in the bottom left shows the location of the thermocouples. The profile passes through the center line of the apparatus along the y-axis at $z = 1.829$ m. The profile starts in the center of the assembly and proceeds out through Quadrant 3 in the positive y-direction. The TCs shown in the plot are located on a water rod near the center of the fuel assembly, heater rods GU and IU (see Figure 2.9 for heater rod naming convention), channel box, basket, pressure vessel, and vault wall. The peak temperature for both cases was located on rod GU but the peak temperature for the helium fill case was 84 K cooler than the air fill case. As was the case in the vertical temperature profile, the temperature gradients between the components inside the pressure vessel are lower in the helium case than in the air case.

Table 3.5 Horizontal temperature profile coordinates for 2.50 kW, $z = 1.829$ m (72.0 in.), and at 100 kPa for the helium and air test cases.

Location	y (in.)	y (m)	Temperature (K)	
			Helium	Air
WEU	0.00	0.000	548	630
GU	1.13	0.029	550	634
IU	2.26	0.057	532	607
Channel	2.70	0.068	499	552
Basket	3.51	0.089	459	481
Pressure Vessel	5.38	0.137	416	414
Vault	6.50	0.165	334	333

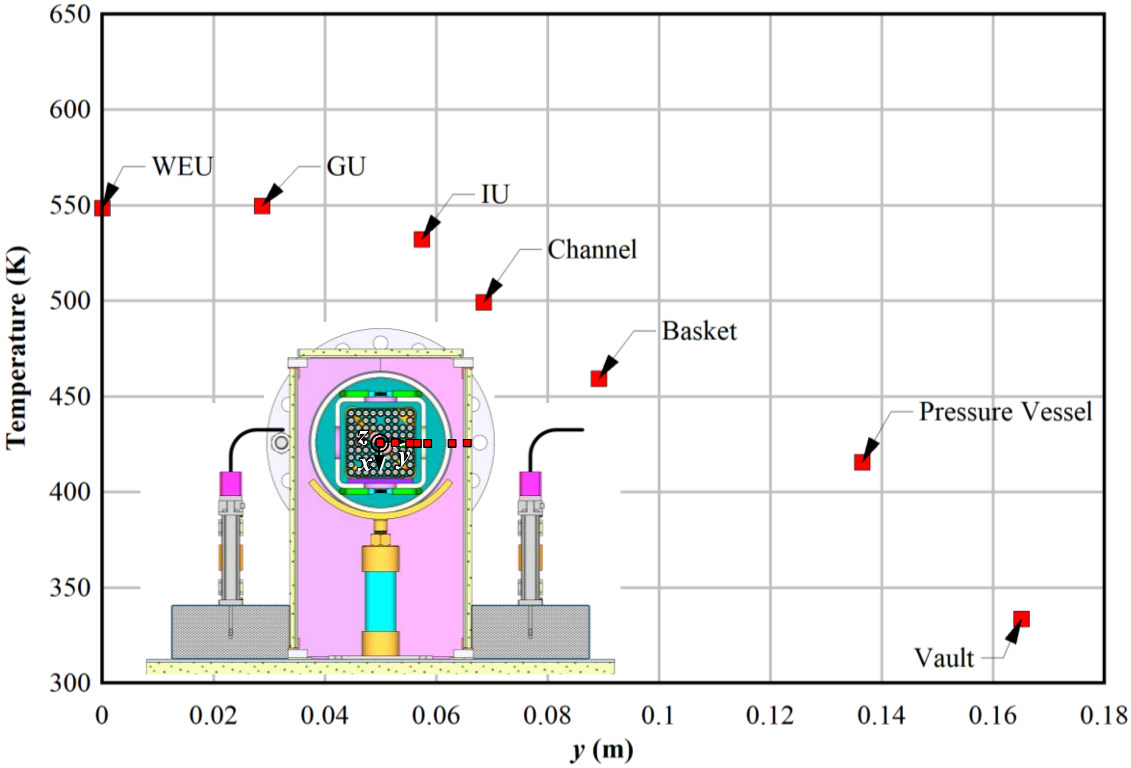

Figure 3.5 **Horizontal temperature profile for 2.50 kW, z = 1.829 m (72.0 in.), and helium at 100 kPa.**

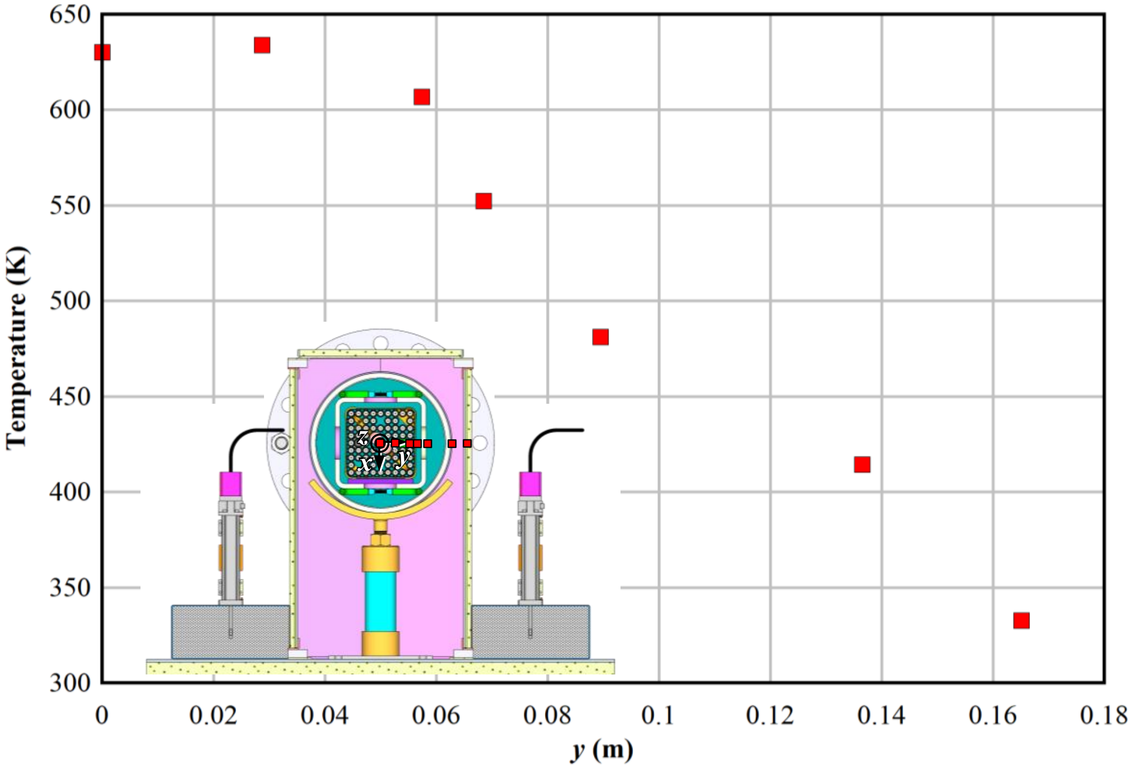

Figure 3.6 **Horizontal temperature profile for 2.50 kW, z = 1.829 m (72.0 in.), and air at 100 kPa.**

4 SUMMARY

The purpose of the present investigation is to produce data sets that can be used to benchmark the codes and best practices presently used to determine cladding temperatures and induced cooling air flows in modern horizontal dry storage systems. The horizontal dry cask simulator (HDCS) has been designed to generate this benchmark data and add to the existing knowledge base. The pressure vessel representing the canister has been designed, fabricated, and pressure tested for a maximum allowable working pressure (MAWP) rating of 2,400 kPa at 400 °C. An existing electrically heated but otherwise prototypic boiling water reactor (BWR), Incoloy-clad test assembly has been deployed inside of a representative storage basket and canister. An insulated sheet metal enclosure is used to mimic the thermal properties of the concrete vault enclosure used in a modern horizontal storage system. Transverse and axial temperature profiles along with induced cooling air flow are measured for a wide range of decay powers and representative (and higher) canister pressures using backfills of helium or air.

The single assembly geometry with well-controlled boundary conditions simplifies computational requirements while preserving relevant physics. The test apparatus integrates all the underlying thermal-hydraulics important to defining the performance of a modern horizontal storage system. These include combined-mode heat transfer from the electrically-heated assembly to the canister walls and the primarily natural-convective heat transfer from the canister to the cooling air flow passing through the horizontal vault enclosure. The objective of the HDCS investigation is to capture the dominant physics of a commercial dry storage system in a well-characterized test apparatus for any given set of operational parameters. The close coupling between the thermal response of the canister system and the resulting induced cooling air flow rate is of particular importance.

In a previous investigation, data sets from a vertically oriented dry cask simulator (DCS) were used in a model validation activity. However, this model validation activity was not fully blind in that all the modeling participants had access to complete data sets. Data from the present investigation using the HDCS will be used to host a blind model validation effort. Although a complete set of data has been collected with the HCDS spanning fill pressures of both helium and air from 100 kPa to 800 kPa and assembly powers from 0.5 kW to 5 kW, only the data from two test cases are presented in this report. These two cases are for a test assembly power of 2.50 kW and a backfill pressure of 100 kPa with helium for one case and air for the other case. Providing this limited data set will facilitate model comparisons and refinement while reserving the remaining data for a blind validation study in the near future.

The steady-state peak temperatures for the components located inside the pressure vessel were significantly lower for the helium fill case than the air fill case. The PCT for the helium case was 559 K and located at z = 1.22 m. The PCT for the air fill case was 647 K and located at 0.61 m. The vertical and horizontal temperature profiles both indicate that the temperature gradients between the components inside the pressure vessel are lower in the helium case than in the air case.

This page is intentionally left blank.

REFERENCES

American National Standards Institute, “American National Standard for Radioactive Materials – Leakage Tests on Packages for Shipment,” ANSI N14.5-2014, New York, NY, June 2014.

American Society of Mechanical Engineers, “ASME Performance Test Code 19.1.2013 – Test Uncertainty,” New York, NY, May 2014.

ASTM International, “Standard Specification for Temperature-Electromotive Force (emf) Tables for Standardized Thermocouples,” E230/E230M-17, West Conshohocken, PA, November 2017.

Bates, J.M., “Single PWR Spent Fuel Assembly Heat Transfer Data for Computer Code Evaluations,” PNL-5571, Pacific Northwest Laboratory, Richland, WA, January 1986.

Creer, J.M., T.E. Michener, M.A. McKinnon, J.E. Tanner, E.R. Gilbert, R.L. Goodman, “The TN-24P PWR Spent Fuel Storage Cask: Testing and Analyses”, EPRI NP-5128 Proj. 2406-4, PNL-6054, Electric Power Research Institute, Palo Alto, CA, April 1987.

Dziadosz, D., E.V. Moore, J.M. Creer, R.A. McCann, M.A. McKinnon, J.E. Tanner, E.R. Gilbert, R.L. Goodman, D.H. Schoonen, M Jensen, and C. Mullen, “The Castor-V/21 PWR Spent-Fuel Storage Cask: Testing and Analyses,” EPRI NP-4887, Project 2406-4, PNL-5917, UC-85, Electric Power Research Institute, Palo Alto, CA, November 1986.

Durbin, S.G. and E.R. Lindgren, “Thermal-Hydraulic Results for the Boiling Water Reactor Dry Cask Simulator,” SAND2017-10551R, Sandia National Laboratories, Albuquerque, NM, September 29, 2017.

Durbin, S.G. and E.R. Lindgren, “Thermal-Hydraulic Experiments Using a Dry Cask Simulator,” NUREG/CR-7250, Nuclear Regulatory Commission, Washington, D.C., October 2018.

Electric Power Research Institute, “High Burnup Dry Storage Cask Research and Development Project: Final Test Plan,” Contract No.: DE-NE-0000593, February 2014.

Irino, M., M. Oohashi, T. Irie, and T. Nishikawa, “Study on Surface Temperatures of Fuel Pins in Spent Fuel Dry Shipping/Storage Casks,” IAEA-SM-286/139P, Proceedings of Packaging and Transportation of Radioactive Materials (PATRAM ’86), Volume 2, p. 585, International Atomic Energy Agency, Vienna, Austria, 1987.

Lindgren, E.R. and S.G. Durbin, “Characterization of Thermal-Hydraulic and Ignition Phenomena in Prototypic, Full-Length Boiling Water Reactor Spent Fuel Pool Assemblies after a Complete Loss-of-Coolant Accident”, NUREG/CR-7143, SAND2007-2270, Nuclear Regulatory Commission, Washington, D.C., March 2013.

Lindgren, E.R. and S.G. Durbin, “Materials and Dimensional Reference Handbook for the Boiling Water Reactor Dry Cask Simulator,” SAND2017-13058R, Sandia National Laboratories, Albuquerque, NM, November 2017

Lindgren, E. R., Salazar, A., and Durbin, S. G, “Component Concepts for Advanced Dry Storage Investigations,” SAND2019-3587 R, Sandia National Laboratories, Albuquerque, NM, March 2019.

McKinnon, M.A., J.W. Doman, J.E. Tanner, R.J. Guenther, J.M. Creer and C.E. King, “BWR Spent Fuel Storage Cask Performance Test, Volume 1, Cask Handling Experience and Decay Heat, Heat Transfer, and Shielding Data,” PNL-5777 Vol. 1, Pacific Northwest Laboratory, Richland, WA, February 1986.

McKinnon, M.A., Dodge, R.E., Schmitt, R.C., L.E. Eslinger, and G. Dineen, “Performance Testing and Analyses of the VSC-17 Ventilated Concrete Cask,” EPRI-TR-100305, Electric Power Research Institute, Palo Alto, CA, May 1992.

McKinnon, M.A., T.E. Michener, M.F. Jensen, G.R. Rodman, “Testing and Analyses of the TN-24P Spent Fuel Dry Storage Cask Loaded with Consolidated Fuel,” EPRI NP-6191 Proj. 2813-16, PNL-6631, February 1989.

McKinnon, M.A., J.M. Creer, C. L. Wheeler, J.E. Tanner, E.R. Gilbert, R.L. Goodman, D.P. Batala, D.A. Dziadosz, E.V. Moore, D.H. Schoonen, M.F. Jensen, and J.H. Browder, “The MC-10 PWR Spent Fuel Storage Cask: Testing and Analysis,” EPRI NP-5268, Electric Power Research Institute, Palo Alto, CA, July 1987.

Misumi, T., Suzuki, K., and Kitamura, K., “Fluid Flow and Heat Transfer of Natural Convection Around Large Horizontal Cylinders: Experiments with Air,” Heat Trans. – Asian Res., 32 (4), 293-305, 2003.

Noack, B.R., “On the Flow Around a Circular Cylinder. Part II: Turbulent Regime,”, ZAMM-Z. Angew. Math. Me., 79, S227-S230, 1999.

Pulido, R.J.M., E.R. Lindgren, S.G. Durbin, A. Zigh, J. Solis, S.R. Suffield, D.J. Richmond, J.A. Fort, L.E. Herranz, F. Feria, J. Penalva, M. LLoret, M. Galbán, J. Benavides, and G. Jiménez, "Modeling Validation Exercises Using the Dry Cask Simulator," SAND2019-6079R, Sandia National Laboratories, Albuquerque, NM, May 2019.

Solis, J. and Zigh, A., “Impact of Variation in Environmental Conditions on the Thermal Performance of Dry Storage Casks,” NUREG-2174, Nuclear Regulatory Commission, Washington, D.C., February 2015.

Sparrow, E.M. and Pfeil, D.R., “Enhancement of Natural Convection Heat Transfer from a Horizontal Cylinder Due to Vertical Shrouding Surfaces,” J. Heat Trans., 106, 124-130, February 1984.

Strope, L.A., M.A. McKinnon, D.J. Dyksterhouse, and J.C. McLean, “NUHOMS Modular Spent-Fuel Storage System: Performance Testing,” EPRI NP-6941, PNL-7327, Electric Power Research Institute, Palo Alto, CA, September 1990.

Suffield, S.R., J.A. Fort, H.E. Adkins, J.M. Cuta, B.A. Collins, and E.R. Siciliano, “Thermal Modeling of NUHOMS HSM-15 and HSM-1 Storage Modules at Calvert Cliffs Nuclear Power Station ISFSI,” PNNL-21788, Pacific Northwest National Laboratory, Richland, WA, October 2012.

Surface Optics Corporation, “ET 100 Reflectometer User's Guide (1.5 to 21 microns, Model 0410-0030 Command Module, Model 0410-0038 Measurement Head),” Version NCA, San Diego, CA, March 2017

Yamamoto, A., Ikehara, T., and Ito, T. “Benchmark Problem Suite for Reactor Physics Study of LWR Next Generation Fuels,” J. Nucl. Sci. Tech., 39 (8), 900-912, 2002.

APPENDIX A ERROR PROPAGATION ANALYSIS

The error and uncertainty inherent to an experimental result are critical to the accurate interpretation of the data. Therefore, the uncertainties in the experimental measurements are estimated in this section. Results of this analysis are given, followed by a general description of the method used and a brief explanation of the source of each reported measurement uncertainty.

The overall standard uncertainty of an indirect measurement y, dependent on N indirect measurements x_i, is defined in Equation A.1. The standard uncertainty associated with an indirect measurement is analogous to the standard deviation of a statistical population.

$$u^2 = \sum_{i=1}^{N} \left(\frac{\partial y}{\partial x_i} u_i \right)^2 \qquad \text{A.1}$$

Here, u is used to define the standard uncertainty of a measurement.

The expanded uncertainty, U, is reported in this appendix and defines the bounds that include 95% of the possible data. The expanded uncertainty is assumed to be defined as the product of the standard uncertainty and the Student's t-value. Unless otherwise stated, all uncertainty measurements are assumed to be based on a Student's t-distribution with no fewer than 30 measurements. The associated t-value for 95% confidence intervals is 2.0 for 29 degrees of freedom. Therefore, Equation A.2 shows the definition of the expanded uncertainty as used in the following sections for a 95% confidence interval.

$$U = t_{\text{value}} \cdot u \qquad \text{A.2}$$

A.1 Temperature Measurements

A.1.1 Uncertainty in Clad Temperature Measurement

Clad temperature was measured with a standard k-type TC using the standard ASTM calibration specifications [ASTM, 2017]. No additional calibrations were performed. While uncertainties of up to 2 to 5% are justified for surface-mounted thermocouples in high heat flux and/or highly transient environments, the relatively small spatial and temporal gradients experienced during the HDCS testing warrant an expanded uncertainty for this type of TC of U_T = 1% of the reading in Kelvin [Nakos, 2004]. The maximum peak clad temperature reading was 647 K for the 2.50 kW 100 kPa air test. The maximum expanded uncertainty for the cladding temperature is $U_{PCT} = \pm 6.5$ K.

A.1.2 Uncertainty in Ambient Air Temperature

The air temperature was measured with a standard k-type TC. The expanded uncertainty for this type of TC is U_T = 1% of the reading in Kelvin [Nakos, 2004]. The maximum ambient temperature reading was 302 K for the 2.50 kW 100 kPa helium test. The maximum expanded uncertainty for the ambient temperature is $U_{T\text{-amb}} = \pm 3.0$ K.

A.2 Pressure Measurements

A.2.1 Uncertainty in Ambient Air Pressure

The air pressure was measured with an Omega pressure sensor (Model PX2760-600A5V, S/N 6857389). The uncertainty of the ambient air pressure was taken from the manufacturer's calibration sheet, which indicated an expanded uncertainty in the instrument of ±0.25% of full scale (110 kPa). Therefore, the expanded uncertainty in the pressure reading is $U_{P\text{-atm}} = \pm 0.275$ kPa.

A.2.2 Uncertainty in Vessel Pressure

The interior vessel pressure was measured as the average output of two high-accuracy 0 to 1,034 kPa (0 to 150 psia) absolute pressure transducers (Setra Systems ASM1-150P-A-1M-2C-03-A-01) installed in the instrument well. The experimental uncertainty associated with a single gage is ±0.05% of full scale, or $U_{\mathrm{PV},1} = \pm 0.52$ kPa (±0.075 psi). The combined uncertainty of the average of the two transducers is $U_{\mathrm{PV, AVG}} = \pm 0.37$ kPa (±0.053 psia). Note that the pressure was controlled to within ±0.35 kPa (±0.051 psia) as measured by taking half of the difference between the overall maximum and minimum internal average pressure observed during testing.

A.3 Uncertainty in Electrical Measurements

The voltage, current, and power supplied to the internal spent fuel assembly heater rods were measured by an Ohio Semitronics, Inc. Multifunction Power Test Board (Model PTB-112D1PCY48, SN 18100713). The stated manufacturer's uncertainty was given as ±0.25% of full scale for each measurement. The full scales for each measurement are Voltage = 150 V, Amps = 100 A, Power Factor = 1.00, and Power = 12.00 kW. However, a special calibration schedule of thirty-two points was ordered for this instrument. The expanded uncertainty based on the *t*-statistic ($t_{31} = 2.0$) and the standard error of the regression for each measurement variable was $U_{\mathrm{Volt}} = \pm 0.11$ V, $U_{\mathrm{Amp}} = \pm 0.07$ A, $U_{\mathrm{PF}} = \pm 0.036$, $U_{\mathrm{Watt}} = \pm 13$ W. These instrument-specific uncertainties represent considerably better accuracy than the generic manufacturer's certification.

A.4 Flow Measurements

The methodology for determining the induced air flow is described in detail in Section 2.5.2. Air velocity profiles were recorded across the inlet ducts. These velocities were then used to derive the two-dimensional flow field in the ducts. This flow field was then integrated to determine the air mass flow rate.

The uncertainty in the air mass flow rate per duct was calculated to be $U_{\dot{m},\,\mathrm{per\ duct}} = \pm 1.5 \times 10^{-4}$ kg/s. The combined error in the total air mass flow rate across all four ducts is $U_{\dot{m},\,\mathrm{Total}} = \pm 3.0 \times 10^{-4}$ kg/s. Note that 90% of this error is associated with uncertainties in the differential areas and integration scheme. The remaining error is due to uncertainty in the hot wire anemometers. Finally, the observed fluctuations in the air mass flow rate per duct, given by $(\dot{m}_{\mathrm{max}} - \dot{m}_{\mathrm{min}})/2 = 1.7 \times 10^{-4}$ kg/s, was roughly in agreement with the estimated uncertainty.

A.4.1 Uncertainty in Hot Wire Anemometer Measurements

The TSI Model 8455 hot wire anemometer has a manufacturer's expanded uncertainty of ±2% of reading +0.5% of full scale. The chosen full scale for all tests was 1 m/s. Therefore, the maximum expanded uncertainty was defined as $U_v = \pm 0.025$ m/s for the ambient temperatures encountered. Standard conditions for the TSI hotwire are 21.1 °C and 101.4 kPa.

For velocities near the wall, an alternative approach was adopted to estimate uncertainty. The difference in the velocity central to the differential area and the average of the estimated velocities along the periphery of the differential area was taken to estimate the maximum uncertainty. The average of this alternative uncertainties along the perimeter of the inlet gives an expanded uncertainty of $U_{v,\,\nabla v} = \pm 0.033$ m/s for these edge velocities.

A.4.2 Uncertainty in Differential Areas

The positional accuracy of each motorized stage (Velmex Xslide) based on straight line accuracy is given by the manufacturer as $U_{\mathrm{stage}} = \pm 0.08$ mm. However, this estimate does not include other sources of uncertainty such as slight errors in stage alignment and deviations in the duct itself. An uncertainty for each dimension of the differential area of $U_{\Delta x} = U_{\Delta y} = \pm 1.6$ mm was chosen to incorporate all known and unknown uncertainties in the differential area.

Table A.1 gives the uncertainty of the average differential area $U_{\Delta A,AVG} = \pm 2.3\times10^{-5}$ m^2.

Table A.1 Representative calculation to estimate the expanded error of flow area determination.

Measurement, x_i	Units	Value	Expanded uncertainty, U_i	Influence coefficient ($U_i \cdot [(\partial\Delta A/\partial x_i)/\Delta A]$)	Contribution
Δx_{AVG}	m	6.4E-03	1.6E-03	2.5E-01	0.81
Δy_{AVG}	m	1.3E-02	1.6E-03	1.2E-01	0.19
ΔA_{AVG}	m^2	8.3E-05	2.3E-05	2.8E-01	1.00

This page is intentionally left blank.

APPENDIX B DRAWINGS

B.1 Internal Components

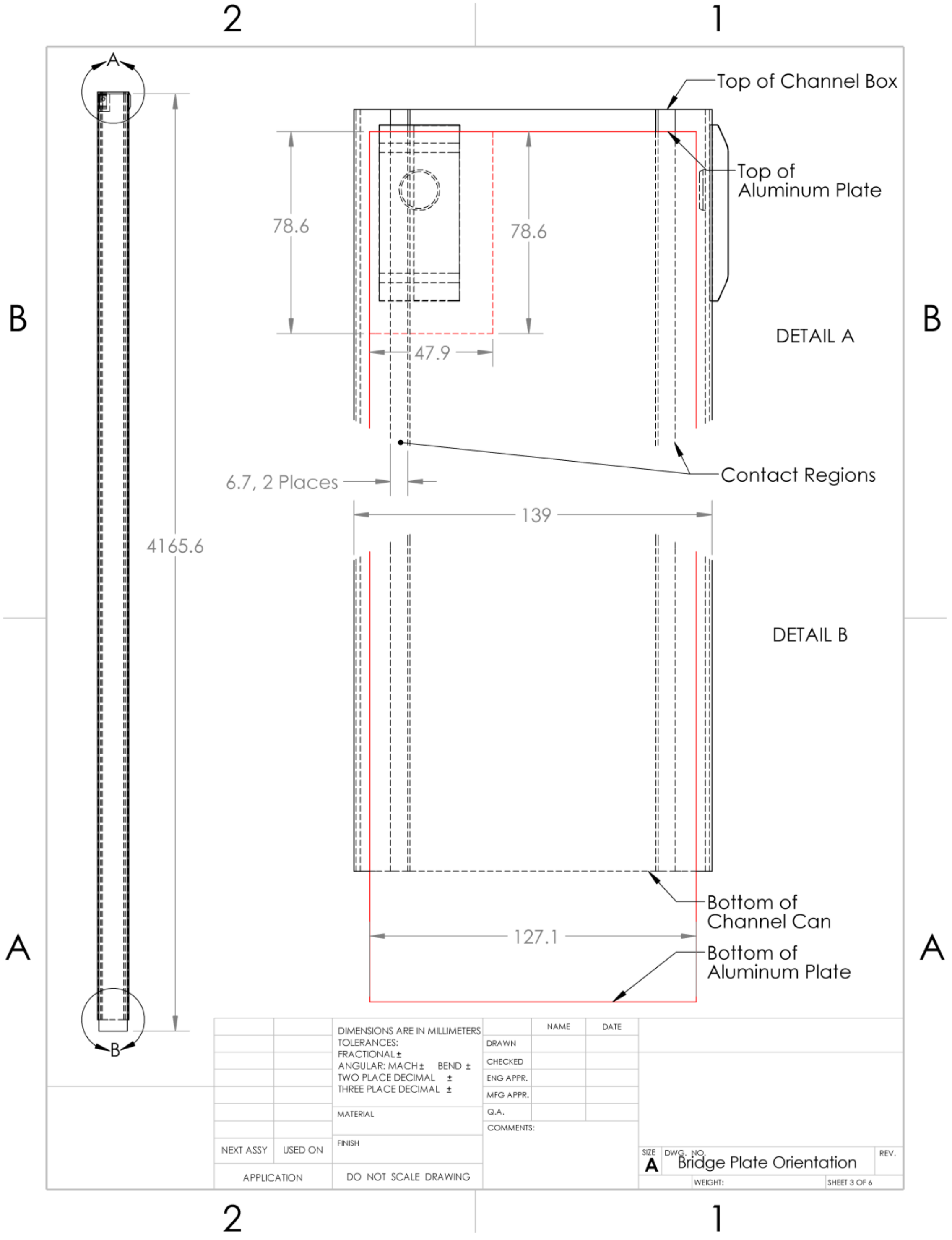

Figure B.1 Aluminum bridge plate orientation with respect to the channel box.

The aluminum bridge plate is shown in red.

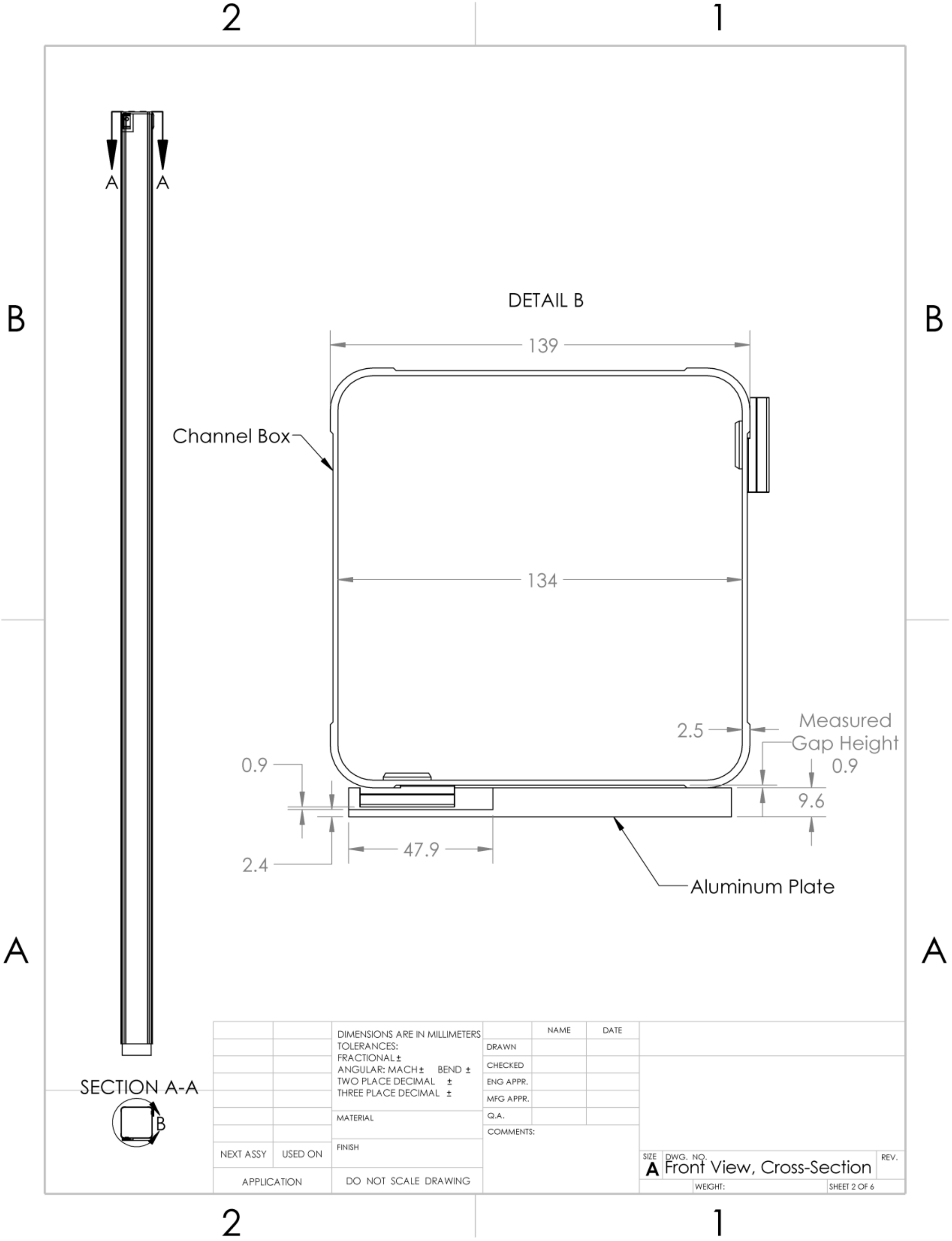

Figure B.2 Top cross-section front view of the channel box and the aluminum bridge plate.

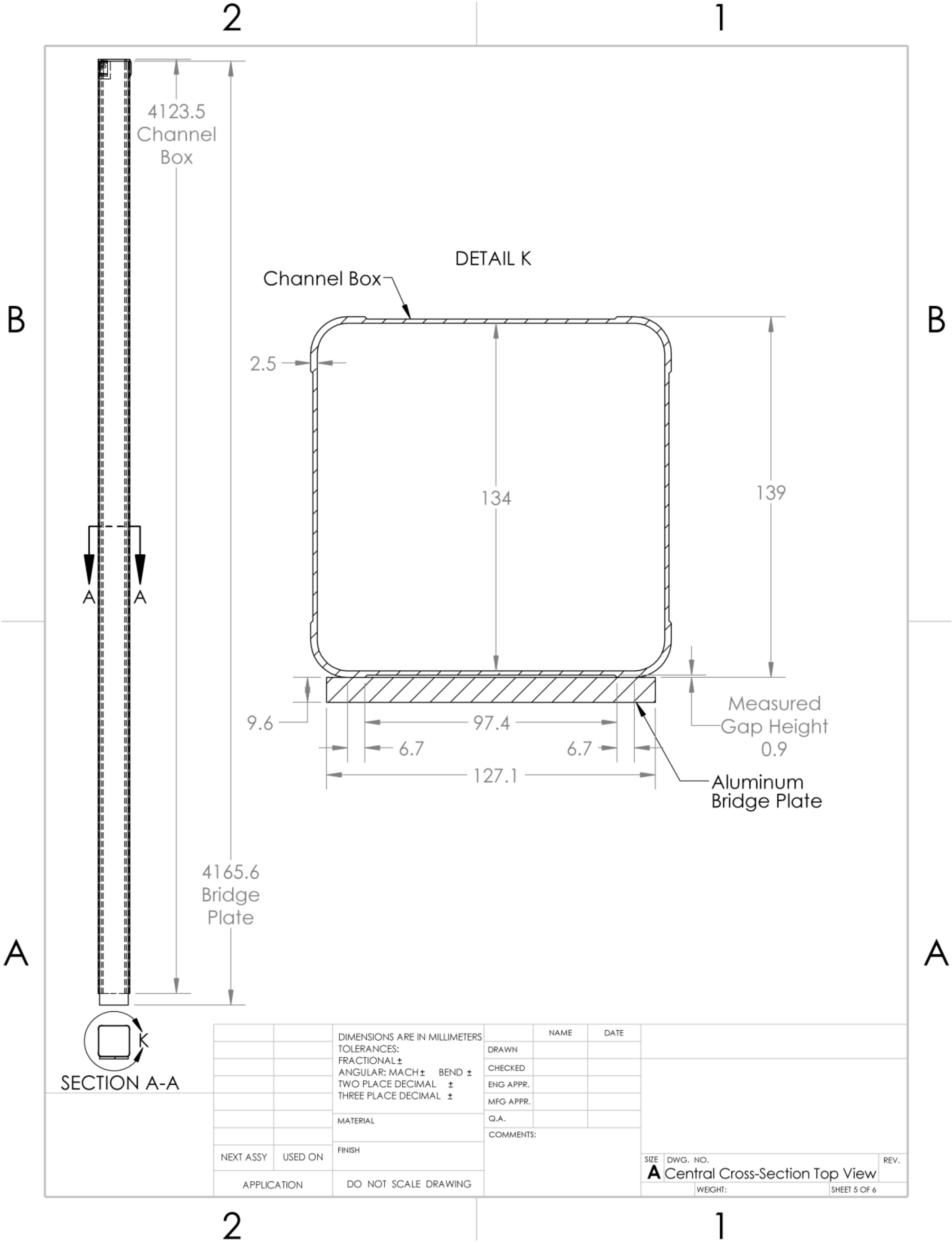

Figure B.3 Central cross-section front view of the channel box and the aluminum bridge plate.

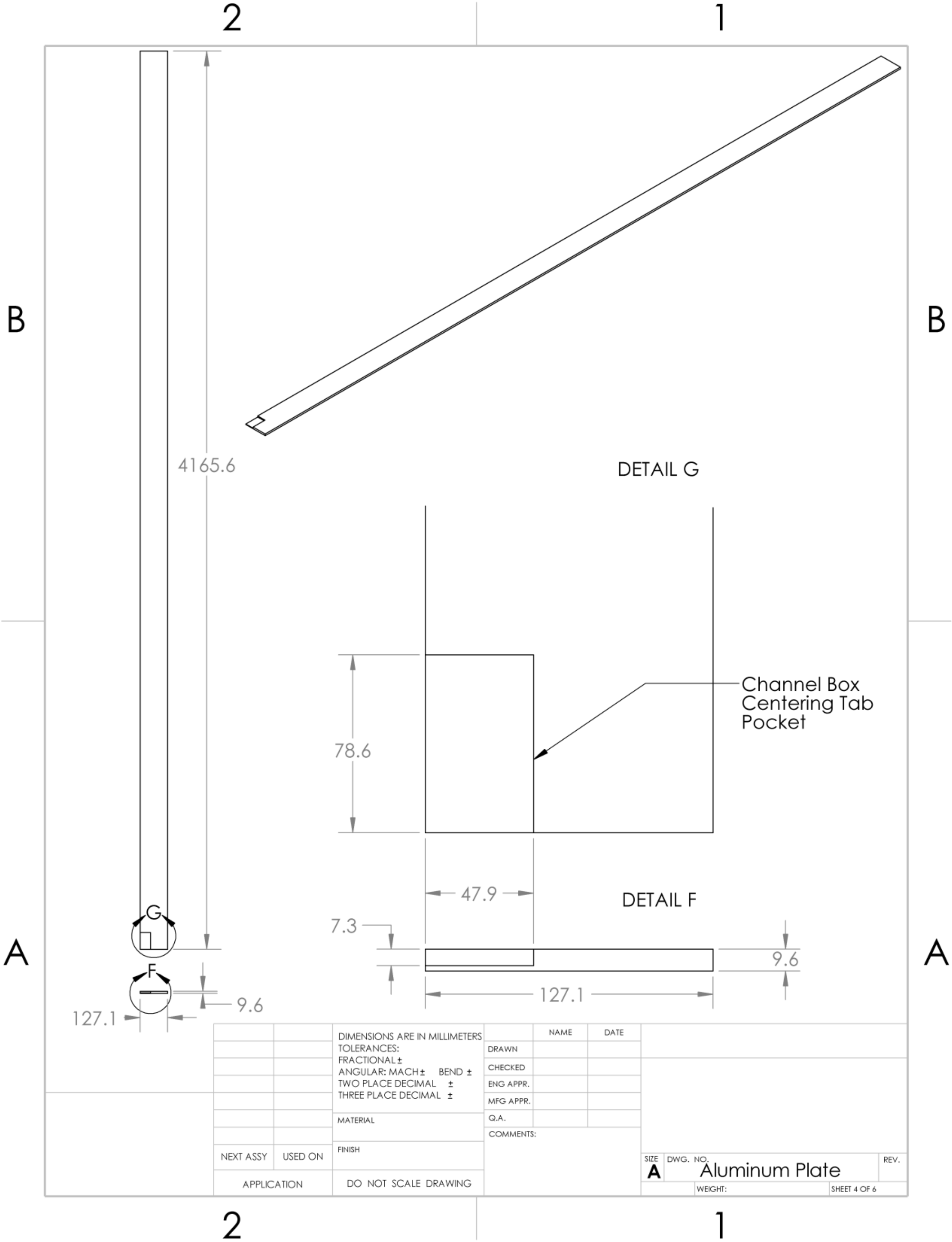

Figure B.4 Aluminum bridge plate dimensions.

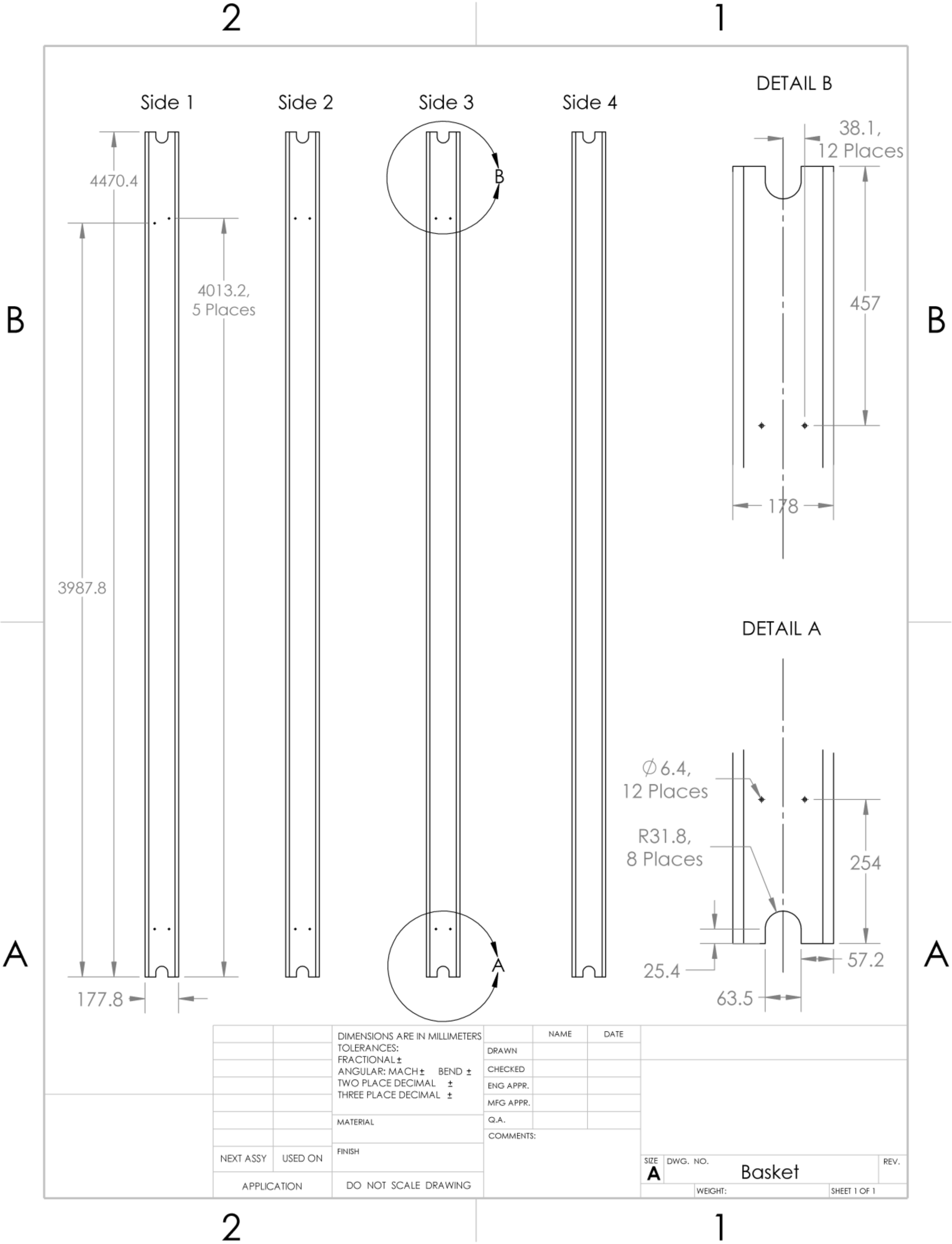

Figure B.5 Basket dimensions.

B.2 Vault

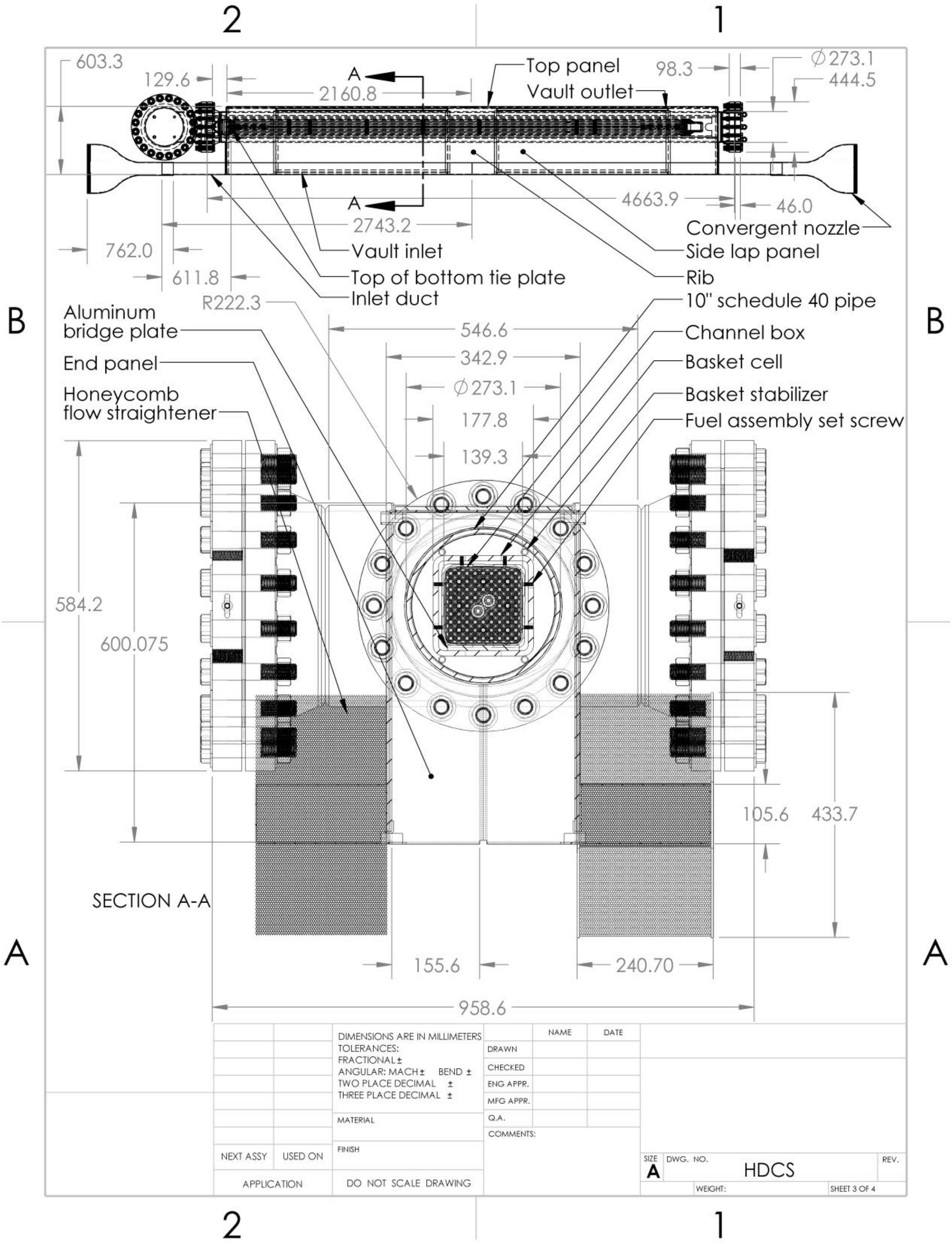

Figure B.7 Transversal view of horizontal dry cask simulator.

B.3 Flow Straightener

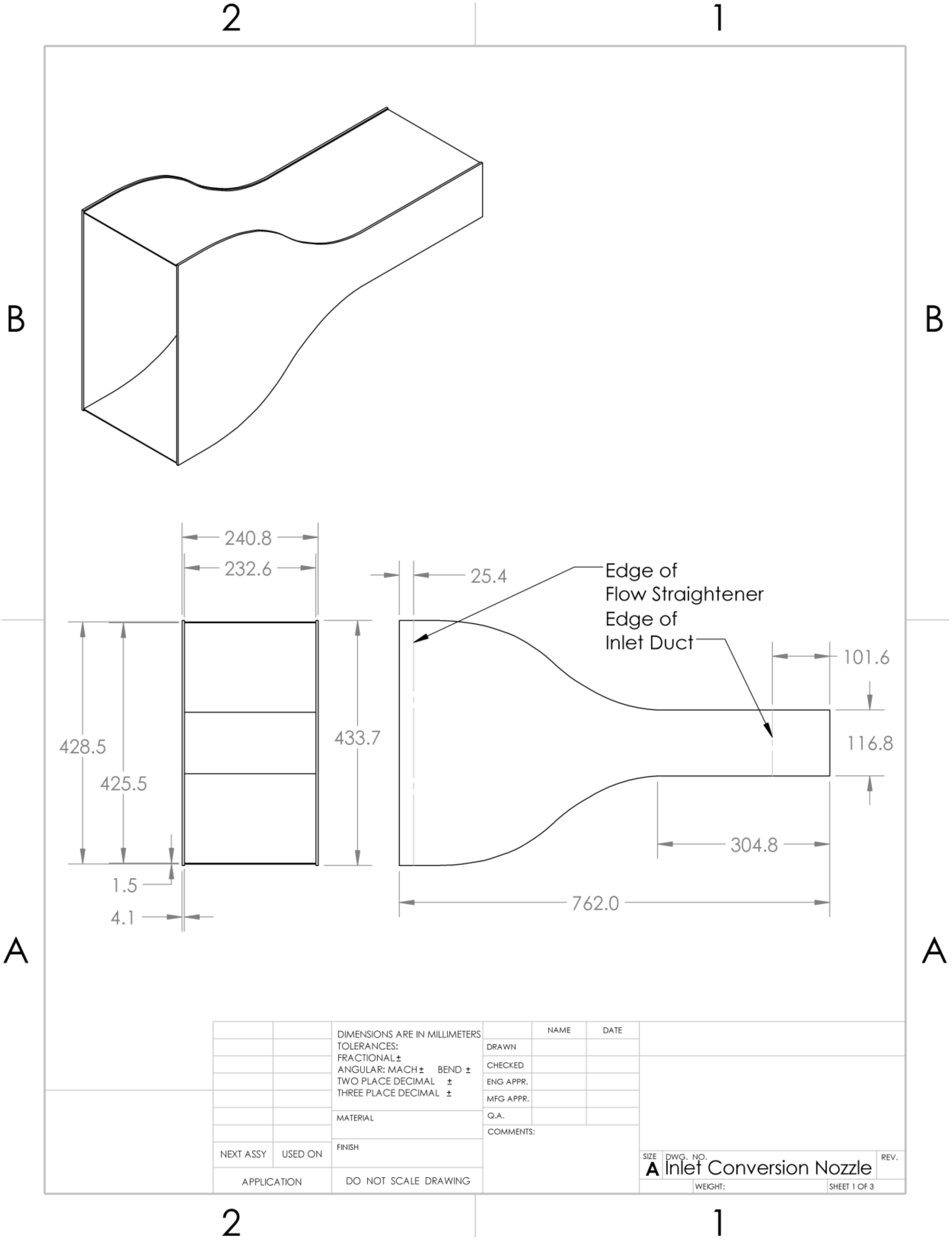

Figure B.8 Inlet conversion nozzle.

This page is intentionally left blank.

APPENDIX C EMISSIVITY OF HDCS VAULT

Emissivity measurements of the Horizontal Dry Cask Simulator (HDCS) vault were carried out to gain information on the radiative thermal conductivity of the Dry Cask Simulator (DCS) system. An ET 100 reflectometer was used to measure the thermal emissivity of the HDCS vault. This vault is a newly constructed structure external to the DCS pressure vessel that is representative of the ventilation systems used in commercial horizontal dry cask storage. This appendix captures the extensive work done to experimentally determine the emissivity profile of this structure – the work here follows the same procedure as the one outlined for the DCS structures in Appendix A of the HDCS test plan [Lindgren et al., 2019].

C.1 Measurement Uncertainties

C.1.1 Spatial Uncertainty

Each emissivity data point is the result of the average of 6 individual measurements on the same spot of the sample. Two axial levels (one at each end of the vault) of each structure were chosen as locations to obtain 30 measurements. This was done in order to obtain a sufficiently large number of degrees of freedom to give 95% confidence that the true population mean is within 2 standard deviations of the measured population mean, as defined by ASME Performance Test Code 19.1 [ASME, 2014]. Measurement obstructions such as gaps between vault components and the platforms used to elevate the DCS fuel assembly and structures introduced nonuniform spacing between the chosen axial levels of the measurements. Nonetheless, the goal was to obtain approximately 12 inches of spacing between each axial level where emissivity measurements were done to match as closely with the thermocouple locations as possible. Each spot where measurements were taken was measured using digital calipers to maintain consistency. The measurement locations were marked using a scribe and a 2.25 in diameter aluminum circular disc for tracing. Measurements were taken inside of these traced circles, and the diameter of the ET 100 reflectometer measurement surface was 1 in., so the spatial measurement uncertainty was assumed to be ±0.625 in.

C.1.2 Reflectometer Measurement Uncertainty

The reflectometer measurement uncertainty for the hemispherical thermal emittance was provided by Surface Optics Corporation. The ET 100 manual reports a reflectance accuracy of ±0.03 at 20 degrees; (Surface Optics Corporation, 2017) contact with a technical representative from Surface Optics Corporation revealed a reflectance accuracy of ±0.03 at 60 degrees and a total hemispherical emissivity accuracy of ±0.05. This error is intrinsic to the instrument and represents the dominant factor in measurement uncertainty.

C.2 HDCS Vault Emissivities

The HDCS vault emissivity profiles along its four interior sides were analyzed using an ET 100 reflectometer to determine their thermal emissivity. The device was first calibrated using a gold calibration coupon and then used to measure the emissivity (formally defined as the hemispherical thermal emissivity or HTE) of each interior side of the HDCS vault at approximately 12-inch axial intervals. Any deviation from the 12-inch spacing between measurement locations was made because of physical obstructions on the measuring surface. The axial zero reference point was defined at the top of the bottom tie plate of the channel box; this point was marked using a digital caliper in order to define the same zero reference point for every side of the vault. The locations of the emissivity measurements are shown in Figure C.1 and Figure C.2. These locations were chosen to be along the first and third quarter-points of each side, where the first quarter-point is defined as the top quarter and the third quarter-point is defined as the bottom quarter of each interior side with respect to an observer facing “north” towards the

HDCS, as defined by Figure C.1. The emissivity at each axial level was taken to be the average of the two values measured at that axial level for each side.

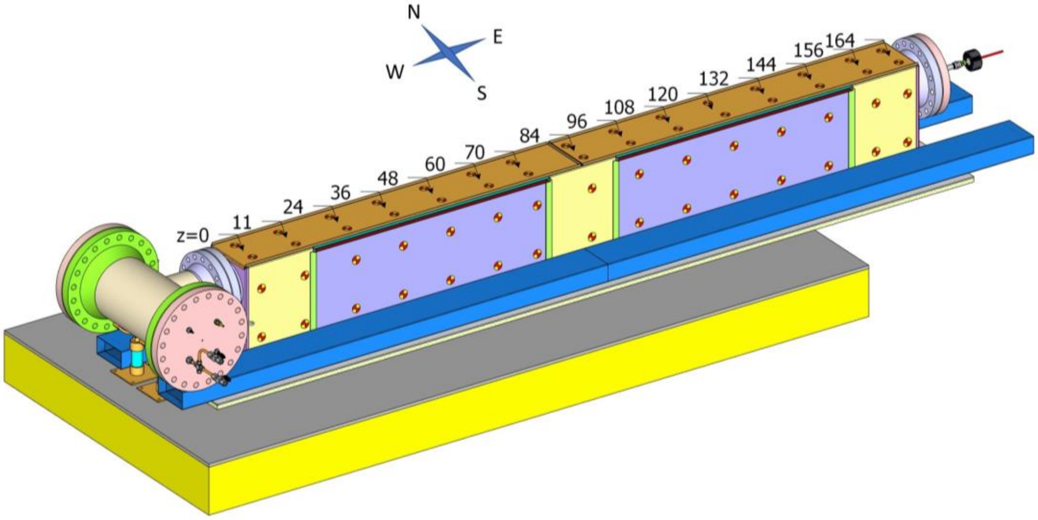

Figure C.1 **Emissivity measurement locations along the top and side interior surfaces of the vault, indicated by the yellow/red circles.**

The measurement locations for the south side of the vault are in line with those on the north side.

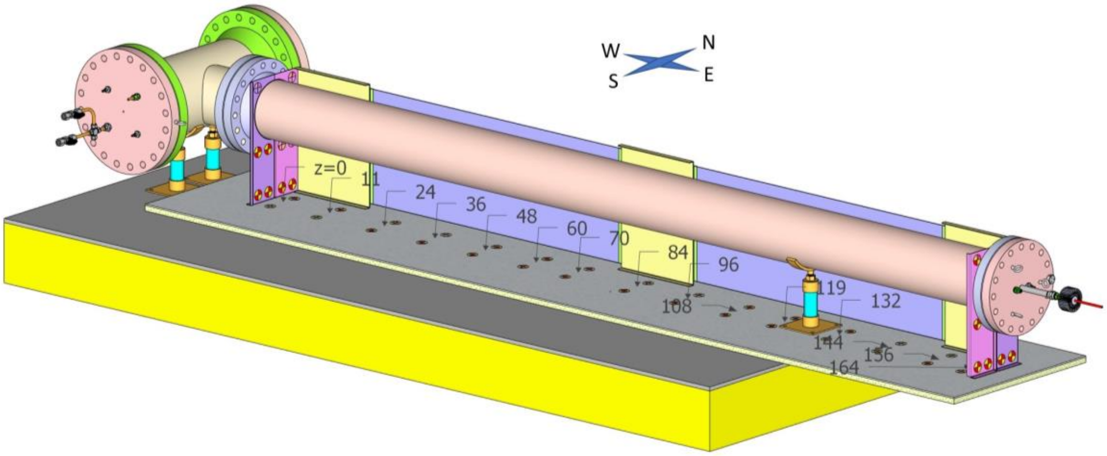

Figure C.2 **Emissivity measurement locations along the bottom interior surface and the two ends of the vault, indicated by the yellow/red circles.**

The results for the emissivity profiles for the four interior sides of the vault are shown in Figure C.3. The HDCS had yet to be tested when the emissivity measurements were taken, so no oxidation that would be generated from testing conditions was present on any surface. In addition, the vault was constructed entirely out of 316 stainless steel. Thus, the emissivities were expected to be constant across the vault's axial length.

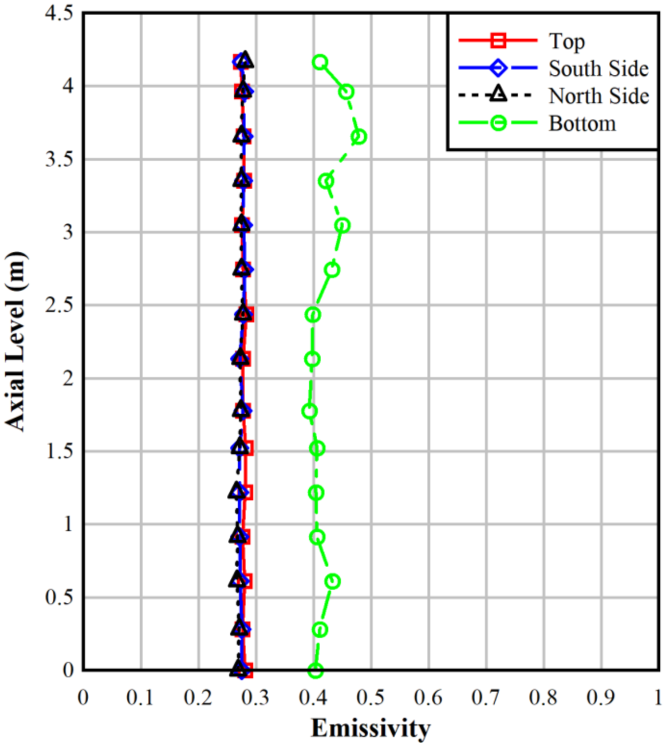

Figure C.3 Measured HDCS vault thermal emissivity values from all four interior sides at room temperature.

The locations for the emissivity measurements taken at the ends of the vault are shown in Figure C.4. The mapping scheme shown in this figure corresponds to the emissivity values shown in Table C.1 and Table C.2 for the ends of the vault at the top and bottom of the HDCS assembly, respectively.

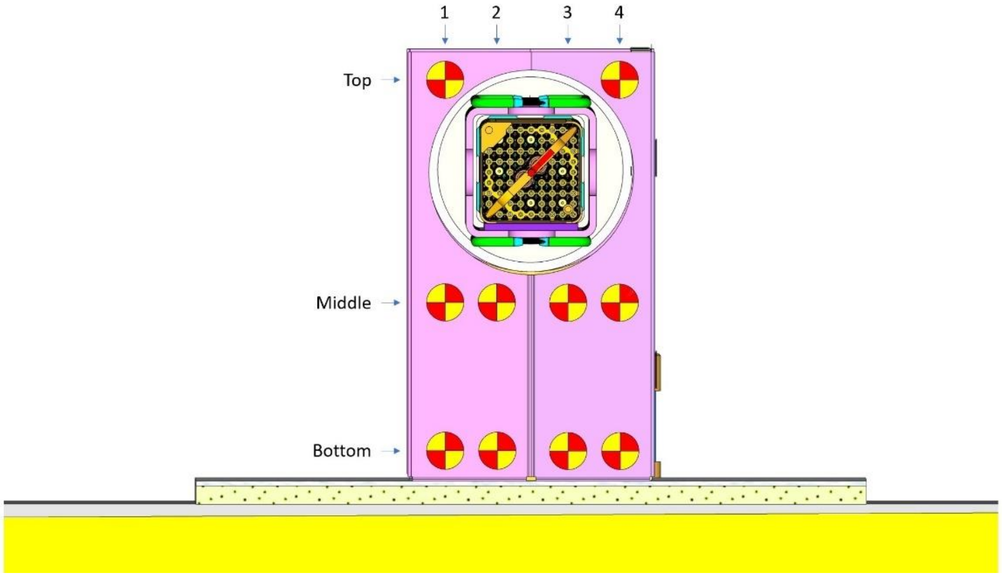

Figure C.4 Emissivity measurement locations on the end of the vault at the top of the HDCS assembly, indicated by the yellow and red circles.

The locations are identical for the end of the vault at the bottom of the assembly.

Table C.1 Emissivity values for the top end of the HDCS vault.

	Column			
	1	2	3	4
Top	0.294	-	-	0.271
Middle	0.292	0.282	0.273	0.262
Bottom	0.284	0.282	0.272	0.272

Table C.2 Emissivity values for the bottom end of the HDCS vault.

	Column			
	1	2	3	4
Top	0.298	-	-	0.275
Middle	0.289	0.279	0.281	0.272
Bottom	0.277	0.285	0.269	0.272

C.3 Emissivity Profile Analysis

The emissivity values for the four interior sides of the vault remain constant across the vault's axial length and on both ends of the vault. The bottom interior surface showed a different value for the emissivity than the other sides, due to a layer of oxidation across the entire surface of the stainless-steel plate that was formed prior to and independent of the HDCS testing.

C.4 Verification of Measurements

C.4.1 Measurement Sample Size Justification

To justify the sample size choice of 6 measurements per measurement location, 30 measurements were done at select axial levels by doing 5 rounds of 6 measurements on each surface and the 95% confidence intervals about the means of the 30-measurement population and one 6-measurement sample were determined. Table C.3 shows the emissivity means and 95% confidence intervals for the 30-measurement population and a 6-measurement sample from that population for the chosen axial levels on each of the four interior sides of the HDCS vault.

The overlap of the 95% confidence intervals about the mean of each sample of 6 measurements and its representative population of 30 measurements on every side of the HDCS vault measured indicate that the choice of 6 measurements on each surface is valid in regard to being representative of a larger population, since the average emissivity values of the 6-measurement sample and the 30-measurement population are statistically the same for every emissivity measurement across all four interior sides of the vault at all axial levels.

Table C.3 Average emissivity values of the HDCS vault on each interior side for 6 versus 30-measurement samples and their 95% confidence intervals.

Axial Level (m)	Side	Quarter-Point	Emissivity 30-sample mean	Emissivity 6-sample mean
0.610	Top	First	0.277 ± 0.001	0.277 ± 0.001
0.610	Top	Third	0.283 ± 0.001	0.286 ± 0.003
0.610	South	First	0.270 ± 0.001	0.270 ± 0.003
0.610	South	Third	0.275 ± 0.001	0.274 ± 0.003
0.610	North	First	0.268 ± 0.001	0.268 ± 0.002
0.610	North	Third	0.265 ± 0.001	0.267 ± 0.002
0.610	Bottom	First	0.444 ± 0.002	0.446 ± 0.005
0.610	Bottom	Third	0.421 ± 0.002	0.420 ± 0.003
3.658	Top	First	0.278 ± 0.001	0.278 ± 0.002
3.658	Top	Third	0.278 ± 0.001	0.277 ± 0.003
3.658	South	First	0.274 ± 0.002	0.268 ± 0.007
3.658	South	Third	0.285 ± 0.001	0.280 ± 0.003
3.658	North	First	0.276 ± 0.001	0.276 ± 0.001
3.658	North	Third	0.272 ± 0.001	0.270 ± 0.002
3.658	Bottom	First	0.463 ± 0.004	0.468 ± 0.005
3.658	Bottom	Third	0.472 ± 0.004	0.467 ± 0.005

C.5 Conclusions

An ET 100 reflectometer was used to measure the emissivity of the horizontal dry cask simulator vault. The procedure used to obtain these emissivities was the same as those used to measure the emissivities of the dry cask simulator structures. Due to the components of the vault being made of stainless steel, the emissivity values were about the same throughout most of the vault structure. However, the bottom interior surface was made from stainless steel with a layer of oxidation, so the emissivity profile of this surface differed from the other surfaces.

This page is intentionally left blank.

APPENDIX D VAULT WEIGHTS AND DIMENSIONS

This Appendix provides details on the dimensions and weights of the various components used in the construction of the HDCS vault. The vault components are all made of 11-gauge stainless steel (0.003 m thickness) except for the bottom platform, which is made of 0.006 m-thick stainless steel with 0.0254 m of DuraBoard ceramic insulation underneath. The dimension measurements were found by taking the average of multiple measurements along a given lateral direction. Figure D.1 gives a top-down view of the HDCS system and defines the spatial orientation of the components referenced in this Appendix. Figure D.2 through Figure D.9 show the various dimension measurement locations for the HDCS vault components. For each component, a 2D *xy*-plane was defined by taking the origin as the bottom-left corner of the component. Table D.1 through Table D.6 give the weights and dimensions of the components of the HDCS vault except for the vault inlets and vault outlets, which have their weights and dimensions included in Figure D.8 and Figure D.9.

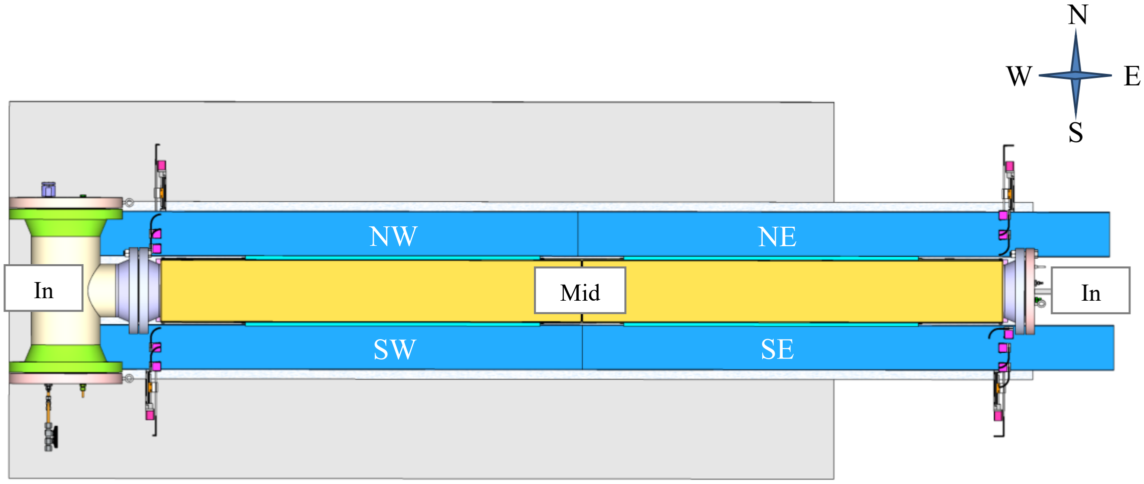

Figure D.1 **Top-down view of the HDCS system, with the spatial orientation indicated by the compass.**

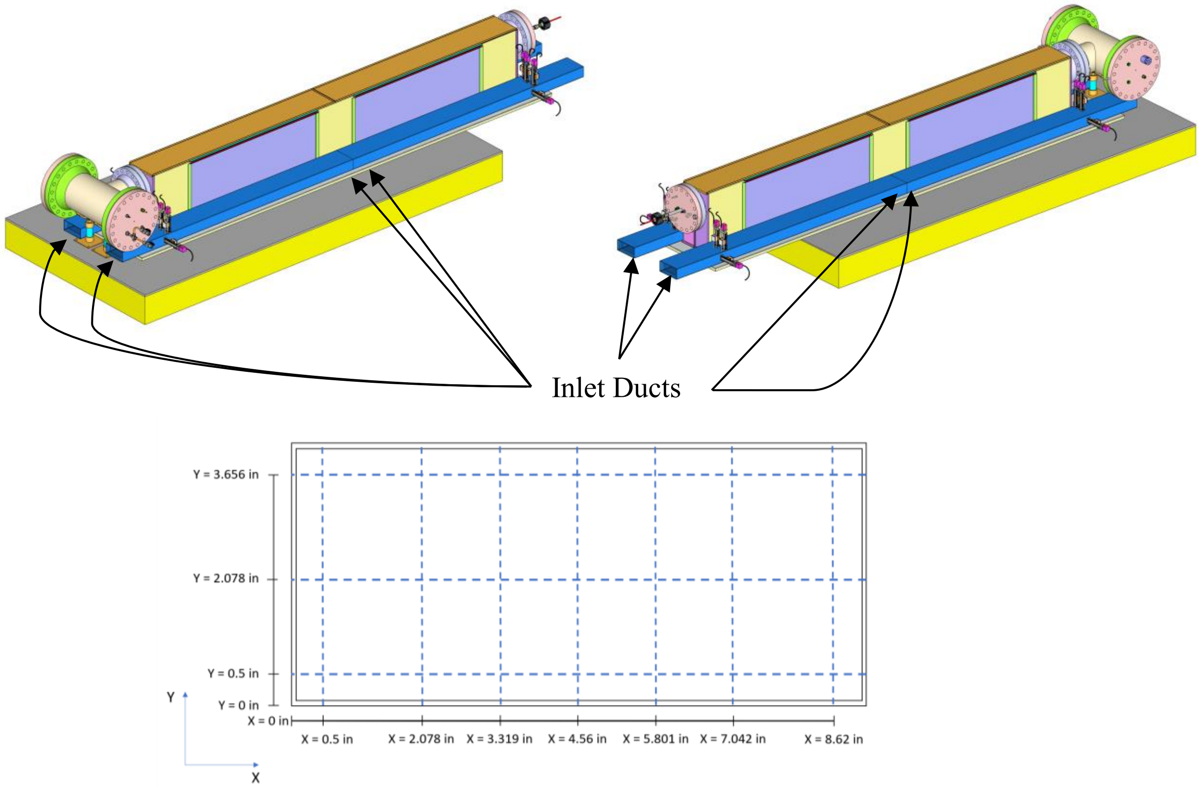

Figure D.2 Dimension measurement locations for the inlet ducts.

Table D.1 Inlet duct opening dimensions.

Item	Material	Weight (kg)	OD (m)	ID (m)
Inlet duct (SE In) average *x*-dim.	Stainless Steel	58.012	0.232	0.228
Inlet duct (SE In) average *y*-dim.	Stainless Steel	58.012	0.106	0.103
Inlet duct (SE Mid) average *x*-dim.	Stainless Steel	58.012	0.232	0.228
Inlet duct (SE Mid) average *y*-dim.	Stainless Steel	58.012	0.106	0.102
Inlet duct (NE In) average *x*-dim.	Stainless Steel	58.128	0.233	0.229
Inlet duct (NE In) average *y*-dim.	Stainless Steel	58.128	0.106	0.102
Inlet duct (NE Mid) average *x*-dim.	Stainless Steel	58.128	0.233	0.229
Inlet duct (NE Mid) average *y*-dim.	Stainless Steel	58.128	0.107	0.104
Inlet duct (SW In) average *x*-dim.	Stainless Steel	57.994	0.232	0.229
Inlet duct (SW In) average *y*-dim.	Stainless Steel	57.994	0.106	0.102
Inlet duct (SW Mid) average *x*-dim.	Stainless Steel	57.994	0.232	0.228
Inlet duct (SW Mid) average *y*-dim.	Stainless Steel	57.994	0.106	0.102
Inlet duct (NW In) average *x*-dim.	Stainless Steel	58.112	0.232	0.228
Inlet duct (NW In) average *y*-dim.	Stainless Steel	58.112	0.107	0.103
Inlet duct (NW Mid) average *x*-dim.	Stainless Steel	58.112	0.232	0.228
Inlet duct (NW Mid) average *y*-dim.	Stainless Steel	58.112	0.106	0.103

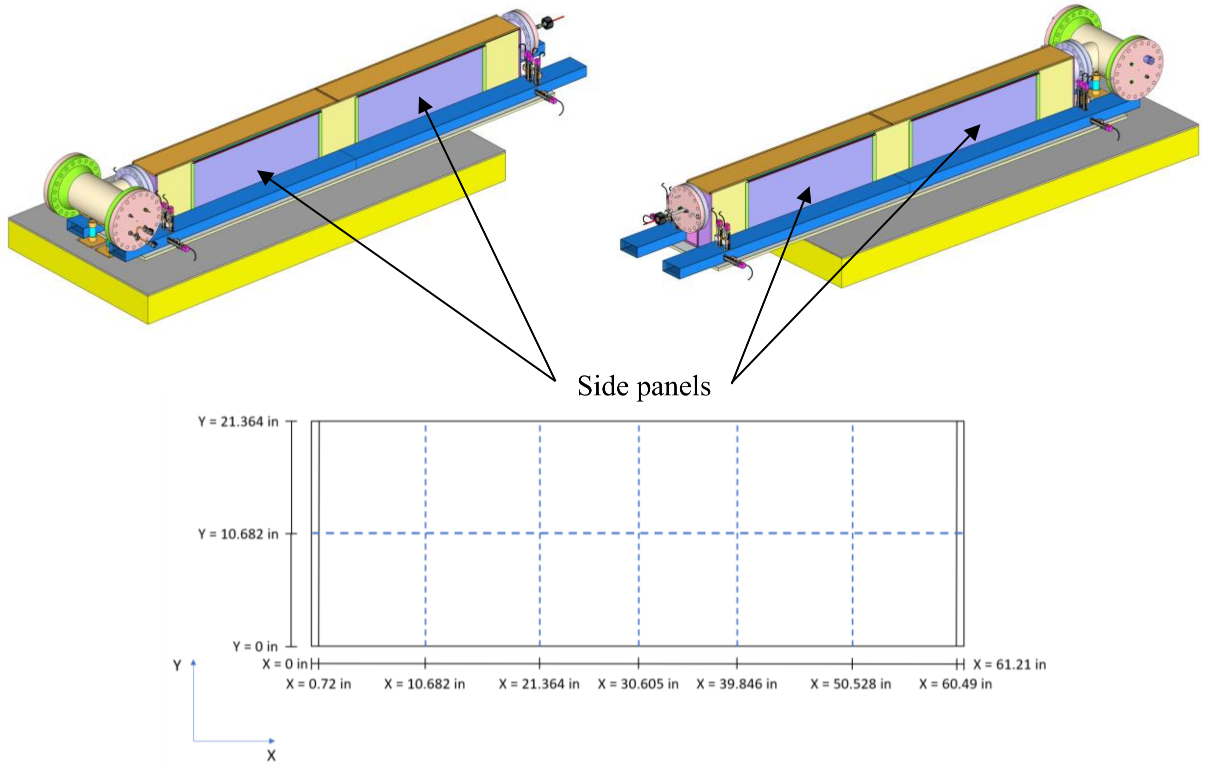

Figure D.3 Dimension measurement locations for the side panels.

Table D.2 Side panel dimensions.

Item	Material	Weight (kg)	Thickness (m)	OD (m)	ID (m)
Side panel (SE) average *x*-dim.	Stainless Steel	20.403	0.003	1.555	1.519
Side panel (SE) average *y*-dim.	Stainless Steel	20.403	0.003	0.543	
Side panel (NE) average *x*-dim.	Stainless Steel	20.430	0.003	1.555	1.519
Side panel (NE) average *y*-dim.	Stainless Steel	20.430	0.003	0.543	
Side panel (SW) average *x*-dim.	Stainless Steel	20.429	0.003	1.555	1.519
Side panel (SW) average *y*-dim.	Stainless Steel	20.429	0.003	0.543	
Side panel (NW) average *x*-dim.	Stainless Steel	20.415	0.003	1.556	1.519
Side panel (NW) average *y*-dim.	Stainless Steel	20.415	0.003	0.543	

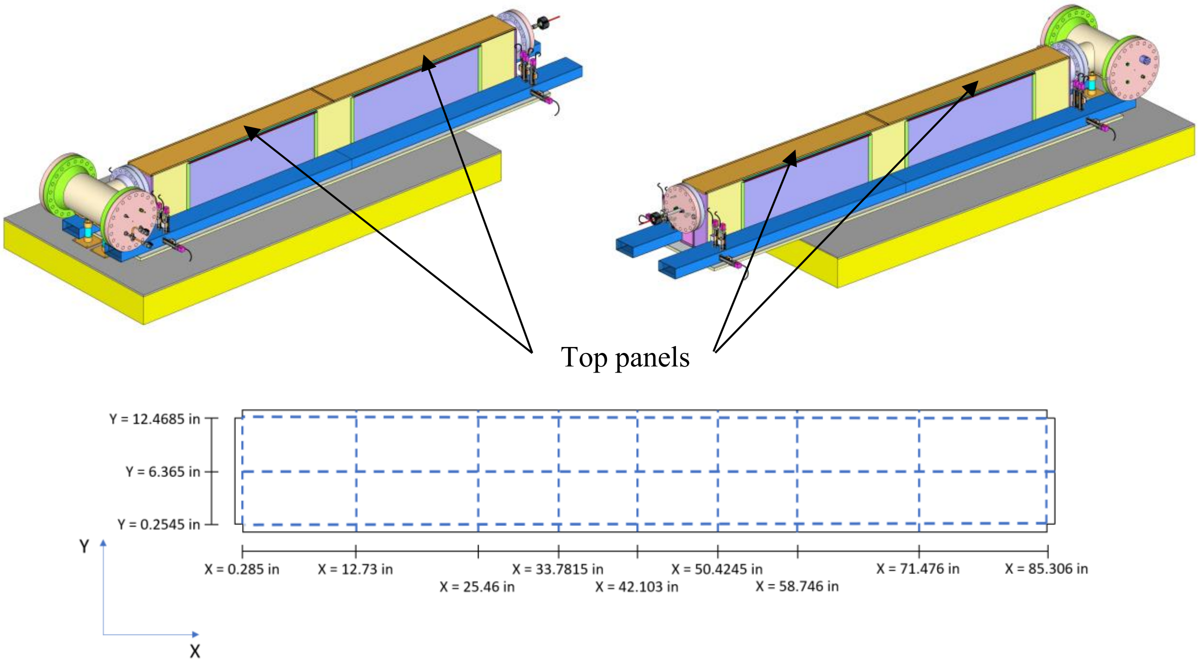

Figure D.4 Dimension measurement locations for the top panels.

Table D.3 Top panel dimensions.

Item	**Material**	**Weight (kg)**	**Thickness (m)**	**Length (m)**
Top panel (E) average *x*-dim.	Stainless Steel	17.863	0.003	2.174
Top panel (E) average *y*-dim.	Stainless Steel	17.863	0.003	0.324
Top panel (W) average *x*-dim.	Stainless Steel	17.854	0.003	2.174
Top panel (W) average *y*-dim.	Stainless Steel	17.854	0.003	0.324

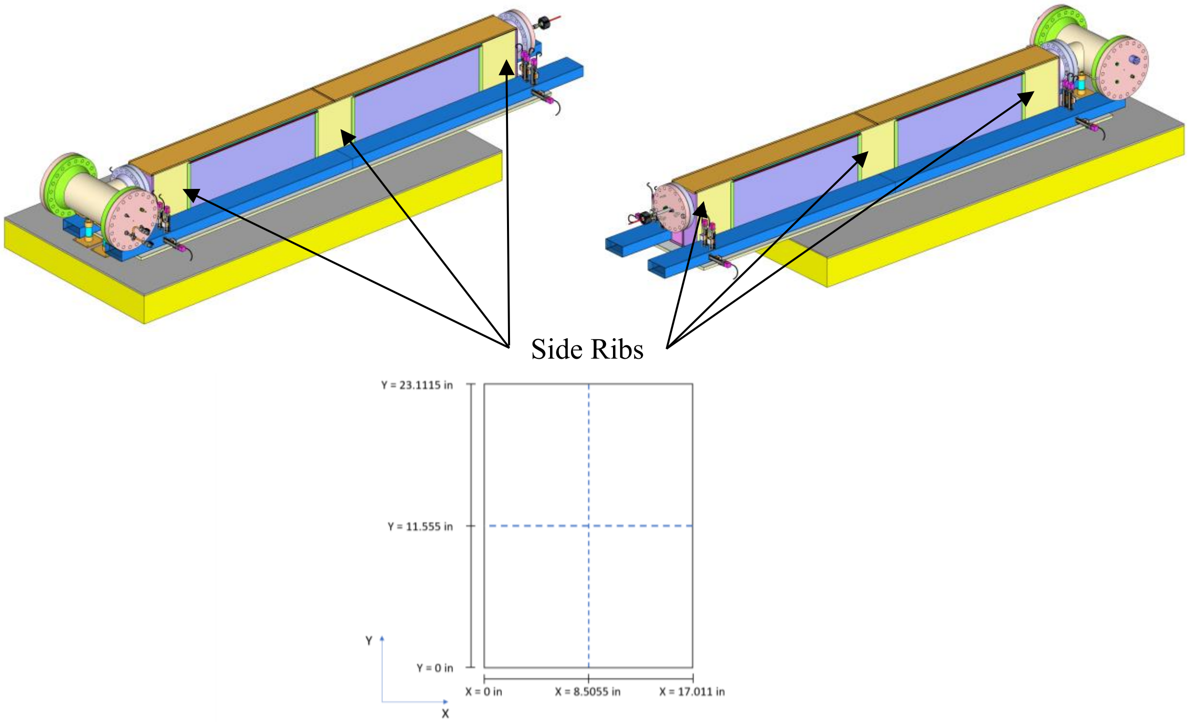

Figure D.5 Dimension measurement locations for the side ribs.

Table D.4 Inlet duct opening dimensions.

Item	**Material**	**Weight (kg)**	**Thickness (m)**	**Length (m)**
Side rib (SE) average *x*-dim.	Stainless Steel	6.390	0.003	0.432
Side rib (SE) average *y*-dim.	Stainless Steel	6.390	0.003	0.587
Side rib (N) average *x*-dim.	Stainless Steel	6.394	0.003	0.432
Side rib (N) average *y*-dim.	Stainless Steel	6.394	0.003	0.587
Side rib (NE) average *x*-dim.	Stainless Steel	6.390	0.003	0.432
Side rib (NE) average *y*-dim.	Stainless Steel	6.390	0.003	0.587
Side rib (SW) average *x*-dim.	Stainless Steel	6.392	0.003	0.433
Side rib (SW) average *y*-dim.	Stainless Steel	6.392	0.003	0.587
Side rib (S) average *x*-dim.	Stainless Steel	6.392	0.003	0.432
Side rib (S) average *y*-dim.	Stainless Steel	6.392	0.003	0.587
Side rib (NW) average *x*-dim.	Stainless Steel	6.390	0.003	0.432
Side rib (NW) average *y*-dim.	Stainless Steel	6.390	0.003	0.588

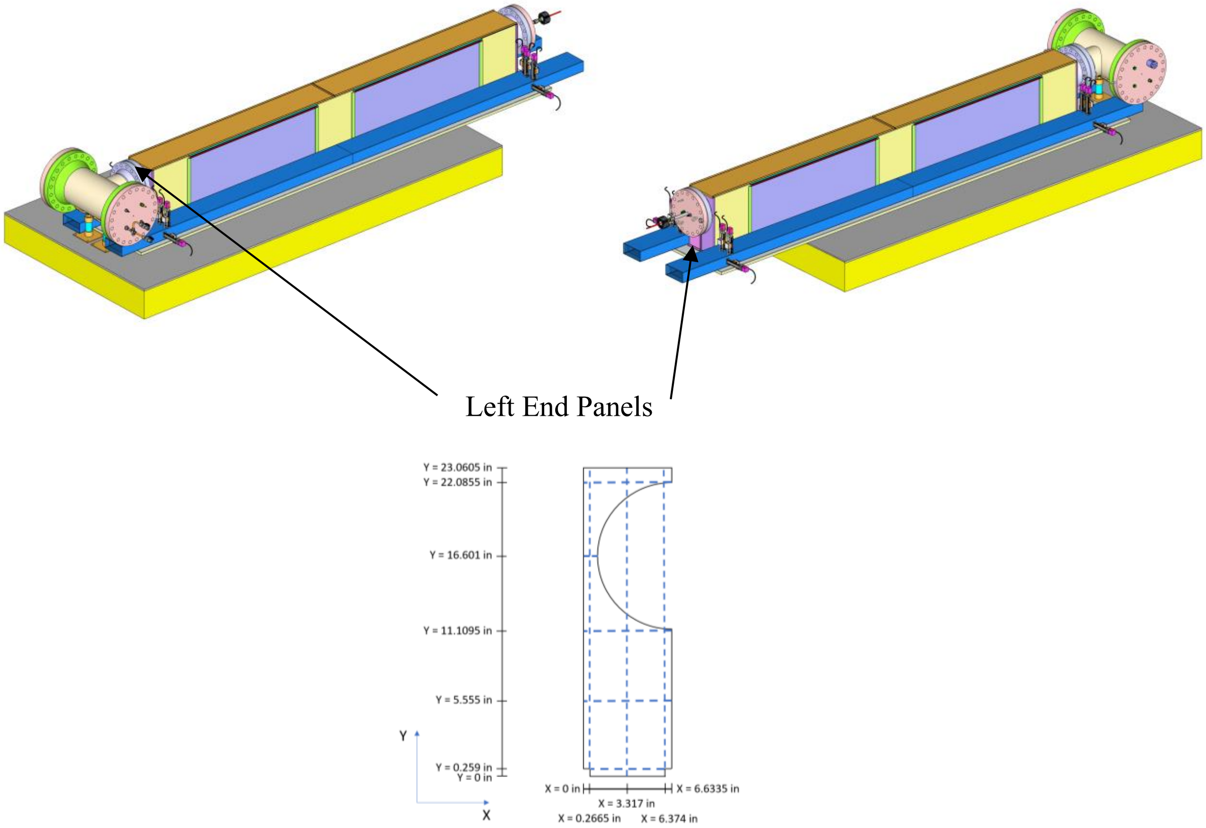

Figure D.6 Dimension measurement locations for the left end panels.

Table D.5 Left end panel dimensions.

Item	Material	Weight (kg)	Thickness (m)	Length (m)
Left end panel (S) average *x*-dim. (long length)	Stainless Steel	1.897	0.003	0.169
Left end panel (S) *x*-dim. (short length)	Stainless Steel	1.897	0.003	0.035
Left end panel (S) average *y*-dim.	Stainless Steel	1.897	0.003	0.586
Left end panel (N) average *x*-dim. (long length)	Stainless Steel	1.895	0.003	0.168
Left end panel (N) *x*-dim. (short length)	Stainless Steel	1.895	0.003	0.029
Left end panel (N) average *y*-dim.	Stainless Steel	1.895	0.003	0.586

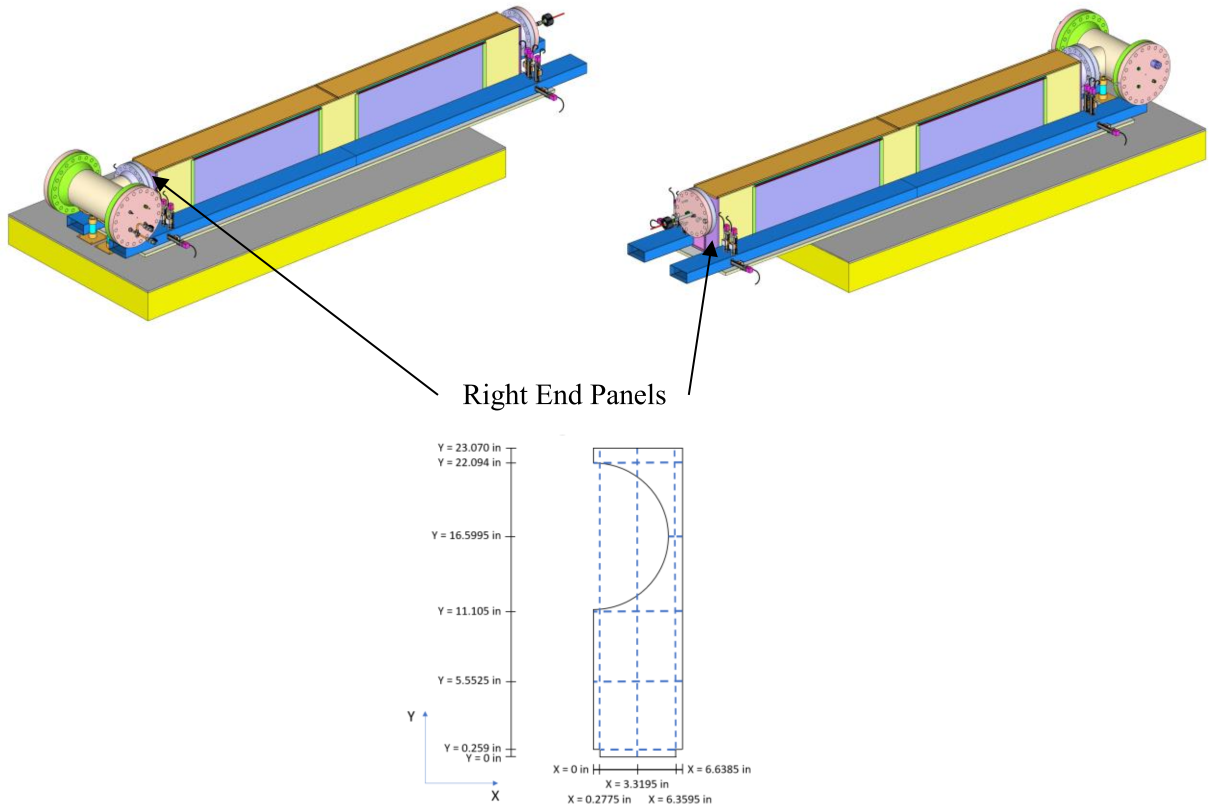

Figure D.7 Dimension measurement locations for the right end panels.

Table D.6 Right end panel dimensions.

Item	Material	Weight (kg)	Thickness (m)	Length (m)
Right end panel (N) average *x*-dim. (long length)	Stainless Steel	1.897	0.003	0.169
Right end panel (N) *x*-dim. (short length)	Stainless Steel	1.897	0.003	0.029
Right end panel (N) average *y*-dim.	Stainless Steel	1.897	0.003	0.586
Right end panel (S) average *x*-dim. (long length)	Stainless Steel	1.896	0.003	0.169
Right end panel (S) *x*-dim. (short length)	Stainless Steel	1.896	0.003	0.029
Right end panel (S) average *y*-dim.	Stainless Steel	1.896	0.003	0.586

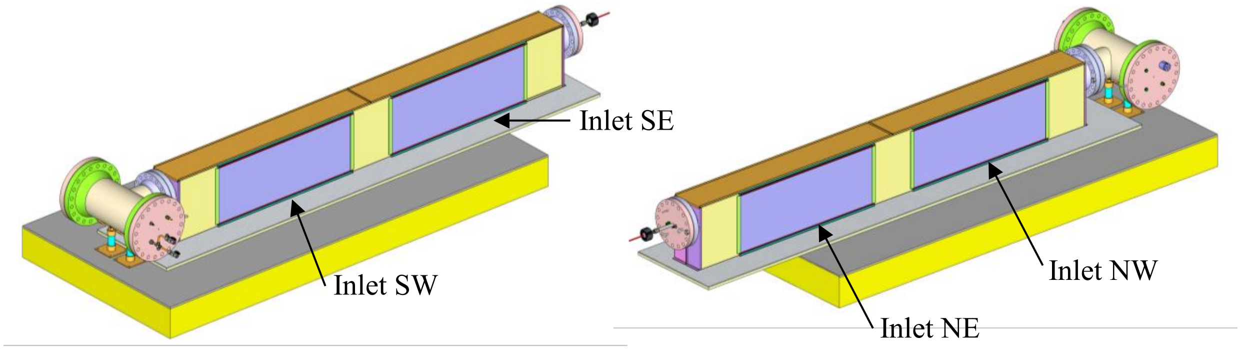

Vault Inlet (SE)

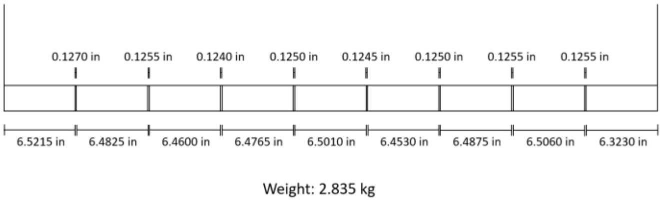

Vault Inlet (NE)

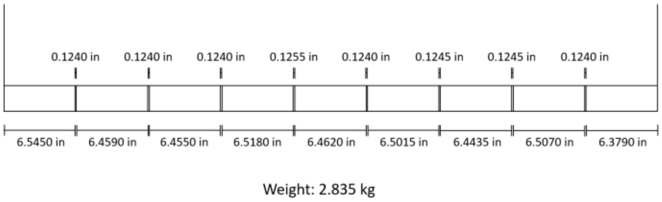

Vault Inlet (SW)

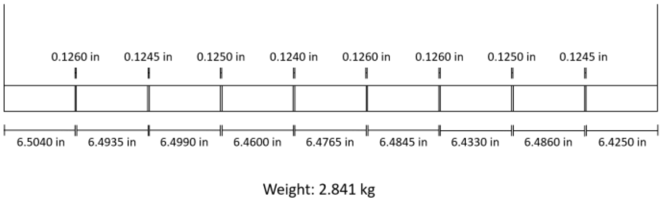

Vault Inlet (NW)

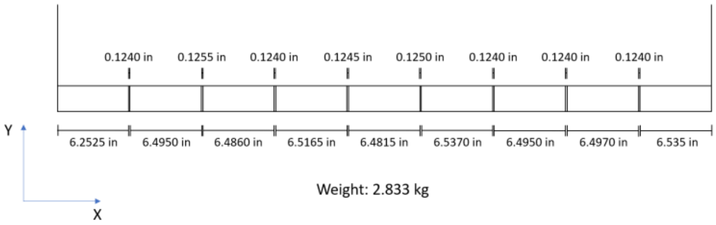

Figure D.8 Dimension measurements for the stainless steel vault inlets.

The vault inlets extend from the inlet ducts and enter the vault, so the 3D isometric view has the inlet ducts hidden to expose the vault inlets. The short dimension in the vault inlet openings could not be accessed and therefore were not measured.

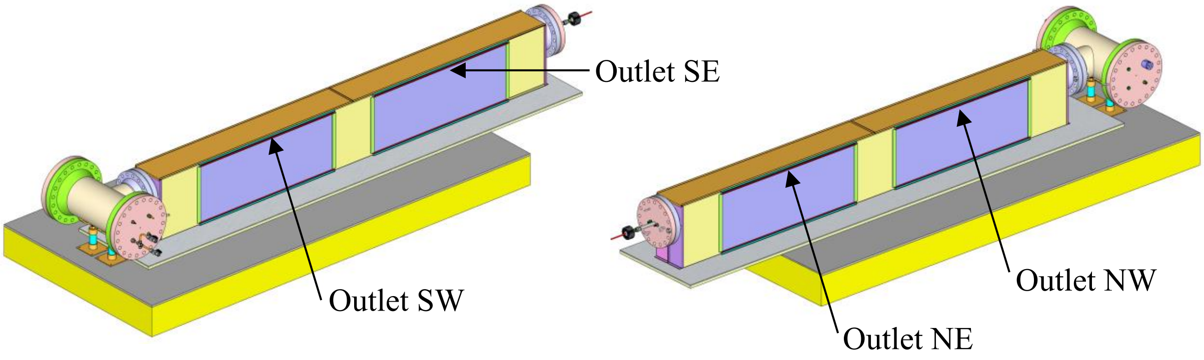

Vault Outlet (SE)

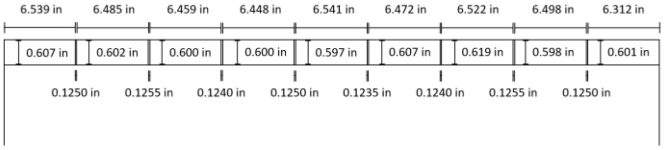

Weight: 2.837 kg

Vault Outlet (NE)

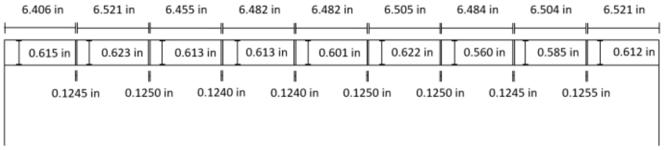

Weight: 2.821 kg

Vault Inlet (SW)

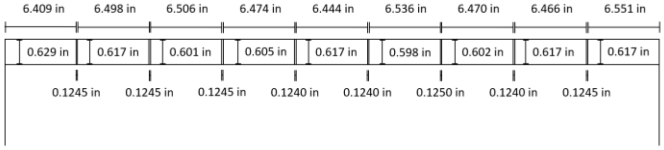

Weight: 2.841 kg

Vault Outlet (NW)

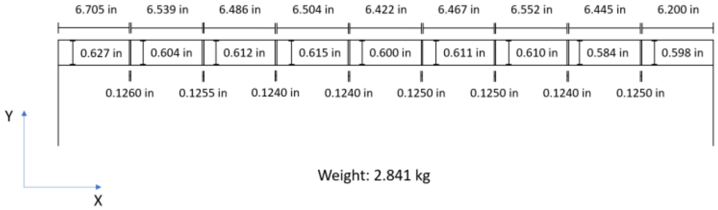

Weight: 2.841 kg

Figure D.9 Dimension measurements for the stainless steel vault outlets.

This page is intentionally left blank.

APPENDIX E HYDRAULIC DIAMETER MEASUREMENTS

E.1 Methodology

The purpose of this appendix is to estimate the hydraulic diameters (D_h) of the inlet ducts and vault inlets. Areas and perimeters are processed with ImageJ software using high contrast pixel measurement. Perimeters are measured that factor in the rounded corners of the sheet metal via approximation with small straight-line segments. The values obtained from the pictures (D_h') will be obtained from the analyzed duct area A_w and wetted perimeter P_w, using a pixel scaling constant f:

$$D_h' = \frac{4A_w}{P_w} * f \tag{E-1}$$

This value can then be compared to the analytical (design-basis) and measured (as-built) value of D_h for error. The numbering scheme for the inlet ducts and vault inlets is shown in Figure E.1 with cardinal directions.

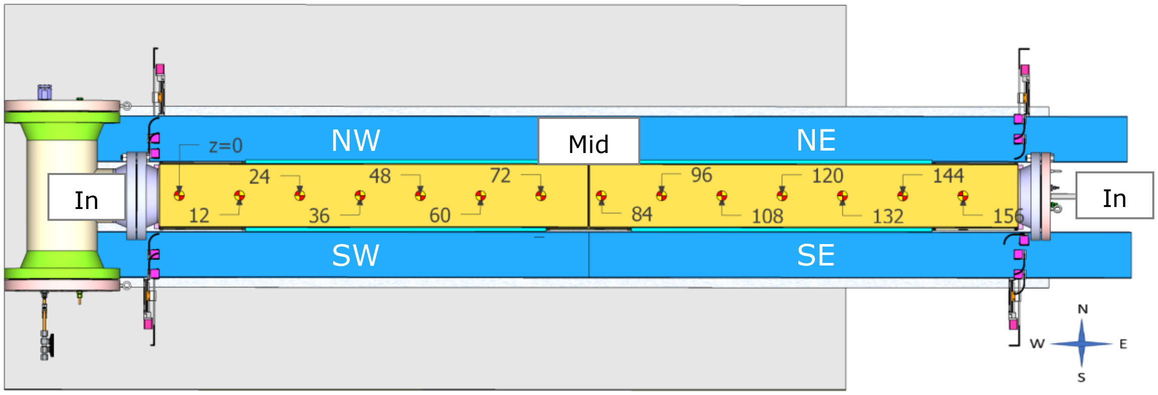

All dimensions are in inches

Figure E.1 Labeling scheme for ducting.

E.2 Inlet Ducts

The inlet duct design parameters are summarized in Table E.1, where analytical values factor in the effects of the sheet metal rounding radii and the approximate values assume a perfect rectangle.

The measured D_h is based on the averages of the inner diameters for the x direction (six measurements) and y direction (three measurements) for a given duct and side from Appendix D. The average measured D_h is 5.576 ± 0.068 in., which is 0.274% off the design value of 5.561 in.

The inner height measurement at $x = 0.5$ in. was used for scaling pixels in the image to real length (see Figure E.2). Results are shown in Table E.2 where the D_h' of the duct is expected to be 5.523 ± 0.034 in. The typical error from the design D_h is -0.672%, while the error from the measured D_h is -0.943%.

Table E.1 Design parameters for the inlet ducts, where sheet metal is 5/64 in. thick.

	Duct area (A_w, in^2)	Wetted Perimeter (P_w, in.)	Outer area (A_o, in^2)	Facial area (A_f, in^2)	Inner rounding radius (r_i, in.)	Outer rounding radius (r_o, in.)	D_h (in.)
Approx	36	26	38.056	2.056	0.063	0.141	5.538462
Analytical	35.9966	25.8918	38.026	2.0294	"	"	5.561081

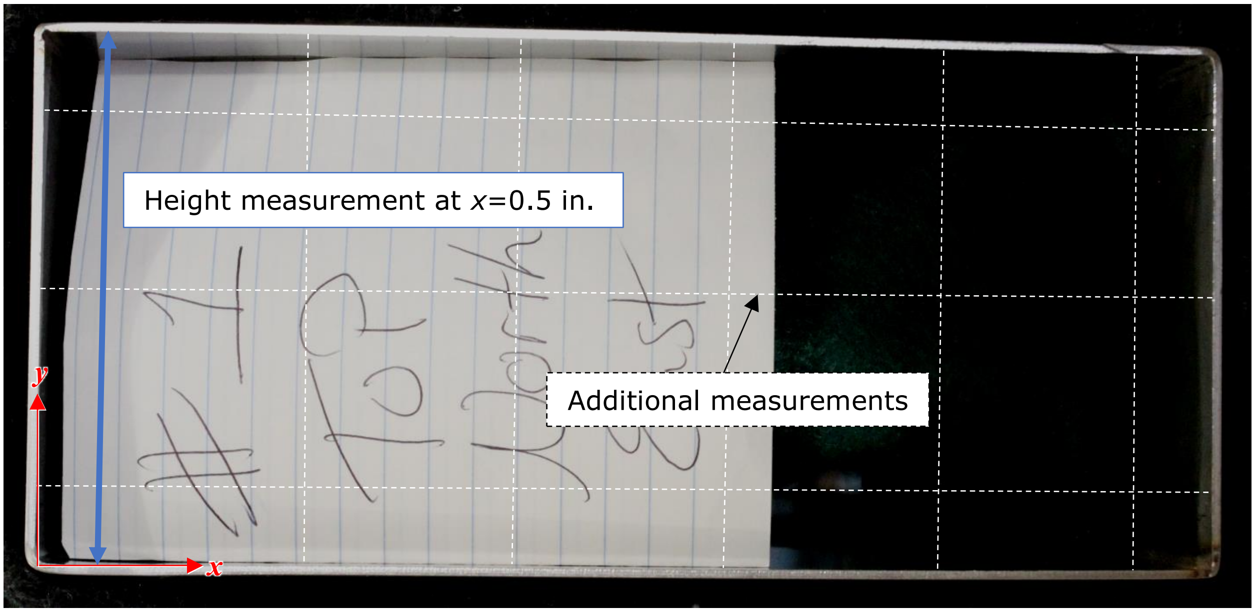

Figure E.2 Inlet of duct #1 showing direct measurement used for calibration and additional measurements.

Table E.2 Measured D_h for the inlet ducts using caliper measurement at $x = 0.5$ in. for scaling.

Duct	Measured D_h (in.)	D_h Error (in.)	Wetted Perimeter from Photos (in.)	Flow Area from Photos (in^2)	D_h’ from Photos (in.)	Error from Measurement
SE_MID	5.562	0.018	25.291	35.011	5.537	-0.442%
SE_IN	5.574	0.015	25.520	35.170	5.513	-1.104%
NW_MID	5.579	0.022	25.948	36.310	5.597	0.332%
NW_IN	5.598	0.026	25.761	35.526	5.516	-1.451%
NE_MID	5.620	0.037	25.487	35.178	5.521	-1.763%
NE_IN	5.573	0.022	25.540	35.285	5.526	-0.843%
SW_MID	5.544	0.016	25.431	34.909	5.491	-0.954%
SW_IN	5.561	0.029	25.343	34.774	5.489	-1.308%

E.3 Vault Inlets

The vault inlets are calibrated with the width measurements obtained for each vent (see Figure E.3). Analysis could only be conducted on images of the curved surface of the inlet vents. The D_h is obtained through the summation of wetted perimeters and areas for each of the nine vents. Results are shown in Table E.3, where the inlet D_h can be expected to be around 1.125 ± 0.013 in. Measurement error is not listed because caliper measurements could not be obtained for the heights of the vents.

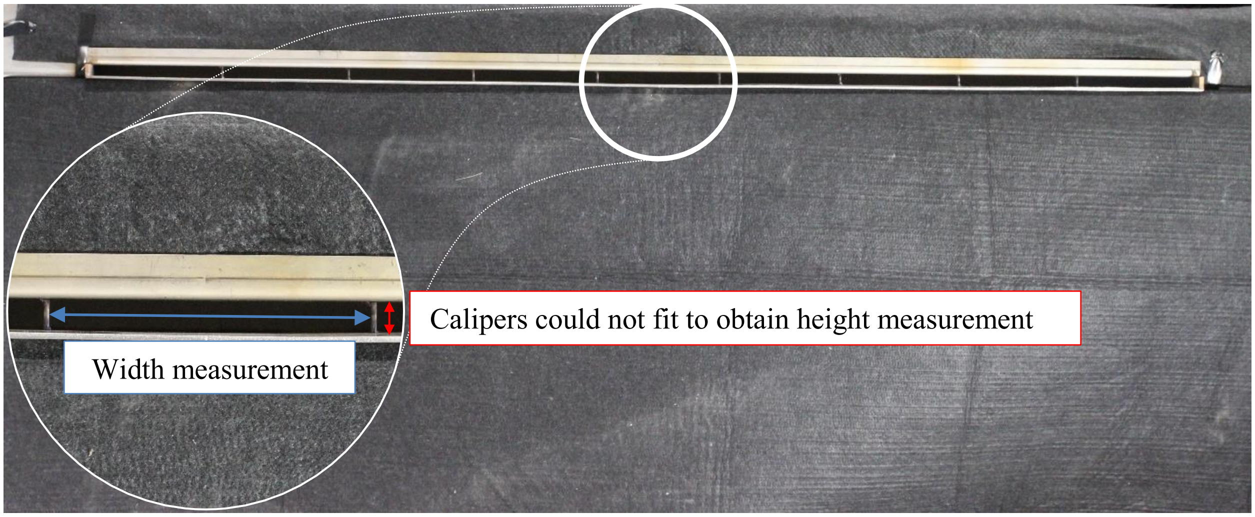

Figure E.3 Inlet #1 shown with inset for 5th vent.

Table E.3 D_h’ for the vault inlets as obtained from photos.

Inlet	Wetted Perimeter (in.)	Flow Area (in^2)	D_h’ (in.)
VI_SE	127.424	35.800	1.124
VI_NW	127.823	35.919	1.124
VI_NE	127.748	36.494	1.143
VI_SW	127.344	35.359	1.111

E.4 Unwelded Vault Outlets

The measured D_h for the vault outlets are shown in Table E.4, where the average value is 1.109 ± 0.044 in. The photo analysis for the vault outlets is calibrated using the width measurements obtained for each vent, and digital measurements are made using images of the flat surfaces (see Figure E.4). Results are shown in Table E.4, where the outlet D_h’ can be expected to be around 1.145 ± 0.010 in.

Table E.4 D_h’ for the vault outlets.

Inlet	Measured D_h (in.)	D_h Error (in.)	Wetted Perimeter (in.) from Photos	Flow Area (in^2) from Photos	D_h’ (in.) from Photos	Error from Measurement
VO_SE	1.104	0.011	127.528	36.276	1.138	-3.079%
VO_NW	1.109	0.019	127.842	37.009	1.158	-4.379%
VO_NE	1.106	0.034	127.938	36.333	1.136	-2.681%
VO_SW	1.117	0.017	128.262	36.883	1.150	-2.949%

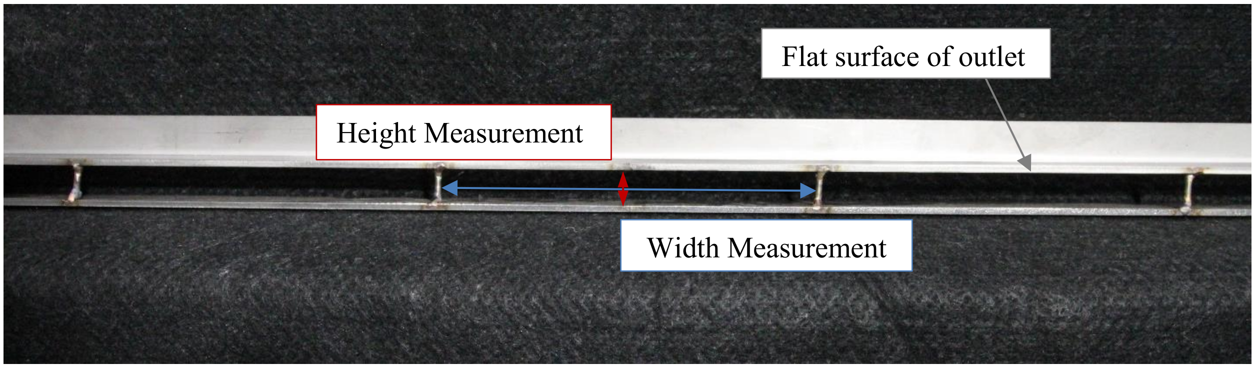

Figure E.4 Middle of outlet #1 showing flat surface used for analysis.

APPENDIX F LIST OF INSTRUMENTATION EXTERNAL TO THE PRESSURE VESSEL

F.1 Conventions

A right-hand coordinate system is employed based on an origin defined by the top of the bottom tie plate in the assembly (see Figure 2.10). Based on the orientation of the assembly within the facility, *x* points downward, *y* points northward, and *z* points eastward. Maintaining terminology from previous vertically-oriented tests, the *z*-component increases from the "bottom" to the "top" of the structure.

A labeling system is devised for instrumentation that identifies the abbreviated name of the adjoining vault component, the cardinal direction, and the cartesian coordinates. For example, on the vault side panel, "SP_S_10.808_-6.5_108" denotes a thermocouple on the side panel facing south 10.808 inches towards the baseplate, 6.5 inches south, and 108 inches east from the origin.

F.2 Thermocouples

F.2.1 Vault Thermocouples

The vault thermocouples are listed in Table F.1 and diagrammed in Figure F.1 through Figure F.3. Those that are installed on the inside of the vault (i.e. facing the pressure vessel) are indicated.

Table F.1 List of thermocouples on the vault top and side panels.

#	Face	Dir.	Label	*x* (in.)	*y* (in.)	*z* (in.)	Type
231	E	W	TP_W_-6.661_0_0	-6.661	0	0	TC (Type-K)
232	E	W	TP_W_-6.661_0_12	-6.661	0	12	TC (Type-K)
233	E	W	TP_W_-6.661_0_24	-6.661	0	24	TC (Type-K)
234	E	W	TP_W_-6.661_0_36	-6.661	0	36	TC (Type-K)
235	E	W	TP_W_-6.661_0_48	-6.661	0	48	TC (Type-K)
236	E	W	TP_W_-6.661_0_60	-6.661	0	60	TC (Type-K)
237	E	W	TP_W_-6.661_0_72	-6.661	0	72	TC (Type-K)
238	E	E	TP_E_-6.661_0_84	-6.661	0	84	TC (Type-K)
239	I	E	TP_INT_E_-6.536_0_84	-6.536	0	84	TC (Type-K)
240	E	E	TP_E_-6.661_0_96	-6.661	0	96	TC (Type-K)
241	E	E	TP_E_-6.661_0_108	-6.661	0	108	TC (Type-K)
242	E	E	TP_E_-6.661_0_120	-6.661	0	120	TC (Type-K)
243	E	E	TP_E_-6.661_0_132	-6.661	0	132	TC (Type-K)
244	E	E	TP_E_-6.661_0_144	-6.661	0	144	TC (Type-K)
245	E	E	TP_E_-6.661_0_156	-6.661	0	156	TC (Type-K)
246	E	SW	RIB_SW_5.027_-6.5_0	5.0	-6.5	0	TC (Type-K)
247	E	S	SP_S_10.808_-6.5_24	10.8	-6.5	24	TC (Type-K)
248	E	S	SP_S_-0.755_-6.5_24	-0.8	-6.5	24	TC (Type-K)
249	E	S	SP_S_5.027_-6.5_48	5.0	-6.5	48	TC (Type-K)
250	E	S	SP_S_10.808_-6.5_71	10.8	-6.5	71*	TC (Type-K)
251	E	S	SP_S_-0.755_-6.5_71	-0.8	-6.5	71*	TC (Type-K)
252	E	S	RIB_S_5.027_-6.5_84	5.0	-6.5	84	TC (Type-K)
253	I	S	RIB_INT_S_5.027_-6.375_84	5.0	-6.375	84	TC (Type-K)

#	Face	Dir.	Label	*x* (in.)	*y* (in.)	*z* (in.)	Type
254	E	S	SP_S_10.808_-6.5_108	10.8	-6.5	108	TC (Type-K)
255	E	S	SP_S_-0.755_-6.5_108	-0.8	-6.5	108	TC (Type-K)
256	E	S	SP_S_5.027_-6.5_132	5.0	-6.5	132	TC (Type-K)
257	E	SE	RIB_SE_10.808_-6.5_156	10.8	-6.5	156	TC (Type-K)
258	E	SE	RIB_SE_-0.755_-6.5_156	-0.8	-6.5	156	TC (Type-K)
259	E	NW	RIB_NW_10.808_6.5_0	10.8	6.5	0	TC (Type-K)
260	E	NW	RIB_NW_-0.755_6.5_0	-0.8	6.5	0	TC (Type-K)
261	E	N	SP_N_5.027_6.5_24	5.0	6.5	24	TC (Type-K)
262	E	N	SP_N_10.808_6.5_48	10.8	6.5	48	TC (Type-K)
263	E	N	SP_N_-0.755_6.5_48	-0.8	6.5	48	TC (Type-K)
264	E	N	SP_N_5.027_6.5_71	5.0	6.5	71*	TC (Type-K)
265	E	N	RIB_N_10.808_6.5_84	10.8	6.5	84	TC (Type-K)
266	E	N	RIB_N_-0.755_6.5_84	-0.8	6.5	84	TC (Type-K)
267	I	N	RIB_INT_N_-0.755_6.375_84	-0.8	6.375	84	TC (Type-K)
268	E	N	SP_N_5.027_6.5_108	5.0	6.5	108	TC (Type-K)
269	E	N	SP_N_10.808_6.5_132	10.8	6.5	132	TC (Type-K)
270	E	N	SP_N_-0.755_6.5_132	-0.8	6.5	132	TC (Type-K)
271	E	NE	RIB_NE_5.027_6.5_156	5.0	6.5	156	TC (Type-K)

TP=top panel, SP=side panel, INT=interior face, E=External, I=Internal
*as-built dimension

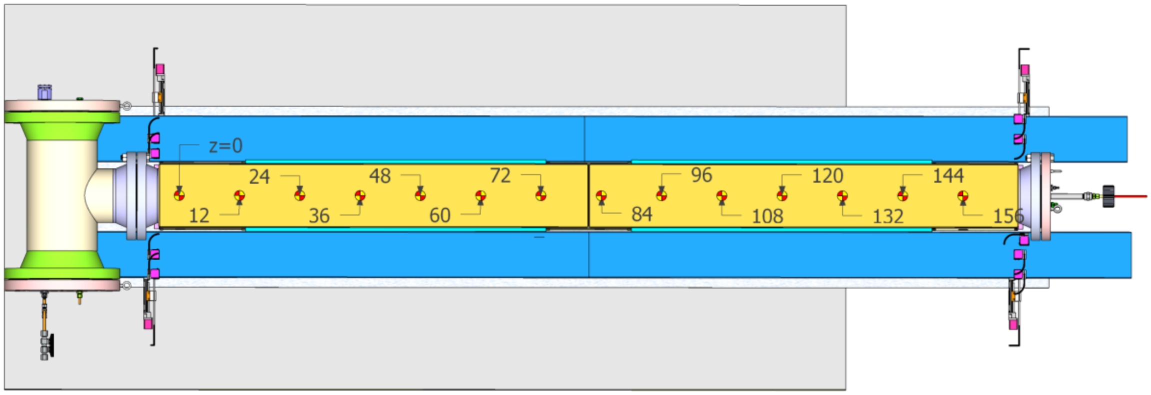

All dimensions are in inches

Figure F.1 View of top panel TCs.

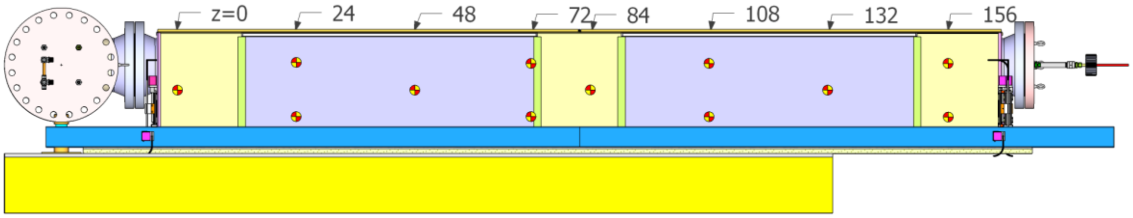

All dimensions are in inches

Figure F.2 View of southern side panel TCs.

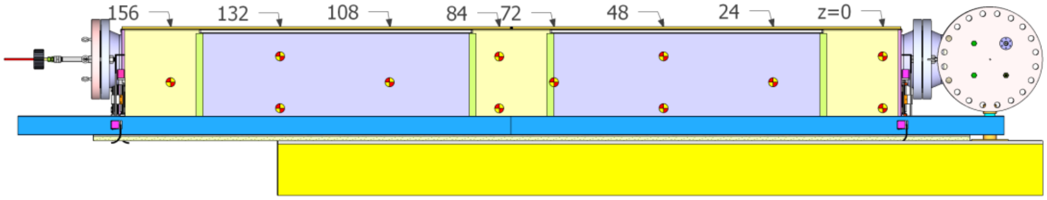

All dimensions are in inches

Figure F.3 View of northern side panel TCs.

F.2.2 Baseplate, Endplate, and Internal Thermocouples

Table F.2 List of thermocouples on the baseplate and vault endplate, as well as gas TCs around the baseplate, pressure vessel, and vault.

#	Face	Dir.	Label	*x* (in.)	*y* (in.)	*z* (in.)	Type
272	I	-	BP_TOP_16.589_0_0	16.5890	0	0	TC (Type-K)
273	I	-	g_BP_PV_10.982_0_0	10.9820	0	0	Gas-TC
274	I	-	g_PV_V_-5.973_0_0	-5.9725	0	0	Gas-TC
275	I	-	BP_TOP_16.589_0_24	16.5890	0	24	TC (Type-K)
276	I	-	BP_TOP_16.589_0_48	16.5890	0	48	TC (Type-K)
277	I	-	g_BP_PV_10.982_0_48	10.9820	0	48	Gas-TC
278	I	-	g_PV_V_-5.973_0_48	-5.9725	0	48	Gas-TC
279	I	-	BP_TOP_16.589_0_72	16.5890	0	72	TC (Type-K)
280	I	-	g_BP_PV_10.982_0_72	10.9820	0	72	Gas-TC
281	I	-	g_PV_V_-5.973_0_72	-5.9725	0	72	Gas-TC
282	I	-	BP_TOP_16.589_0_96	16.5890	0	96	TC (Type-K)
283	I	-	BP_TOP_16.589_0_120	16.5890	0	120	TC (Type-K)
284	I	-	g_BP_PV_10.982_0_120	10.9820	0	120	Gas-TC
285	I	-	g_PV_V_-5.973_0_120	-5.9725	0	120	Gas-TC
286	I	-	BP_TOP_16.589_0_144	16.5890	0	144	TC (Type-K)
287	I	-	BP_TOP_16.589_0_156	16.5890	0	156	TC (Type-K)
288	I	-	g_BP_PV_10.982_0_156	10.9820	0	156	Gas-TC
289	I	-	g_PV_V_-5.973_0_156	-5.9725	0	156	Gas-TC

#	Face	Dir.	Label	*x* (in.)	*y* (in.)	*z* (in.)	Type
290	E	SW	EP_SW_11.17_-3.31_-4.644	11.170	-3.313	-4.6	TC (Type-K)
291	E	NW	EP_NW_11.17_3.31_-4.644	11.170	3.313	-4.6	TC (Type-K)
292	E	SE	EP_SE_11.17_-3.31_166.816	11.170	-3.313	166.8	TC (Type-K)
293	E	NE	EP_NE_11.17_3.31_166.816	11.170	3.313	166.8	TC (Type-K)
334	E	-	BP_BOT_16.839_0_156	16.839	0	156.0	TC (Type-K)

BP=base plate, PV=pressure vessel, V=vault, EP=end plate, g=gas, E=External, I=Internal, BOT=bottom

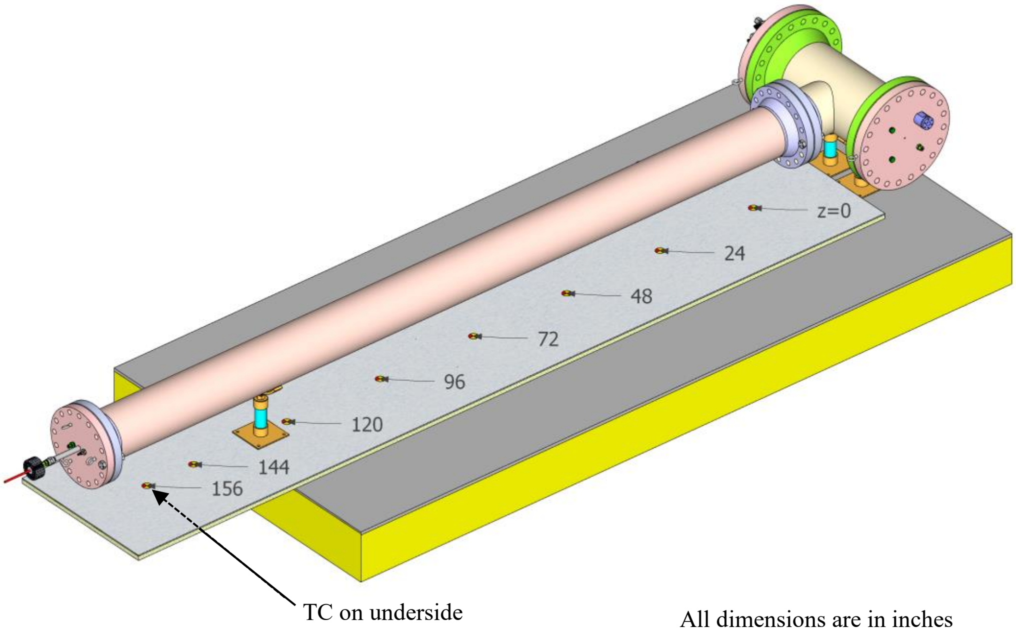

Figure F.4 Baseplate TCs.

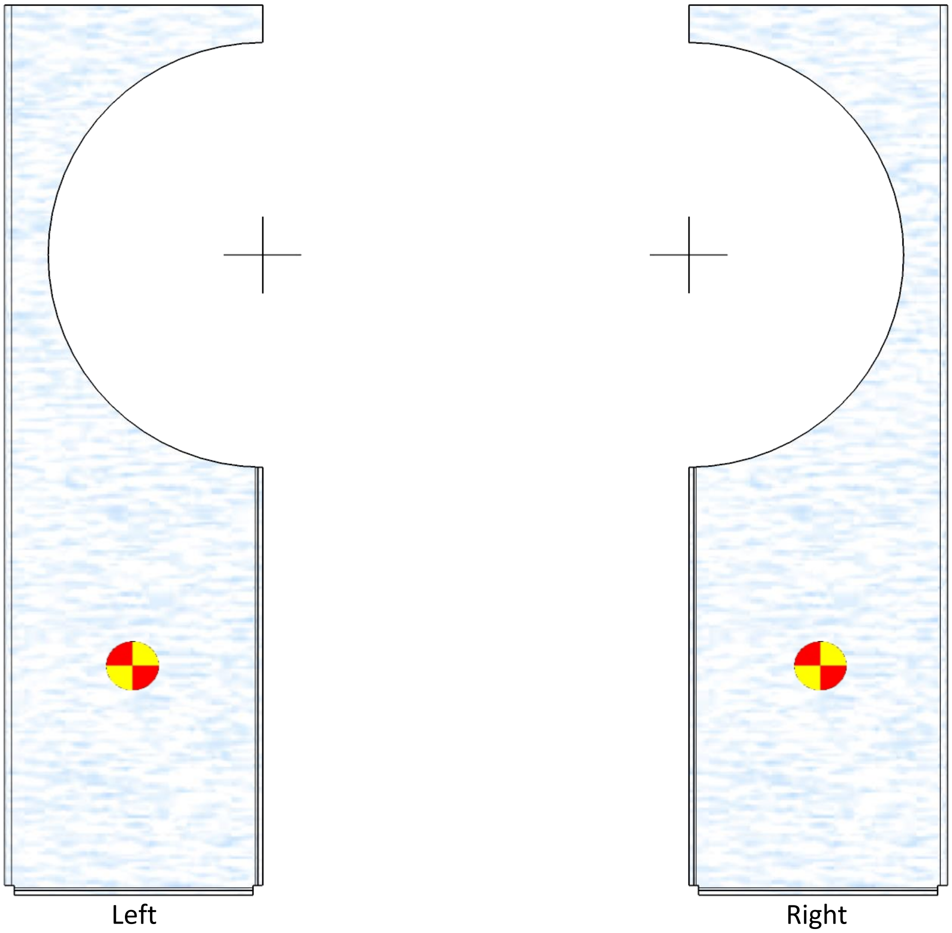

Figure F.5 Location of TCs on left and right endplates.

F.2.3 Inlet and Outlet Thermocouples

Table F.3 List of thermocouples on the vault inlets and outlets.

#	Face	Dir.	Label	*x* (in.)	*y* (in.)	*z* (in.)	Type
296	I	NW	g_INL_NW_14.511_11.7_-24.3	14.511	11.7	-24.3	Gas-TC
297	I	NW	g_INL_NW_14.511_11.7_48	14.511	11.7	48	Gas-TC
298	I	SW	g_INL_SW_14.511_-11.7_-24.3	14.511	-11.7	-24.3	Gas-TC
299	I	SW	g_INL_SW_14.511_-11.7_48	14.511	-11.7	48	Gas-TC
300	I	NE	g_INL_NE_14.511_11.7_120	14.511	11.7	120	Gas-TC
301	I	NE	g_INL_NE_14.511_11.7_186.4	14.511	11.7	186.4	Gas-TC
302	I	SE	g_INL_SE_14.511_-11.7_120	14.511	-11.7	120	Gas-TC
303	I	SE	g_INL_SE_14.511_-11.7_186.4	14.511	-11.7	186.4	Gas-TC
304	I	NW	g_OUT_NW_-6.202_6.5_36	-6.202	6.5	36	Gas-TC
305	I	NW	g_OUT_NW_-6.202_6.5_48	-6.202	6.5	48	Gas-TC
306	I	NW	g_OUT_NW_-6.202_6.5_60	-6.202	6.5	60	Gas-TC
307	I	SW	g_OUT_SW_-6.202_-6.5_24	-6.202	-6.5	24	Gas-TC

#	Face	Dir.	Label	*x* (in.)	*y* (in.)	*z* (in.)	Type
308	I	SW	g_OUT_SW_-6.202_-6.5_48	-6.202	-6.5	48	Gas-TC
309	I	SW	g_OUT_SW_-6.202_-6.5_72	-6.202	-6.5	72	Gas-TC
310	I	NE	g_OUT_NE_-6.202_6.5_108	-6.202	6.5	108	Gas-TC
311	I	NE	g_OUT_NE_-6.202_6.5_120	-6.202	6.5	120	Gas-TC
312	I	NE	g_OUT_NE_-6.202_6.5_132	-6.202	6.5	132	Gas-TC
313	I	SE	g_OUT_SE_-6.202_-6.5_96	-6.202	-6.5	96	Gas-TC
314	I	SE	g_OUT_SE_-6.202_-6.5_120	-6.202	-6.5	120	Gas-TC
315	I	SE	g_OUT_SE_-6.202_-6.5_145	-6.202	-6.5	145*	Gas-TC

INL=inlet, OUT=outlet, g=gas, E=External, I=Internal
*as-built dimension

F.2.4 System and Ambient Thermocouples

Table F.4 List of thermocouples measuring ambient and system temperatures.

#	Face	Dir.	Label	*x* (in.)	*y* (in.)	*z* (in.)	Type
294	E	E	Mid_Top_Flange_E_-1_0_173.9	-1.0	0	173.9	TC (Type-K)
295	E	W	Mid_Inst_Well_W_0_0_-29.8	0.0	0	-29.8	TC (Type-K)
316	A	N	AMB_N_0_42.5_0	0	42.5	0	Gas-TC
317	A	S	AMB_S_0_-42.5_0	0	-42.5	0	Gas-TC
318	A	N	AMB_N_0_42.5_84	0.0	42.5	84	Gas-TC
319	A	S	AMB_S_0_-42.5_84	0.0	-42.5	84	Gas-TC
320	A	N	AMB_N_-12_42.5_84	-12.0	42.5	84	Gas-TC
321	A	S	AMB_S_-12_-42.5_84	-12.0	-42.5	84	Gas-TC
322	A	N	AMB_N_12_42.5_84	12.0	42.5	84	Gas-TC
323	A	S	AMB_S_12_-42.5_84	12.0	-42.5	84	Gas-TC
324	A	N	AMB_N_-97_42.5_84	-97.0	42.5	84	Gas-TC
325	A	S	AMB_S_-97_-42.5_144	-97.0	-42.5	144	Gas-TC
326	A	N	AMB_N_33_42.5_84	33.0	42.5	84	Gas-TC
327	A	S	AMB_S_33_-42.5_84	33.0	-42.5	84	Gas-TC
328	A	N	AMB_N_0_42.5_144	0	42.5	144	Gas-TC
329	A	S	AMB_S_0_-42.5_144	0.0	-42.5	144	Gas-TC
330	A	NW	AMB_NW_14.511_-11.7_-63.3	14.511	-11.7	-63.3	Gas-TC
331	A	SE	AMB_SE_14.511_11.7_225.4	14.511	11.7	225.4	Gas-TC
332	A	NE	AMB_NE_14.511_11.7_225.4	14.511	11.7	225.4	Gas-TC
333	A	SW	AMB_SW_14.511_-11.7_-63.3	14.511	-11.7	-63.3	Gas-TC
335	E	E	Power_feed_tube_E_-0.5_0_180.6	-0.5	0	180.6	TC (Type-K)
336	I	E	Power_box_air_E_1_0_193.2	1.0	0	193.2	Gas-TC

AMB=A=ambient, E=External, I=Internal

F.3 Hotwire Anemometers

The hotwire anemometers are listed in Table F.5 and shown from the east in Figure F.6 and isometrically in F.7.

Table F.5 List of hot wire anemometers including position and direction of travel.

#	Position	Travel	Duct	Label	*x* (in.)	*y* (in.)	*z* (in.)
1	inner	*x*-axis	SE	HW_SE_xvar_-7.703_-6.019	variable	-7.7	-6.0
2	middle	*x*-axis	SE	HW_SE_xvar_-11.703_-6.019	variable	-11.7	-6.0
3	outer	*x*-axis	SE	HW_SE_xvar_-15.703_-6.019	variable	-15.7	-6.0
4	horizontal	*y*-axis	SE	HW_SE_14.511_yvar_-5.019	14.511	variable	-5.0
5	inner	*x*-axis	NW	HW_NW_xvar_7.703_-6.019	variable	7.7	-6.0
6	middle	*x*-axis	NW	HW_NW_xvar_11.703_-6.019	variable	11.7	-6.0
7	horizontal	*y*-axis	NW	HW_NW_14.511_yvar_-5.019	14.511	variable	-5.0
8	middle	*x*-axis	NE	HW_NE_xvar_11.703_168.191	variable	11.7	168.2
9	outer	*x*-axis	NE	HW_NE_xvar_15.703_168.191	variable	15.7	168.2
10	horizontal	*y*-axis	NE	HW_NE_14.511_yvar_167.191	14.511	variable	167.2
11	middle	*x*-axis	SW	HW_SW_xvar_-11.703_168.191	variable	-11.7	168.2
12	outer	*x*-axis	SW	HW_SW_xvar_-15.703_168.191	variable	-15.7	168.2
13	horizontal	*y*-axis	SW	HW_SW_14.511_yvar_167.191	14.511	variable	167.2
xvar = variable in *x*-direction, yvar = variable in *y*-direction							

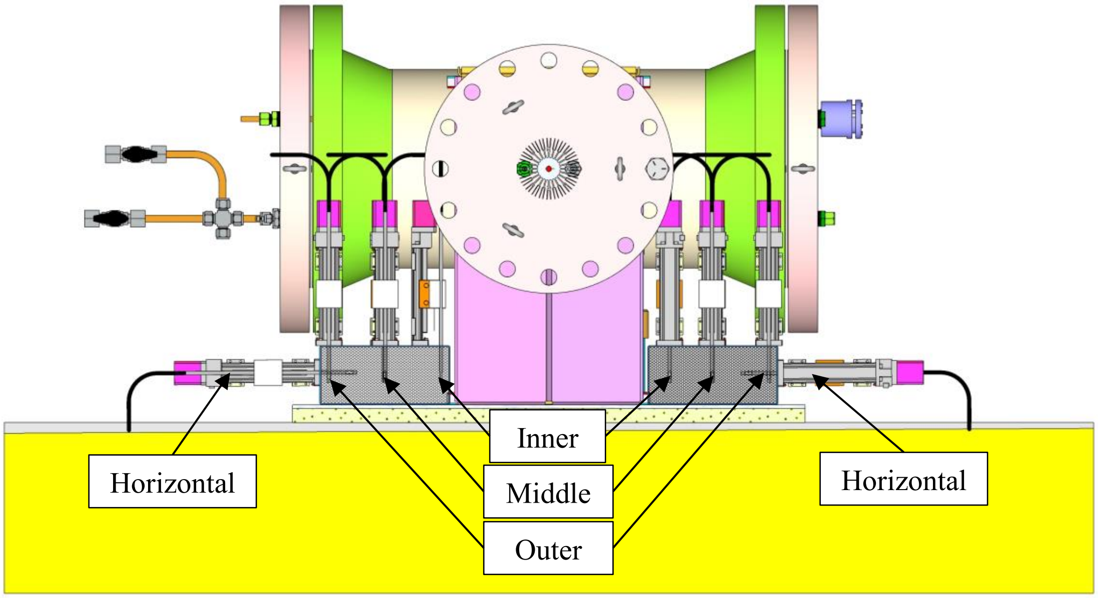

Figure F.6 View of HDCS from east.

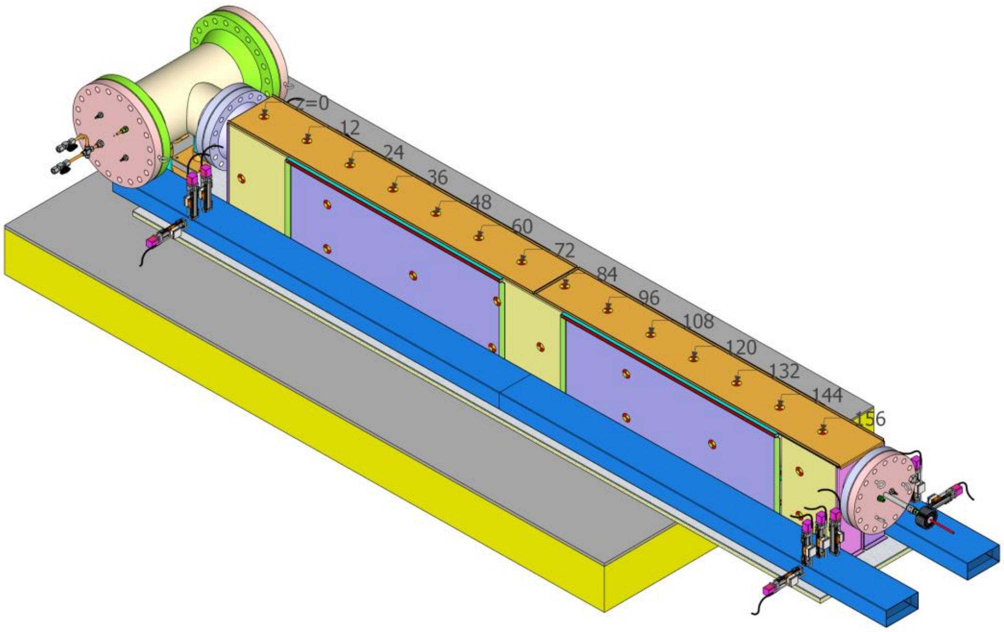

All dimensions are in inches

Figure F.7 Isometric view of HDCS (from southeast) showing vault TCs on top and south side panels and the south side hotwires.

Sandia National Laboratories